UNIVERSITÀ
DEGLI STUDI
FIRENZE

Dipartimento di Ingegneria Industriale

Corso di Dottorato in Ingegneria Industriale

Curriculum: Energetica e Tecnologie Industriali e Ambientali Innovative

Ciclo XXXII

Improvements in CFD-based Throughflow Methods for Analysis and Design of Axial Turbines

Academic Discipline (SSD) ING-IND/08

Doctoral Candidate
Martina Ricci

Supervisor
Prof. Roberto Pacciani

Coordinator
Prof. Maurizio De Lucia

2016-2019

University of Florence, Department of Industrial Engineering (DIEF).

Ai miei genitori.

Abstract

The research activity presented in this work has been devoted to the extension and improvement of a CFD-based throughflow code aimed at the development of a meridional analysis tool for modern industrial design systems for turbomachinery.

The throughflow code inherits its numerical scheme from a state-of-the-art CFD solver (TRAF code) and incorporates real gas capabilities, three-dimensional flow features, and spanwise mixing models. Secondary flow effects are introduced via a concentrated vortex model. Tip gap and shroud leakage effects are modelled in terms of source vectors in the system of governing equations. Also, film cooling and purge flow injections are taken into account as source terms vectors that are applied in selected regions of the meridional flowpath. The impact of part-span shrouds and snubbers are considered, on a local basis, through suitable body force fields.

The advection upstream splitting method (AUSM$^+$-up) upwind strategy has been adopted as a basis to construct a numerical flux scheme explicitly suited for throughflow applications. The original formulation has been adapted to handle real gas flows and to embed the treatment of body force fields in a fully consistent framework. In order to relieve the time-step limitations associated with source terms, an implicit treatment of the axisymmetric and force vectors has been considered.

During the research activity a methodology for gas turbines off-design analyses, based on the application of the throughflow method, has also been developed.

The effectiveness of the proposed methodology will be discussed by reporting the results obtained for three of the test cases used for the validation activity, for which detailed experimental data are available (the T106 high-lift, low-pressure turbine blade, the KTH 4b subsonic high-pressure steam turbine stage, and the CT3 stage high-pressure transonic gas turbine). Each one of

these allows us the assessment of the various physical models included in the framework.

Finally, the capabilities of the throughflow procedure is assessed by applying it to the study of some industrial axial turbine configurations designed and manufactured by Ansaldo Energia. The first one is a four-stage, air-cooled gas turbine. A detailed analysis at design point will be presented together with an extensive off-design study over a wide range of operating conditions with varying expansion ratios and operating speed. The last two test cases are the low-pressure modules of two large steam turbines. The assessment of the throughflow predictions will be discussed by scrutinizing them against 3D CFD analyses carried out with the TRAF code and the available experimental data.

Acknowledgments

Firstly, I would like to express my sincere gratitude to my supervisor, Professor Roberto Pacciani, for the great opportunity offered to me. His careful, well-organized guidance together with his continuous support and encouragement were essential throughout the period of research.

I would also like to thank Professor Andrea Arnone, for welcoming me into his research group, the T-Group, and all my colleagues, especially Dr. Michele Marconcini for his constructive and helpful suggestions.

Finally, I wish to express my acknowledgment to Ansaldo Energia for the permission to publish some results on their turbines. A particular thanks to Paolo Macelloni, Stefano Cecchi and Claudio Bettini from the AEN Product & Technology team, for their continuous and careful advice.

Contents

Introduction **xxiii**

1 Computational Framework **1**
1.1 Governing equations 1
1.2 Blade body forces 2
1.3 Incidence and deviation treatments 7
1.4 Dissipative force 8
1.5 Loss mechanism 11

2 Numerical method **13**
2.1 AUSM^{+}-up scheme 14
2.2 Inviscid flux and Source terms 18
2.3 Semi-implicit formulation 18
2.4 Real gas model 20
2.5 Boundary conditions 21

3 Three-dimensional Flow Features **23**
3.1 Secondary flows 23
3.2 Leakage flows 27
3.2.1 Unshrouded blades 30
3.2.2 Shrouded blades 32

4 Coolant Injections and Purge Flows **37**
4.1 Coolant flows model 38
4.2 Coolant mixing loss model 39
4.3 Coolant efficiency 40

5 Radial Mixing **41**
5.1 Viscous stresses 41
5.2 Mixing coefficient 42

6 Data matching and off-design analisys procedures **47**
6.1 Stream Surface 48
6.2 Aerodynamic Blockage 49
6.3 Loss distribution 50
6.4 Cooling scheme 51

7 Validation **53**
7.1 T106 Turbine Cascade 54
7.1.1 Discussion of results 55
7.2 KTH 4b Turbine Stage 57
7.2.1 Computational domain 59
7.2.2 Discussion of results 60
7.3 CT3 Turbine Stage 69
7.3.1 Computational domain 70
7.3.2 Discussion of results 70

8 Application **77**
8.1 Four Stage High-Pressure Gas Turbine: the 94.3A4 77
8.1.1 Base Load condition 78
8.1.2 Off-design analyisis 82
8.2 Three Stage Low-Pressure Steam Turbine: the ND48 89
8.2.1 Discussion of results 89
8.3 Four Stage Low-Pressure Steam Turbine: the ENEL 320 . . . 94
8.3.1 Discussion of results 94

9 Conclusions **99**

A Semi-implicit operator matrices **103**

B Solution of the flow surface and blockage evolution equations **105**

C A geometric approach to reverse engineering of profiles **109**

Publications **113**

Bibliography **115**

List of Figures

1.1 Extraction of tangential force. 3
1.2 Body force field representation of blade row. 4
1.3 Flow angles. 5
1.4 Adapted flow surface for the first stage of a four-stage gas turbine in subsonic and transonic conditions. 9
1.5 Entropy rise distribution along a streamline. 10
1.6 Entropy rise contours near the part-span of a turbine. 11

2.1 Convergence histories of explicit and semi-implicit scheme for a four-stage gas turbine. 20

3.1 Secondary flow model. 24
3.2 Comparisons between 3D CFD and throughflow results in terms of spanwise distributions for different values of the c_1 constant. 27
3.3 Leakage model. 28
3.4 Tip clearance loss distribution and entropy at the trailing edge of a turbine rotor blade. 30
3.5 Variation of gap discharge coefficient with clearance for Yaras and Sjolander cascade. 31
3.6 Relative flow angle at the trailing edge of a turbine rotor with and without a tip gap of 1% of the blade span. 32
3.7 Seal cavity geometry. 33
3.8 Entropy contours downstream of the trailing edge of a shrouded turbine rotor blade. 35

4.1 Flux balance in injected cell. 38

5.1 Function of inlet boundary layer thickness. 44
5.2 Radial distributions for an annular duct with wall jet. 45

6.1 S2 streamsurface for a four-stage turbine with superimposed Mach number contours. 48
6.2 Aerodynamic and geometric blockage for a turbine blade. . . 50
6.3 Prescribed (from 3D CFD analysis) and calculated (from throughflow results) entropy distributions. 51

7.1 Cascade geometry of the T106 blade [24]. 54
7.2 Predicted and measured spanwise distributions for the T106 cascade with tapered endwalls. 56
7.3 Meridional view of the KTH 4b stage with purge cavity. . . . 58
7.4 KTH test turbine stator and rotor geometries. 59
7.5 Blockage distribution of the KTH stage. 60
7.6 Spanwise distributions for the KTH stage for $\nu = 0.43$, $q = 0\%$ 64
7.7 Spanwise distributions for the KTH stage for $\nu = 0.30$, $q = 0\%$ 65
7.8 Spanwise distributions for the KTH stage for $\nu = 0.75$, $q = 0\%$ 66
7.9 Mass flow rate (a) and isentropic efficiency (b) for the KTH stage as a function of the isentropic velocity ratio ν for $q = 0\%$ 67
7.10 Spanwise distributions at rotor outlet for $\nu = 0.43$, $q = 2\%$ . . 67
7.11 Compute Absolute Mach number contours overimposed on entropy contours for the KTH stage. 68
7.12 Meridional view of the CT3 stage. 69
7.13 Blockage distribution of the CT3 stage. 70
7.14 Predicted and measured spanwise distributions of flow quantities in Plan 3 for the CT3 turbine stage at nominal conditions with and without radial mixing effects. 73
7.15 Predicted and measured spanwise distributions of flow quantities in Plan 3 for the CT3 turbine stage at low conditions with and without radial mixing effects. 74
7.16 Predicted and measured spanwise distributions of flow quantities in Plan 3 for the CT3 turbine stage at high conditions with and without radial mixing effects. 75
7.17 Measured and computed performance for the CT3 stage: (a) Total Pressure ratio; (b) Power. 76

8.1 Calculated expansion lines for the 4-stage turbine in the $h - s$ diagram. 78
8.2 Computed Absolute Mach number contours for the AE94.3A4 gas turbine: Design condition. 80
8.3 Throughflow and 3D CFD (TRAF) spanwise distributions of flow quantities at the exit of rotor blade rows for the AE94.3A4 axial turbine at nominal condition. 81
8.4 Computed performance for the axial turbine at off-design conditions: total pressure ratio (a) and power (b) in function of the pressure ratio. 84
8.5 Computed performance for the axial turbine at off-design conditions: mass-flow (a) and efficiency (b) in function of the pressure ratio. 85
8.6 Computed Absolute Mach number contours for the AE94.3A4 gas turbine: High condition. 86
8.7 Computed Absolute Mach number contours for the AE94.3A4 gas turbine: Low condition. 87
8.8 Throughflow and 3D CFD (TRAF) spanwise distributions of flow quantities at the exit of the last rotor blade row at low and high conditions. 88
8.9 Last rotor blade of the ND48 Low-Pressure Module [69]. . . . 89
8.10 Computed Absolute Mach number contours for the ND48 Low-Pressure module. 91
8.11 Expansion line for the ND48 Low-Pressure module. 92
8.12 Spanwise distributions of flow quantities for the ND48 Low-Pressure module at Stage 3 Outlet. 93
8.13 Absolute Mach Number Contours for the Enel 320MW Low-Pressure module. 95
8.14 Spanwise distributions of flow quantities at last stage exit for the Enel 320 Low-Pressure module. 97

C.1 Airfoil mathematical functions. 109
C.2 The airfoil's key points. 110

List of Tables

7.1 Geometrical parameters of blade in the T106 Test Turbine. . 54
7.2 Rotor shrouding geometrical parameters of the KTH Test Turbine. 57
7.3 Geometrical parameters of stator and rotor of the KTH Test Turbine. 57
7.4 Investigated operating points for the KTH Test Turbine. . . . 58
7.5 Key parameters of purge flow for the KTH Test Turbine. . . 59
7.6 Correlations used in the KTH Test Turbine. 60
7.7 Geometrical parameters at mid-span of stator and rotor in the CT3 Test Turbine. 69
7.8 Operating conditions at midspan for the CT3 stage. 70
7.9 Correlations used in the CT3 Test Turbine. 71

8.1 Correlations used in the 94.3A4 Gas Turbine. 78
8.2 Relative differences between computed operating characteristics for the 94.3A4 Gas Turbine at design conditions. 79
8.3 Correlations used in the ND48 Steam Turbine. 90
8.4 Relative differences between computed operating characteristics for the ND48 Low-Pressure module. 90
8.5 ENEL 320 turbine design characteristics. 94
8.6 Relative differences between computed operating characteristics for the ENEL 320 Low-Pressure module. 96

C.1 Geometrical parameters obtained for the KTH Test Turbine. 111

Nomenclature

a	speed of sound
A_w	frontal area
b	tangential blockage factor
c	absolute velocity magnitude
C_D	drag coefficient
c_d	discharge coefficient
c_p	specific heat at constant pressure
d	dissipative force magnitude
f	blade body force magnitude
F_t	loading coefficient
H	total enthalpy
h	static enthalpy or annulus height
$\mathcal{I}$	rotalpy
J	Jacobian of the coordinate transformation
k_t	thermal conductivity
l_s	length of the shroud
M	Mach number or momentum
$\dot{m}$	mass flow rate

m	meridional coordinate
N	number of blade
p	pressure
Pr_t	turbulent Prandtl number
q	momentum source coefficient
r	radius
s	specific entropy
s, n, h	intrinsic coordinates
Sc_t	turbulent Schmidt number
U, V	contravariant velocities
u, v, w	axial, radial, tangential velocity
$\mathcal{V}$	volume cell
v	specific volume
W	power
x, r, θ	cylindrical coordinates
Z	secondary flow penetration depth
z_0	vortex core radius

Greek:

α	absolute flow angle
β	relative flow angle
δ	deviation angle or boundary layer
Γ	stream surface
μ_t	dynamic viscosity
ν	kinematic fluid viscosity

Ω	angular velocity
ω	secondary vorticity
Φ	secondary loss distribution function
ρ	fluid density
τ	viscous stress
ξ, η	curvilinear coordinates

Subscripts and undersigns:

$1/2$	cells interface quantity
L, R	left and right interface
p, s	pressure and suction side
AUSM	Advection Upstream Splitting Method
EXP	Experimental Measurements
TF	Throughflow

Introduction

Throughflow methods have been on the scene of turbomachinery design and analysis since several decades. Starting from the 1940s with the general theory of Wu [72], many meridional techniques based on the radial equilibrium concept [65], the streamline curvature method [46], or the matrix throughflow method [40] were developed. During the 1970s, several researchers, such as Hirsch and Warzee [32], Denton [23], elaborated different methods for solving the governing equations of the system. For a long time, throughflow methods maintained the role of most advanced tools in industrial design systems. Since their introduction, these approaches have shown relevant limitations, like the ones related to the difficulties and uncertainty in transonic and supersonic flow conditions, or to the lack of detailed resolution of the flow field inside bladed regions. However, they represented the only practical way to obtain a three-dimensional blade design and to apply loss and deviation correlations, on a local basis, to non uniform flows in the meridional plane.

In the 90s, CFD solvers dedicated to turbomachinery started to gain popularity in industrial design processes. With the continuously increasing computational power, designers began to look at more sophisticated optimization techniques aimed to control flow details in order to further improve the performances of compressors and turbines. This trend contributed to decrease the importance of throughflow methods, which began to move from the top of the design chain to some intermediate places in design procedures. In fact, the meridional analysis is still the workhorse of modern design methodologies and remains a key tool for the designer. In preliminary stages, it provides realistic spanwise distributions of flow parameters and performances can be predicted with good accuracy when determined with suitable experimental correlations. It also offers a rapid way for evaluating the impact of the optimization of single components on the whole turbine or compressor system.

However, the development of CFD code has increased the gap in the

predictive capabilities between tools typically used at first design phases and the three-dimensional, viscous solvers employed for advanced design and optimization. Multidisciplinary problems related to the reduction of the environmental impact of propulsion and power generation systems has progressively raised new issues in turbine and compressor design. In order to address such issues, along with the increasing performances of current turbomachinery, improved techniques would be desirable at any stage of the design process. Indeed, there is a strong industrial interest in improved tools in order to effectively accomplish these goals.

Recently, with the increasing importance of renewable energy sources in the power generation scenario, designers are more interested in predicting the transient behaviour of traditional fossil fuel power generation systems. The need of a prompt and efficient response of their components to relevant and rapid load variations has then become an issue in gas turbines and compressor design. The use of CFD for calculating the operating characteristics of a multistage turbine or compressor at different rotational speeds is a very time consuming process, especially when carried out repeatedly in subsequent design iterations. Consequently, reduced fidelity tools and procedures aimed at exploring the off-design operations of multistage turbines and compressors with more affordable computational times and resources would be strongly desirable. For instance the works of Petrovic [52, 54, 53, 55, 71] represents a successful applications of throughflow methods for analyzing the performance of power generation systems components over a wide operating ranges.

In the last two decades, numerical methodologies borrowed from CFD approaches have been exploited to solve the axisymmetric Euler [67] and Navier-Stokes [73] equations in the framework of time-marching throughflow solvers. This is the case of recent studies conducted by Mildner and Gallus [43], Gehring and Riess [28], Persico and Rebay [51, 50] and Simon and Léonard [62, 61, 64]. The so-called CFD-based throughflow models are able to treat any flow regime, that is subsonic, transonic or supersonic without any major issue or particular assumption, and to provide a more realistic meridional flow field with respect to classical methodologies. Shock waves occurring in bladed or unbladed regions of the flowpath can be captured without introducing specific correlations for the related losses.

The interest in extending the range of applicability of these fast throughflow methods beyond the conceptual and first design steps has led researchers to look for appropriate methodologies to include 3D effects into meridional

analysis tools. In the context of CFD-based throughflow procedures, models for three-dimensional features of the flow can be devised on a more general way and applied on a local basis, thus providing realistic effects on radial distributions of flow parameters. This facilitates their hierarchical integration in modern design systems, and also reduces the gap with the successive design steps involving advanced CFD analyses. The works of Simon and Leonard [63, 61] and Petrovic and Wiedermann [7, 8] are examples of attempts to account for effects related to endwall boundary layers, secondary flows, entropy radial redistribution, and tip leakage flows in throughflow approaches.

The research activity presented in this work has been devoted to the extension and improvement of a CFD-based throughflow code aimed at the development of a meridional analysis tool for modern industrial design systems for turbomachinery. The entire work is focused on gas and steam turbine applications, but the proposed framework is general and flexible enough to be easily adapted to treat multistage compressors too.

Several novel models for secondary and tip leakage flow effects, coolant flow injections, and radial mixing have been implemented in an axisymmetric Euler solver with tangential blockage and body forces, which inherits its numerical scheme from a state-of-the-art CFD solver (TRAF code [6]). As outlined above, we highlighted how an efficient throughflow analysis requires computationally light numerical schemes that are able to cope with a wide range of Mach numbers and do not suffer CPU-time overhead when applied to real gas flows. To this end the AUSM$^+$-up upwind strategy was selected and implemented in the throughflow procedure. Originally devised for supersonic flows, such a numerical flux scheme has been successively extended to treat virtually any flow regime [37], from incompressible to supersonic, and it has proven to be effective for turbomachinery flow calculations [48]. The original formulation has been adapted to handle real gas flows and to embed the treatment of body force fields in a consistent framework. Note that, by using explicit schemes for time-integration of the governing equations, we should take into account the source terms contributions to the characteristic time step. In order to overcome the time-step limitations associated with source terms, an implicit treatment of the axisymmetric and force vectors has been considered in the research activity.

Secondary flows have been modelled as additional 3D flow features associated with the vortices that are created when the non-uniform inlet flow is turned by the blade rows. They are accounted for via a transverse velocity

field which, in a circumferentially-averaged sense, is assumed to be represented by discrete Lamb-Oseen-type vortices. Tip leakage effects for shrouded and unshrouded blades are modelled in terms of source and sink convective terms. For reliable predictions it is important that three-dimensional flow features and the constructive details of blades and flowpath are included in the meridional analysis. To this purpose, pre-processing tools that are able to extract all the most relevant geometric features of the blade rows from a three-dimensional coordinates set has been developed. These include the three-dimensional mean surface of the blades, the tangential blockage distributions with the possible effects of fillets, and the airfoil geometrical design parameters. The presence of part-span features, like snubbers or damping wires which are commonly encountered in steam turbine blades, is modelled in terms of an additional drag force field which is distributed locally in the area of the computational domain occupied by the cross section of the device.

In order to have realistic simulations of modern, strongly cooled, multistage gas turbines, it is very important to consider the cooling air injections into the meridional flowpath, as they can have a strong impact on blade rows aerodynamics and performances. Film cooling and purge flow injections have been accounted for as source terms vectors applied in selected regions of the meridional flowpath.

Secondary, leakage and coolant mixing losses are provided via correlations. They are considered on a local basis and distributed in the computational domain by suitable models.

In order to take into account the spanwise redistribution of flow distortions and losses, that typically occurs in multistage turbomachines, a radial mixing model has been studied and implemented.

During the research activity, we developed a methodology for gas turbines off-design analyses, based on the application of the throughflow method. We started from the calibration of the throughflow models in order to match the results of 3D CFD analyses at design point, whereupon the computational framework is frozen and used for off-design simulations. Such a matching is achieved by prescribing the S2 flow surface, the aerodynamic blockage of the blades and a suitable loss distribution. This is done by employing an automated procedure that extracts such information directly from the circumferentially averaged CFD solution at design point without the need of user inputs for the calibration. An approximate yet effective approach to

treat the changes in coolant and purge flows at off-design conditions, that avoid secondary air system studies for every considered operating point, has also been devised.

The effectiveness of the proposed methodology will be discussed by reporting the results obtained for three test cases used for the validation activity, for which detailed experimental data are available. Each test allows us to the assessment of the various physical models included in the framework. The first one is the T106 high-lift, low-pressure turbine blade, used to assess the secondary flow modelling approach. The second one is a subsonic high-pressure steam turbine stage, the KTH 4b, which allows us to highlight the average effect of three-dimensional flow features, like leakage effects and purge flows. The last one is a high-pressure transonic gas turbine, the CT3 stage, which allows us to analyse the radial mixing model and the predictive capability of the solver at off-design conditions.

Finally, the capabilities of the throughflow procedure is assessed by applying it to the study of some industrial axial turbine configurations designed and manufactured by Ansaldo Energia. The first one is a four-stage, medium size F-class, air-cooled gas turbine. A detailed analysis at design point will be presented together with an extensive off-design study over a wide range of operating conditions with varying expansion ratios and operating speed. The last two test cases are the low-pressure modules of two large steam turbines. The first one refers to a state-of-the-art turbine (ND48) for the $100-250$ MW output power range, that features a modern design based on extensive blade aerodynamics optimization (Torre et al. [69]). The second one, (ENEL 320 MW) features a more traditional design that was experimentally validated with field measurements (Accornero et al. [2, 1]). The assessment of the throughflow predictions will be compared with 3D CFD analyses carried out with the TRAF code and the available experimental data.

It will be shown how the generality and reliability of the proposed throughflow method demonstrates its feasibility for an intensive use in the design of gas and steam turbines. In particular, throughflow predictions can compete with the ones provided by state-of-the-art 3D CFD approaches and can be obtained with a small fraction of the computational time.

Outline

The present work is organized in eight chapters: the first four chapters are dedicated to the development of the code, while the two last chapters address the validation and applications of the model.

In the first chapter, the set of governing equations describing the throughflow model are presented. Various aspects related to the modelling are addressed such as the tangential blockage, blade body and dissipative force.
The second chapter is dedicated to the numerical methods used to solve the equations obtained and described in the first chapter.
The third chapter presents the three-dimensional flow features models implemented in the throughflow solver.
The fourth chapter is dedicated to the coolant injection and purge flows.
The fifth chapter is dedicate to the radial mixing model.
The sixth chapter is dedicated to the description of the automated procedures for off-design analysis of multistage turbines.

The following chapter presents the validation of the methodology on three experimental test cases, and the last one presents the results of the application of the throughflow model to three industrial turbomachinery configurations designed and manufactured by Ansaldo Energia.

Chapter 1

Computational Framework

A novel Computational Fluid Dynamics (CFD)-based throughflow model is introduced in this chapter. Blade and dissipative body force models, that were already implemented in the throughflow method since its very first stages of development, will be presented and discussed. It will also be discussed how the dissipative body force formulation has been extended during this research activity in order to include losses originating from part-span features of the blades like damping wires or snubbers.

1.1 Governing equations

An appropriate model for the meridional analysis of turbomachinery can be obtained by circumferentially averaging the 3D unsteady Euler equations in cylindrical coordinates. The averaging process removes the circumferential coordinates but introduces sources terms which account for the angular momentum variation due to effect of blades and for the work exchange in rotor rows. These terms are called, respectively, the tangential blockage and the body forces. In addition to these, we introduce a dissipative body force field which is used to model viscous losses.

The continuity, momentum and energy equations written in conservative form and mapped in a curvilinear, body fitted coordinate system ξ e η, are:

$$\frac{\partial bJ^{-1}W}{\partial t} + \frac{\partial bJ^{-1}F}{\partial \xi} + \frac{\partial bJ^{-1}G}{\partial \eta} = bJ^{-1}S + J^{-1}S_b + J^{-1}S_f. \qquad (1.1)$$

The vector of the so-called conservative variables W consists, in three dimensions, of the following five components:

$$W = \begin{bmatrix} \rho \\ \rho u \\ \rho v \\ \rho w \\ \rho E \end{bmatrix}.$$

For the vector of convective fluxes we obtain:

$$F = \begin{bmatrix} \rho U \\ \rho U u + p\xi_x \\ \rho U v + p\xi_y \\ \rho U w \\ \rho u H \end{bmatrix}, \qquad G = \begin{bmatrix} \rho V \\ \rho V u + p\eta_x \\ \rho V v + p\eta_y \\ \rho V w \\ \rho v H \end{bmatrix},$$

with the contravariant velocity U and V. Finally, the source terms at the right hand side:

$$S = \begin{bmatrix} -\rho v \\ -\rho u v \\ \rho w^2 - \rho v^2 \\ -2\rho v w \\ -\rho v H \end{bmatrix}, \qquad S_b = \begin{bmatrix} 0 \\ p\frac{\partial b}{\partial x} \\ p\frac{\partial b}{\partial r} \\ 0 \\ 0 \end{bmatrix}, \qquad S_f = \begin{bmatrix} 0 \\ \rho f_x - \rho d_x \\ \rho f_r - \rho d_r \\ \rho f_\theta - \rho d_\theta \\ \rho(f_\theta - d_\theta)\Omega r \end{bmatrix},$$

where S is a source term vector arising from the formulation of the Euler equations in cylindrical coordinates, S_b is the source term vector which accounts for the variation of tangential blockage in the blade passage, S_f is the source term vector containing the components of the blade body force, $\mathbf{f}$, and the dissipative forces, $\mathbf{d}$. These terms, which represent the details of three-dimensional viscous flow, are computed by suitable closure models.

The throughflow code inherits its numerical scheme from a 3D CFD code. A detailed description will be discussed in the Chapter 2.

1.2 Blade body forces

A body force representation of a blade row determines the axisymmetric influence of the blades on the flow field through source terms in the governing

equations. The pressure forces on blades are averaged in the tangential direction to produce the blade body force field. Similarly, for viscous stresses to reproduce the dissipative force field.

The unknown terms arising from the tangential averaging process and that are usually interpreted as blade body force components can be written as:

$$f_x = \frac{N}{2\pi\rho b}\left[\left(p\frac{\partial\theta}{\partial x}\right)_p - \left(p\frac{\partial\theta}{\partial x}\right)_s\right],$$
$$f_r = \frac{N}{2\pi\rho b}\left[\left(p\frac{\partial\theta}{\partial r}\right)_p - \left(p\frac{\partial\theta}{\partial r}\right)_s\right],$$
$$f_\theta = \frac{N}{2\pi\rho b}\left[\left(\frac{p}{r}\right)_p - \left(\frac{p}{r}\right)_s\right],$$

where the subscripts p and s identify the blade pressure and suction sides respectively.

It can be noticed how the tangential component of the blade body force can be directly related to the pressure difference between the pressure and suction surface of the blade:

$$f_\theta = \frac{N}{2\pi b\rho r}\Delta p. \tag{1.2}$$

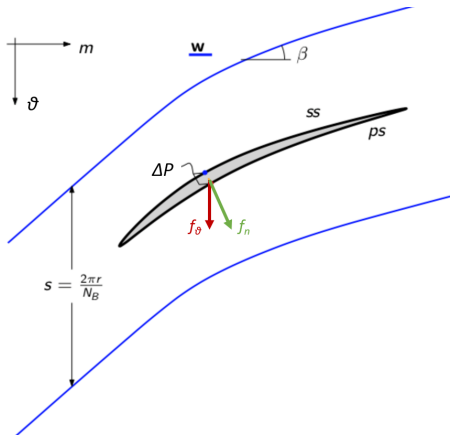

Figure 1.1: Extraction of tangential force.

The blade body force field is assumed to be orthogonal to the flow surface and null in non-bladed regions, as shown in Figure 1.2. Its intensity can be determined by assuming that the deflection of the meridional S2 stream surface, which represents the average path of the flow, is equal to the one of the mean surface of the blade.

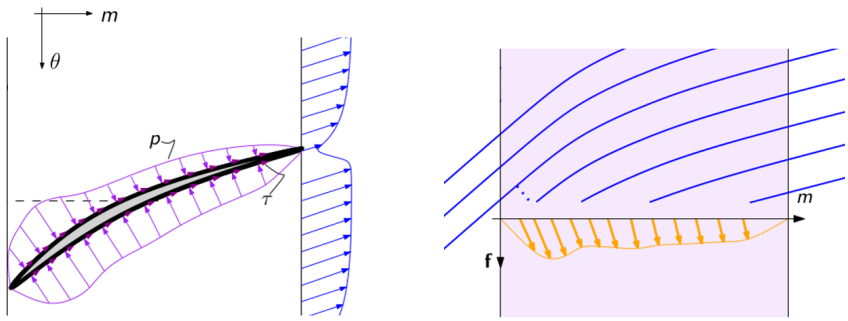

(a) *Blade row.* **(b)** *Body force field.*

Figure 1.2: Body force field representation of blade row.

In analysis problems, the blade mean surface can be described in the functional form as:

$$\theta = \Gamma(x, r),$$

or, in the implicit form as:

$$\varphi(x, r, \theta) = \theta - \Gamma(x, r).$$

This will result a flow surface if the dot product between the relative velocity $\mathbf{v}$ and its normal unit vector $\mathbf{n}$ is equal to zero:

$$\mathbf{v} \cdot \mathbf{n} = u \cdot n_x + v \cdot n_r + w \cdot n_\theta = 0, \tag{1.3}$$

where, according to the Figure 1.3, we have:

$$\begin{aligned} n_x &= -\sin\alpha\cos\beta, \\ n_r &= -\sin\alpha\sin\beta, \\ n_\theta &= \cos\alpha. \end{aligned}$$

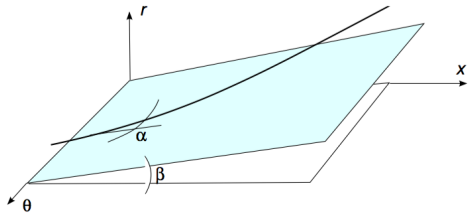

Figure 1.3: Flow angles.

Recalling that the surface normal is equal to the normalized gradient:

$$\mathbf{n} = \frac{\nabla\varphi}{|\nabla\varphi|} = \frac{\left[-\frac{\partial\Gamma}{\partial x}, -\frac{\partial\Gamma}{\partial r}, \frac{1}{\partial r}\right]^T}{|\nabla\varphi|},$$

then, replacing in (1.3), we have:

$$u\frac{\partial\varphi}{\partial x} + v\frac{\partial\varphi}{\partial r} + (w - \Omega r)\frac{1}{r}\frac{\partial\varphi}{\partial\theta} = -u\frac{\partial\Gamma}{\partial x} - v\frac{\partial\Gamma}{\partial r} + \frac{w}{r} - \Omega = 0,$$

which is known as the flow tangency condition. The blade body force components can then be expressed as:

$$\begin{aligned} f_x &= -f\frac{\partial\Gamma}{\partial x}, \\ f_r &= -f\frac{\partial\Gamma}{\partial r}, \\ f_\theta &= \frac{f}{r}. \end{aligned} \tag{1.4}$$

Several closure models have been proposed to determine the blade body force intensity, $\mathbf{f}$. For design applications, Sturmayr and Hirsch [67] determined the blade body force by imposing the distribution of angular momentum inside the blade rows. The application of such a constraint was relaxed in time i.e. the blade body force magnitude was determined as the solution of a time dependent equation:

$$\frac{\partial f}{\partial t} = K\left[\left(\frac{w}{r}\right)^{target} - \frac{w}{r}\right].$$

For analysis purposes, Simon and Leonard [61] used an approach, firstly proposed by Baralon et al. [9], in which a time-dependent equation for the blade body force intensity is constructed in order to satisfy the requirement of flow tangency to a prescribed S2 (e.g. Wu [72]) streamsurface:

$$\frac{\partial f}{\partial t} = K\left(-u\frac{\partial \Gamma}{\partial x} - v\frac{\partial \Gamma}{\partial r} + \frac{w}{r} - \Omega\right), \tag{1.5}$$

in which the time evolution of the blade body force is used to drive the right hand side to zero and thus to satisfy the flow tangency constraint. Although an evolutionary formulation for the blade body force may be desirable, Equation (1.5) is not of practical use for design problems. Moreover, the value of the constant K, which acts as a relaxation factor, must be carefully chosen case by case in order to end up with good convergence rates.

Persico and Rebay [51] prescribed the flow tangency condition in bladed regions by modeling the blade as an elastic constraint and calculated the body force field by using a penalty formulation ([44, 5]). The method requires no additional equations, but needs the tuning of some constants and relaxation factors in order to ensure a satisfactory degree of flow tangency to the S2 streamsurface at convergence, without inducing instabilities in the time-marching process.

In this work, an algebraic body force model, which can be regarded as a generalization of the ones used in streamline curvature methods, has been employed [49]. The relative tangential velocity required to obtain the correct flow deflection can be expressed by the tangency condition (1.3) as:

$$\tilde{w} = \Omega r + ur\frac{\partial \Gamma}{\partial x} - vr\frac{\partial \Gamma}{\partial r}. \tag{1.6}$$

where u and v are axial and radial velocity components. In this way, substituting in the steady formulation of the governing equations,

$$\frac{\partial bF}{\partial x} + \frac{\partial bG}{\partial r} = bS,$$

and considering the tangential component of the momentum equation:

$$\frac{\partial b\rho u\tilde{w}}{\partial x} + \frac{\partial b\rho v\tilde{w}}{\partial r} = b\rho f_\theta,$$

it is possible to obtain:

$$u\frac{\partial \tilde{w}}{\partial x} + v\frac{\partial \tilde{w}}{\partial r} = f_\theta.$$

Finally, recalling equation (1.4), the blade body magnitude is calculated as:

$$f_\theta r = f = u\frac{\partial r\tilde{w}}{\partial x} + v\frac{\partial r\tilde{w}}{\partial r}. \tag{1.7}$$

Note that this equation can be directly used also for design purposes, where an angular momentum distribution $r \cdot \tilde{w}$ is typically prescribed between blade row inlet and outlet.

1.3 Incidence and deviation treatments

In the actual operation of turbomachinery, the flow direction does not follow the camber line angle at the airfoil leading and trailing edge due to incidence and deviation effects. As a consequence, the actual stream surface does not coincide with the mean blade surface, and their differences due to incidence and deviation must be accommodated with suitable treatment. In the present work, an adaptive formulation for the mean stream surface is used [49]. A time-dependent equation for Γ is defined as follows:

$$\frac{\partial \Gamma}{\partial t} = \frac{\omega}{\tau}\left[\mu_1(\alpha_1 - \beta_1) + \mu_2(\alpha_2 - \beta_2 - \delta)\right], \tag{1.8}$$

where α_1 and α_2 are the flow angles, respectively, at the blade leading and trailing edge, β_1 and β_2 are the camber line angles at the same locations, and δ is the deviation angle, defined as:

$$|\delta| = |\alpha_2 - \beta_2|.$$

Moreover, ω is a relaxation factor equal to 0.25, and τ is a time scale assumed as the ratio between the meridional velocity, c_m, and the local blade length along the meridional direction:

$$\tau = \frac{c_m}{m_{TE} - m_{LE}}.$$

Finally, the terms μ_1 and μ_2 are used to distribute, step-by-step, the stream surface, m, along the blade meridional length (the axial chord in the case of

an axial turbomachine), m^*. To this end:

$$\mu_1(m) = \begin{cases} 1, & \text{if } m \leq m_{LE} \\ \frac{1}{2}\left[1 - \cos\left(\frac{m - m_{LE}}{m_1^* - m_{LE}}\right)\right], & \text{if } m_{LE} < m \leq m_1^* \\ 0, & \text{if } m > m_1^* \end{cases} \tag{1.9}$$

$$\mu_2(m) = \begin{cases} 0, & \text{if } m \leq m_2^* \\ \frac{1}{2}\left[1 - \cos\left(\frac{m - m_2^*}{m_{TE} - m^*}\right)\right], & \text{if } m_2^* < m \leq m_{TE} \\ 1, & \text{if } m > m_{TE} \end{cases} \tag{1.10}$$

The value of m_1^* has been chosen so that the effect of incidence is distributed between the blade leading edge and the first 30% of blade length, while for the deviation it is assumed that its effect is distributed between the minimum blockage factor location, which coincides with m_2^*, and the blade trailing edge.

Once the steady state is reached, the blade mean surface and the stream surface, which follows the computed flow direction upstream of the blade leading edge, will smoothly merge at the location m_1^*. In the same way, at the location m_2^*, the stream surface will depart again from the blade mean surface so that the flow will eventually leave the blade row with an angle that differs of an amount equal to the deviation δ from the geometrical one.

Equation (1.8) is integrated at each time step and the adapted surface Γ is used in equations (1.4), (1.6), (1.7) to compute the source term vector S_f.

An example of the adaptive methodology defined by equations (1.8), (1.9) and (1.10) is reported in Figure 1.4, which shows the computed flow surface for the first-stage of an industrial gas turbine. It is possible to observe the changes in the flow surface corresponding to different operating conditions: subsonic and transonic.

1.4 Dissipative force

The Distributed Loss Model [22] is based on the assumption that the entropy rise along the flow streamlines due to viscous dissipation can be represented by the work of a drag force, $\mathbf{d}$, which is assumed to be tangent to the streamline and opposite to the relative velocity vector.

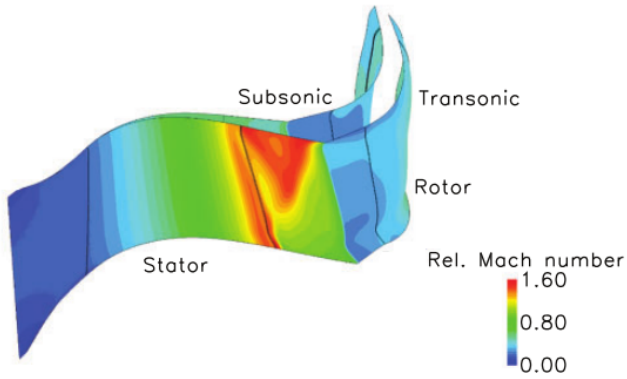

Figure 1.4: Adapted flow surface for the first stage of a four-stage gas turbine in subsonic and transonic conditions.

The dissipating body force field, $\mathbf{d} = d\mathbf{t}$, must satisfy the Crocco's theorem, which, in the steady case and in the relative frame of reference, can be written as:

$$\mathbf{w} \times (\nabla \times \mathbf{w} + 2\omega) = \nabla \mathcal{I} - T\nabla s - \frac{f}{\rho}\mathbf{n} + d\mathbf{t},$$

where $\mathcal{I}$ is the rotalpy and s the entropy of the flow. By taking the scalar product of such equation with the relative velocity vector, $\mathbf{w}$, we obtains:

$$T\nabla s \cdot \mathbf{w} = d\mathbf{t} \cdot \mathbf{w}. \tag{1.11}$$

The tangent to streamline unit vector can be expresses as:

$$\mathbf{t} = \frac{\mathbf{w}}{|\mathbf{w}|},$$

and so, replacing in equation (1.11), we obtain:

$$T\nabla s \cdot \mathbf{w} = d|\mathbf{w}|.$$

The entropy rise across a blade row is computed via loss correlations. The dissipating body force magnitude can be computed as:

$$\mathbf{d} = T\nabla s \cdot \frac{\mathbf{w}}{|\mathbf{w}|}. \tag{1.12}$$

In order to determine a realistic distribution along the streamline, it is used a law that closely follows the ones predicted with viscous, three-dimensional, CFD calculations.

For example, as shown in Figure 1.5, the profile loss is distributed for the 30% between the leading edge and minimum blockage factor location, and for 70% between this location and the trailing edge. Instead, the trailing edge loss is applied for a length equal to the diameter of the trailing edge immediately downstream the blade row exit plane.

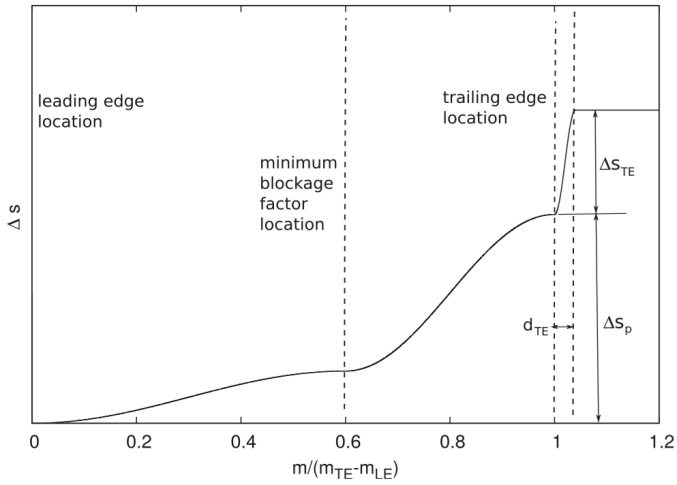

Figure 1.5: Entropy rise distribution along a streamline.

An additional drag force, $\mathbf{d_w}$, is added to equation (1.12) to simulate the presence of part-span damping wires or snubbers. The vector $\mathbf{d_w}$ is applied to mesh cells that approximates the actual wire cross-section, where the local contribution for each cell is obtained by area-averaging the total drag force:

$$\mathbf{d_w} = -\frac{1}{2}\rho C_D c_{rel}^2 A_w \mathbf{t},$$

where A_w is the frontal area and C_D the drag coefficient of the wire. As an example, the entropy rise contours near the part-span snubber of a last rotor blade steam turbine are reported in Figure 1.6.

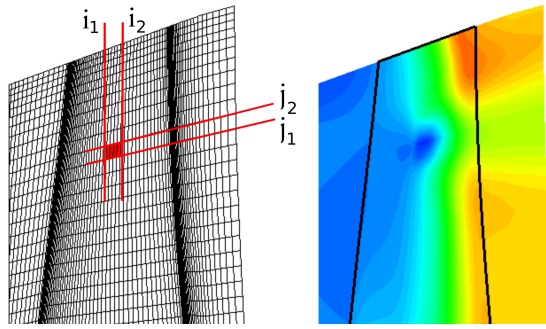

Figure 1.6: Entropy rise contours near the part-span of a turbine.

1.5 Loss mechanism

The addition of the dissipative force per unit volume, $\mathbf{d}$, to the system of governing equation (1.1) is carried out via the source term vector:

$$S_{f,d} = -\begin{bmatrix} 0 \\ \rho d_x \\ \rho d_r \\ \rho d_\theta \\ \rho d_\theta \Omega r \end{bmatrix}.$$

In the present work, losses are computed by empirical correlations and then distributed in the computational domain. In literature, there are many different definitions of loss coefficients. Perhaps the most common is the pressure loss coefficient, which is defined by:

$$Y = \frac{p_{01} - p_{02}}{p_{02} - p_2} = \frac{p_{01} - p_{02}}{\frac{1}{2}\rho V_2^2}.$$

A more useful loss coefficient for design purpose is the energy loss coefficient, ζ, or the entropy loss coefficient, ζ_s, that for a turbine blade are characterize by:

$$\zeta = \frac{h_2 - h_{2s}}{h_{02} - h_2},$$

$$\zeta_s = \frac{T_2 \Delta S}{(h_{02} - h_2)}.$$

The great advantage of ζ_s is that may be used directly as a measure of entropy production both in stator and rotor blades rows, and so for the whole machine [21]. The relation between the pressure loss coefficient and the energy loss coefficient is given by:

$$\zeta = \frac{1 - \left(1 + Y\left(1 - \left(1 + 0.5\left(\gamma - 1\right)M^2\right)^{-\frac{\gamma}{\gamma-1}}\right)\right)^{-\frac{\gamma-1}{\gamma}}}{0.5\left(\gamma - 1\right)M^2},$$

while between the energy loss coefficient and the entropy loss coefficient by:

$$\zeta_s = \frac{\zeta}{1 - 0.25\left(\gamma - 1\right)M^2\zeta}.$$

Over the years, many researchers have carried out experimental tests in order to determine appropriate correlations, for design and off-design conditions, capable of estimating losses present within the turbomachinery. A number of approaches have been made to predict the total pressure loss coefficients and flow deviation angles. A detailed account of the different methods have been given by Dunham and Came [25], Kacker and Okapuu [34], Craig and Cox [17], Traupel [70] and others.

In the present work, various experimental correlations have been considered. They range from the the well-known Kacker and Okapuu [34], based on Ainley and Mathieson's model, to the ones of Traupel [70] or Craig and Cox [17], up to the recent ones of CIAM (Central Institute of Aviation Motors) [10]. The last two correlations has been implemented during the present research activity.

Once the spanwise distribution of loss coefficient have been computed for each blade row, it is first converted in terms of entropy loss coefficient and finally in entropy rise contributions that are used as a closure for the Distributed Loss Model to calculate the dissipative force.

Chapter 2

Numerical method

The throughflow code inherits its numerical scheme from the steady release of the TRAF code [16]. The system of governing equations (1.1) is solved for density, absolute momentum components, and total energy via a time-marching methodology.

The space discretization is based on a cell centered finite volume scheme. The system of governing equations is advanced in time using an explicit four-stage Runge-Kutta scheme. Residual smoothing, local time-stepping, and multigridding are employed to speed-up convergence to the steady state solution. The multigrid technique is based on the Full Approximation Storage (FAS) scheme of Brandt [15] and Jameson [33]. A V-type cycle with coarse grid sweeps (subiterations) is used. For the sake of computational efficiency, the time integration of the evolution equation for the flow surface (Eq. (1.8)) is carried out only on the finest grid level and the changes $\delta\Gamma$ are transferred to the coarse grid levels by interpolation.

Several numerical flux schemes are available for the discretization of convective terms. They range from central schemes with artificial dissipation to second order TVD schemes built on top of several upwind strategies.

The artificial dissipation model available in the code is the one introduced by Jameson et al. [33], with the eigenvalue scaling of Martinelli and Jameson [41] and Swanson and Turkel [68]. This have proven to be a fairly general scheme that shows no major issues when applied to ideal or real gas flows from subsonic to transonic flow regimes. However, on the supersonic flow side, it can suffer reduced robustness when the Mach number is sensibly above the unity. On the low Mach number side, a preconditioning strategy should be

used for effectively scaling the dissipation terms as the incompressible limit is approached.

The requirements for efficient throughflow analyses call for computationally light numerical schemes that are able to cope with a wide range of Mach numbers and do not suffer too much CPU-time overhead when adapted to deal with real gases. During the present research activity, the AUSM$^+$-up upwind strategy was selected and implemented in the throughflow procedure. Originally devised for supersonic flows, such a numerical flux scheme has been successively extended to treat virtually any flow regime [37], from incompressible to supersonic, and it has proven to be effective for turbomachinery flow calculations [48]. In the present work the AUSM$^+$-up framework has been adapted to handle real gas flows and extended to treat the body force terms that characterize throughflow frameworks.

When explicit time-integration schemes are used in the governing equations (1.1), the source terms contributions to the characteristic time step should, in principle, be accounted for. The most relevant contributions come from axisymmetric source terms and blade body forces. For example, in highly swirling flows, the impact of the axisymmetric terms on the stability properties of the numerical method can be very important. The tip regions of low-pressure, steam-turbine bladings, which are characterized by very high blade tip speeds and tangential velocities, are typically affected by such stability issues. In order to relieve the time-step limitations associated with source terms, an implicit treatment of the axisymmetric and force vectors has been considered in the research activity. This leads to a semi-implicit time-integration scheme that allows one to determine the characteristic time step only on the base of flux jacobian eigenvalues, (as if there was no source term in the governing equations) while operating with the CFL numbers typical of Runge-Kutta schemes.

2.1 AUSM$^+$-up scheme

The AUSM$^+$-up scheme is an all-Mach-numbers variant in the AUSM family of upwind schemes. It relies on the concept of the so-called numerical speed of sound [39] to treat flow regimes that range from incompressible to supersonic. It has proven to be flexible enough to handle ideal or real gas flows and even multi-phase flows. Let us consider the system of governing equation (1.1). As a first step, the inviscid flux is explicitly split into advective

and pressure fluxes [37]. For example, in the curvilinear ξ direction, at the interface denoted by subscript "1/2", has the form:

$$\mathbf{F}_{1/2} = \dot{m}_{1/2}\mathbf{\Phi}_{1/2} + \mathbf{P}_{1/2}, \tag{2.1}$$

where the vector $\mathbf{\Phi}_{1/2}$, determined by a standard upwind formulation, and the pressure flux are expressed as:

$$\mathbf{\Phi} = \begin{bmatrix} \rho a_{1/2} \\ \rho a_{1/2} u \\ \rho a_{1/2} v \\ \rho a_{1/2} w \\ \rho a_{1/2} H \end{bmatrix}, \qquad \mathbf{P}_{1/2} = b \begin{bmatrix} 0 \\ p_{1/2}\xi_x \\ p_{1/2}\xi_r \\ 0 \\ 0 \end{bmatrix}.$$

Clearly, the main tasks are to define the mass and pressure fluxes, which will now described in detail.

The mass flux has the form:

$$\dot{m}_{1/2} = u_{1/2}\rho_{L/R} = a_{1/2}M_{1/2}\rho_{L/R}, \tag{2.2}$$

where $u_{1/2}$ is the convective velocity, $a_{1/2}$ is the speed of sound and $\rho_{L/R}$ is the density, labelled by subscripts "L" and "R", respectively, namely to the left and right of the interface. Since the convective flux is associated with the linear field of the system of conservation laws, the interface density can be dictated by the direction of Mach number. Thus, rewriting the equation (2.2) gives:

$$\dot{m}_{1/2} = a_{1/2}M_{1/2}b \cdot \begin{cases} \rho_L & M_{1/2} > 0, \\ \rho_R & \text{otherwise.} \end{cases}$$

The interface Mach number is set in terms of M_L and M_R as:

$$M_{1/2} = \mathcal{M}^+_{(m)}(M_L) + \mathcal{M}^-_{(m)}(M_R) + \mathcal{M}_P.$$

The split Mach number, $\mathcal{M}^{\pm}_{(m)}$, are polynomial functions of degree $m\,(= 1, 2, 4)$, as given in [37]:

$$\mathcal{M}^{\pm}_{(1)}(M) = \frac{1}{2}\left(M \pm |M|\right),$$
$$\mathcal{M}^{\pm}_{(2)}(M) = \pm\frac{1}{4}\left(M \pm 1\right)^2,$$

$$\mathcal{M}^{\pm}_{(4)}(M) = \begin{cases} \mathcal{M}^{\pm}_{(1)}(M) & \text{if } |M| \geq 1, \\ \mathcal{M}^{\pm}_{(2)}\left(1 \mp 16\beta\mathcal{M}^{\mp}_{(2)}\right) & \text{otherwise.} \end{cases}$$

The pressure diffusion term, $\mathcal{M}_P$, introduced to enhance calculations of low Mach number or multi-phase flow, is defined to be:

$$\mathcal{M}_P = -\frac{K_P}{f_a}\max\left(1 - \sigma\bar{M}^2, 0\right)\frac{p_R - p_L}{\frac{1}{2}\rho_{1/2}a^2_{1/2}}, \tag{2.3}$$

where $0 \leqslant K_p \leqslant 1$, $\sigma \leqslant 1$, while the interface density is evaluated as a simple arithmetic average:

$$\rho_{1/2} = \frac{\rho_L + \rho_R}{2}.$$

As the flux splitting is carried out in terms of Mach number only,

$$M_{L,R} = \frac{U_{L,R}}{a_{1/2}},$$

the interface speed of sound, $a_{1/2}$, is the only quantity that needs to be reformulated for the application to real gases. In the present work the following formulation is employed:

$$a = \sqrt{\left[\frac{\partial p(h,v)}{\partial \rho}\right]_s},$$

where the speed of sound is simply expressed as a derivative of pressure as a function of static enthalpy,

$$h = H - \frac{c^2}{2},$$

and specific volume, v, at constant entropy.

For the purpose of properly scale the numerical dissipation with the flow speed, a simple quadratic expression has been adopted for the speed of sound scaling factor [37]:

$$f_a(M_0) = M_0(2 - M_0),$$

with the reference Mach number defined as:

$$M_0^2 = \min\left[1, \max\left(\bar{M}^2, M_{co}^2\right)\right], \tag{2.4}$$

where the mean local Mach number is expressed with respect to the numerical speed of sound:

$$\bar{M} = \frac{U_L + U_R}{a_{1/2}}.$$

The cut-off Mach number, M_{co}, is introduced in (2.4) to prevent M_0 becoming too small causing convergence stall and numerical issues. In the throughflow analyses presented in this work, the cut-off Mach number was calculated with the following formula:

$$M_{co} = \mu \cdot \min\left[1, \max\left(M_{in}, M_{out}\right)\right],$$

where M_{in} and M_{out} are average Mach numbers at inlet and outlet boundaries of the computational domain, and $\mu = 0.2 - 0.4$.

As for the interface Mach number (equation (2.3)), the pressure flux is modified [38] adding a velocity diffusion term $\mathcal{P}_u$:

$$p_{1/2} = \mathcal{P}_{(n)}^{+}(M_L)p_L + \mathcal{P}_{(n)}^{-}(M_R)p_R + \mathcal{P}_u,$$

where $n = 1, 3$ or 5 corresponds to the degree of the polynomials $\mathcal{P}^{\pm}$, as in $\mathcal{M}^{\pm}$. The fifth degree polynomials are preferred because they are found to yield more accurate solutions. They can be expressed in terms of split Mach number functions as:

$$\mathcal{P}_{(5)}^{\pm}(M) = \begin{cases} \frac{1}{M}\mathcal{M}_{(1)}^{\pm} & \text{if } |M| \geq 1, \\ \mathcal{M}_{(2)}^{\pm}\left[(\pm 2 - M) \mp 16\alpha M \mathcal{M}_{(2)}^{\mp}\right] & \text{otherwise.} \end{cases}$$

Also, the velocity diffusion term is given by:

$$\mathcal{P}_u = -K_u \mathcal{P}_{(5)}^{+}(M_L)\mathcal{P}_{(5)}^{-}(M_R)\left(\rho_L + \rho_R\right) a_{1/2}\left(u_R - u_L\right),$$

and the constant $0 \leq K_u \leq 1$. The coefficient $\mathcal{P}_{(5)}^{+}(M_L)\mathcal{P}_{(5)}^{-}(M_R)$ simply switches off $\mathcal{P}_u$ as the flow becomes supersonic, resulting in one-sided upwinding.

2.2 Inviscid flux and Source terms

In order to bring uniformity and consistency in the numerical treatment of all the terms of the governing equations, the described upwind scheme has also been used to evaluate the right hand side of equation (1.7), where the tangential component of the momentum equation in steady form is computed by:

$$f_\theta = \frac{f}{r} = \frac{\partial \tilde{F}_\theta}{\partial \xi} + \frac{\partial \tilde{G}_\theta}{\partial \eta} + J^{-1}\tilde{S}_\theta,$$

with the area-averaged inviscid flux and the source term defined as:

$$\tilde{F}_\theta = \rho b U \tilde{w}, \qquad \tilde{G}_\theta = \rho b V \tilde{w}, \qquad \tilde{S}_\theta = \frac{2\rho b v \tilde{w}}{r}.$$

Now, with the AUSM$^+$-up upwind scheme, also the tangential momentum fluxes must be assembled in the standard finite-volume form. It is possible to write the interface flux in terms of a common mass flux, for example:

$$\tilde{F}_{\vartheta,1/2} = \dot{m}_{1/2}\tilde{\Phi}_{\vartheta,1/2},$$

where the quantity $\tilde{\Phi}_\vartheta$ convected by $\dot{m}$ is:

$$\tilde{\Phi}_{\vartheta,1/2} = a_{1/2}\tilde{w}.$$

A second order scheme is built on top of the present upwind strategy by means of MUSCL extrapolation and TVD limiters. In particular, the Van-Albada limiter has been used in the present work.

2.3 Semi-implicit formulation

Let us consider the system of governing equations (1.1). The state vector of the conservative variables can be expressed by an implicit treatment at the time $(n+1)$ of the source term vectors, in particularly the axysimmetric terms, S, and the blade forces, S_f, as:

$$bJ^{-1}\frac{\partial W}{\partial t} = -C(W) + bJ^{-1}S^{(n+1)} + J^{-1}S_b^{(n)} + J^{-1}S_f^{(n+1)}, \qquad (2.5)$$

where $C(W)$ represents the convective fluxes:

$$C(W) = \frac{\partial bJ^{-1}F}{\partial \xi} + \frac{\partial bJ^{-1}G}{\partial \eta}.$$

As we noticed, the solution of the equations (2.5) requires the evaluation of the source terms at the new time level, that cannot be done directly. However, we can express the new interface position as a function of the old position. For example, the axysimmetric source term results:

$$S^{(n+1)} = S^{(n)} + \frac{\partial S}{\partial W}\Big|_n \delta W.$$

Hence, we obtain:

$$bJ^{-1}\frac{\partial W}{\partial t} = C(W) + bJ^{-1}S^{(n)} + J^{-1}S_f^{(n)} + \frac{\partial (bS)}{\partial W}\Big|_n \delta W + \frac{\partial S_f}{\partial W}\Big|_n \delta W,$$

and so, calling:

$$R = C(W) + bJ^{-1}S^{(n)} + J^{-1}S_f^{(n)},$$

and:

$$A = \frac{\partial (bS)}{\partial W}\Big|_n, \qquad B = \frac{\partial S_f}{\partial W}\Big|_n,$$

the final expression is:

$$bJ^{-1}\frac{\partial W}{\partial t} = R + (A + B)\ \delta W.$$

Applying the residual smoothing technique we have:

$$\left[\frac{\mathcal{V}}{\delta t} + \varepsilon\,(A + B)\right]\delta W = R,$$

where $\mathcal{V}$ is the volume of the cell, ε is a parameter to be determined and R is the residual function. Therefore, for each Runge-Kutta step:

$$\left[I + \varepsilon\frac{\delta t}{\mathcal{V}}P\right]\delta W = R. \tag{2.6}$$

where the matrix P is the flux Jacobian expressed in primitive variables and I is the identity matrix. The term on the left-hand side is referred to as the

implicit operator. The details of this matrix is written out in the Appendix A.

The implemented Runge-Kutta semi-implicit scheme can be summarize as follows. In the first step, the explicitly evaluated residuals are transformed to residuals in primitive variables to form the right-hand side of Equation (2.6). Next, the inversion of the implicit operator yields new residuals in primitive variables, which are transformed to conservative variables. As the final step, the new residuals are used in the Runge-Kutta stage to update the conservative variables.

As an example, Figure 2.1 shows the convergence history of the semi-implicit method with respect of an explicit scheme.

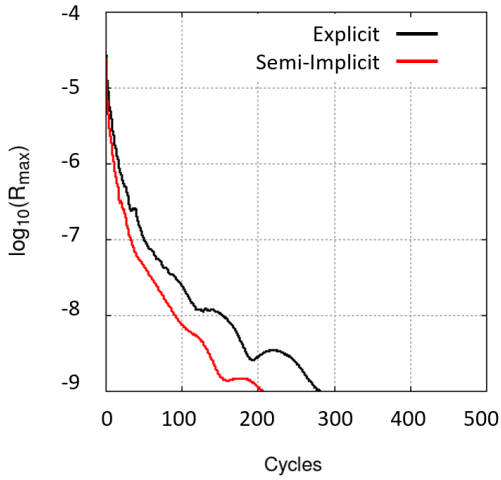

Figure 2.1: Convergence histories of explicit and semi-implicit scheme for a four-stage gas turbine.

2.4 Real gas model

The throughflow code has real-gas capabilities to account for the actual behaviour of the evolving fluid [14]. In this model, the behaviour of real gases, gas mixtures or steam is reproduced by replacing analytic relationships of the perfect gas with the use of gas property tables. For sake of computational efficiency, gas tables are generated off-line and accessed by flow solvers at each

solution step. This approach turned out to be much faster that evaluating thermodynamic properties by means of an analytic equation of state.

The gas database is generated by two-variable formulations based on intensive quantities. A local interpolation of gas data is performed to provide thermodynamic property required by the flow solver in each solution step. In the throughflow code, loss and deviation correlations were reformulated in order to handle real-gas flows.

2.5 Boundary conditions

According to the theory of characteristics, for the solution of incompressible inviscid flows, it is necessary to define a number of boundary conditions equal to that of the governing equations. For a subsonic flow (M<1), four conditions (spanwise distributions of flow angles, total pressure and total temperature) are imposed at the firs row inlet, while the outgoing Riemann invariant is taken from the interior. Instead, at the last row outlet is prescribed only one condition, which is the static pressure at the hub. The spanwise distribution is then determined by the radial equilibrium equation. The density and the three velocity components are extrapolated. On the hub and tip endwalls, the normal velocity is equal to zero in order to satisfy the tangency condition at the wall.

Chapter 3

Three-dimensional Flow Features

This chapter discusses the development of novel models to account for three-dimensional flow effects in the throughflow framework, carried out during the research activity. The 3D flow features that have been considered include secondary flows, tip leakage and shroud effects.

Secondary flows are modelled as additional 3D flow features associated with the vortices that are created when the non-uniform inlet flow is turned by the blade rows. Secondary flow distortions are generated through a transverse velocity field which, in a circumferentially-averaged sense, is assumed to be represented by discrete vortices.

Tip leakage effects for unshrouded blades are modelled in terms of source and sink convective terms in a way that ensures mass and energy conservation. For the case of shrouded blades, the total enthalpy change due to the shroud windage is taken into account.

Secondary and tip leakage losses are provided via correlations and distributed in the meridional flowpath.

3.1 Secondary flows

In the proposed model, secondary flows are included in the circumferentially averaged flow field as additional flow distortions, which are introduced through concentrated Lamb-Oseen type vortices. They are used to generate

a transverse velocity field that deforms the S2 stream surface and locally modifies the blade body force.

The Lamb-Oseen vortex represents an analytical solution of the vorticity transport equation. In a polar coordinate system, whose origin is coincident with the vortex center (Figure 3.1b), the axial and radial velocities are equal to zero, while the tangential velocity is defined as:

$$\tilde{w} = v_\theta = \frac{\Gamma}{2\pi r}\left[1 - \exp\left(\frac{r}{4\nu t}\right)^2\right].$$

One can remove the explicit dependence on time by introducing a characteristic vortex core radius, $z_0 = \sqrt{4\nu t}$, which increases with time as a result of the diffusion of vorticity and shear stresses.

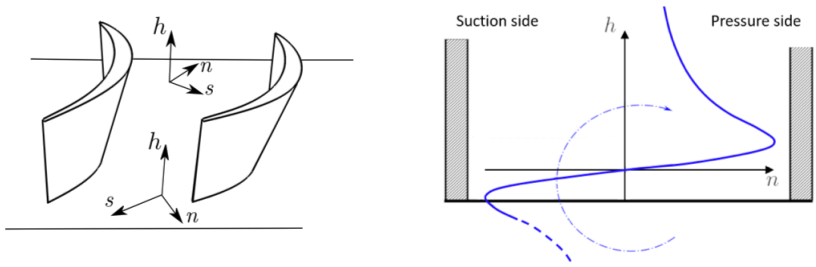

(a) *Intrinsic coordinate system.* **(b)** *Lamb-Oseen vortex.*

Figure 3.1: Secondary flow model.

The circumferentially averaged secondary velocity and vorticity are considered in the intrinsic relative coordinate system (s, n, h) of Figure 3.1a (Hawtorne et al. [31]) and expressed as components w'_n and ω'_s respectively given by:

$$w'_n(\zeta) = \frac{\Gamma}{2\pi z_0 \zeta}\left\{1 - e^{-\zeta^2}\right\}, \tag{3.1}$$

$$\omega'_s(\zeta) = \frac{\Gamma}{\pi z_0^2} e^{-\zeta^2}.$$

The vortex intensity or circulation, Γ, can then be expressed in terms of the vorticity at the vortex center:

$$\Gamma = \pi \omega'_s z_0^2 e^{\zeta^2}.$$

The vorticity component, ω'_s, is assumed to be coincident with the streamwise vorticity of the passage vortex at the blade trailing edge, $\omega'_{s,2}$. This is evaluated using the classical secondary flow theory (Hawthorne et al. [31]) which considers inviscid vortex theory applied to the general case of uniform density flow through a rotating cascade. If the streamwise component of the vorticity in the inlet flow, $\omega'_{s,1}$, is assumed to be negligible relative to the normal component, $\omega'_{n,1}$, then we can write [16]:

$$\omega'_{s,2} = \omega'_{n,1} \frac{\frac{1}{2}\left(\sin 2\beta_2 - \sin 2\beta_1\right) + \left(\beta_2 - \beta_1\right)}{\cos\beta_1 \cos\beta_2},$$

where β_1 and β_2 are, respectively, the inlet and outlet relative flow angles. It must be noticed that, in the Hawthorne's theory, such a vorticity contribution is considered as distributed in the blade passage and not concentrated at the vortex center like in the present approach.

For the evaluation of the normal vorticity at the row inlet, the expression proposed by Smith [3] is adopted:

$$\omega'_{n,1} = k_1 \frac{c_1}{\delta_1} \left(\cos\alpha_1 - \cos\beta_1\right),$$

with c_1 the absolute inlet velocity, δ_1 the inlet endwall boundary layer thickness and k_1 a constant equal to 0.25. Following again what proposed by Smith [3], it is common to assume:

$$\delta_1 = 5\delta_1^*,$$

as a simple relationship between inlet boundary layer thickness and the correspondent displacement thickness, δ_1^*.

The repeating stage assumption is adopted in order to evaluate the endwall boundary layer displacement thickness at each blade row inlet:

$$\frac{\delta_1^*}{h} = \left(\frac{\delta_{rs}^*}{h} - \frac{\delta_{1,in}^*}{h}\right)\left(1 - e^{\frac{n-1}{2}}\right) + \frac{\delta_{1,in}^*}{h},$$

where h is annulus height, $\delta_{1,in}^*$ is the known or assumed value at the meridional flowpath inlet, δ_{rs} is the repeating stage value and n is the blade row number, where $n = 1$ for the first stator, $n = 2$ for the following rotor, etc. [3, 19]. The repeating stage condition is assumed to be reached after an axial distance corresponding to four times the reference length (defined as the axial

chord of the first row).

The vortex characteristic length, z_0, is calculated from the secondary flow penetration depth, Z. Such a quantity is commonly used in correlations to characterize the span fractions, from hub and tip endwalls, that are affected by secondary vortices. In this work, the correlation suggested by Benner [11] is used for that purpose:

$$\frac{Z}{h} = \frac{0.1 F_t^{0.79}}{\sqrt{CR}\, h/c_x} + 32.7 \left(\frac{\delta_1^*}{h}\right)^2,$$

where the loading coefficient, F_t, represents the tangential force per unit length non-dimensionalized by dynamic pressure based on the vector mean velocity, while the convergence ratio, CR, is an approximate measure of the channel acceleration; it is defined as:

$$CR = \frac{\cos\beta_1}{\cos\beta_2}.$$

The vortex characteristic length is assumed to be proportional to the penetration depth:

$$z_0 = c_1 Z,$$

where, on the base of numerical experiments, a value of 0.12 is chosen for the constant c_1. Inside the blade passage, the characteristic length is then distributed linearly along the blade meridional length from the minimum blockage factor location up to the trailing edge [47]. The secondary velocity component given by Equation (3.1) is finally projected in the tangential direction to obtain a tangential velocity $\tilde{w}'$ which is then used in Eq. (1.7) to generate an additional body force. This provides the secondary deviation distribution.

Secondary losses are estimated via correlations like the ones by Benner [12] or Kacker and Okapuu [34, 45]. Secondary loss coefficients are converted in entropy rise values, $\Delta s'$, where local flow conditions at the endwalls are used for this purpose. Such values are then distributed in the spanwise direction so that the integral of the distribution correspond to $\Delta s'$, and the resulting entropy field is used for the distributed loss model. To this end, the following distribution function is used:

$$\Phi(\zeta) = \left\{ \frac{1}{\zeta^2} \left[1 - (1+\zeta^2) e^{-\zeta^2} \right] \right\}^2.$$

It was found that such a distribution, which is suggested by the behaviour of the dissipation in a Lamb-Oseen vortex, closely matches the results of viscous, three-dimensional CFD calculations.

Several parametric studies were carried out in order to check the behaviour of the function Φ and to determine the optimum value of the proportionality constant c_1 between the characteristic vortex core radius and the penetration depth. An example of these studies has been conducted at the rotor blade exit of a gas turbine. In Figure 3.2, viscous, three-dimensional, CFD calculations results are compared to throughflow predictions, in terms of secondary deviation and loss coefficient, for several values of the constant c_1. For these analysis, secondary losses are estimated with the Kacker and Okapuu correlation.

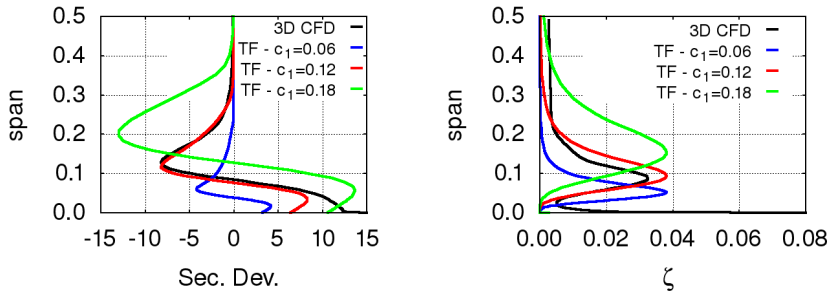

(a) *Secondary deviation.* **(b)** *Loss coefficient.*

Figure 3.2: Comparisons between 3D CFD and throughflow results in terms of spanwise distributions for different values of the c_1 constant.

3.2 Leakage flows

The details of tip leakage flows clearly depend on whether the blades are shrouded or unshrouded. A suitable model for shroud leakage effects can be devised as a combined extraction and reinjection of fluid across the tip section of the blade. Tip clearance effects could be, in principle, accounted for in the throughflow procedure in a fashion similar to that of secondary flows. Unfortunately the correlations available for the tip vortex penetration depth in the spanwise direction and for the induced loss in flow turning by the blade row are characterized by a high level of empiricism and unsatisfactory

agreement between different formulations (e.g. [57, 74]). Therefore it was decided to model tip leakage effects in terms of source and sink flux vectors and additional losses (Figure 3.3).

For unshrouded rotors, those terms are introduced in the streamwise row of cells adjacent to the tip endwall, where the height of those cells is enforced to be equal to the tip gap height by the grid generation procedure. For shrouds or hub seals, the sink and source vectors are applied separately in cells belonging slots located upstream and downstream of the blade row.

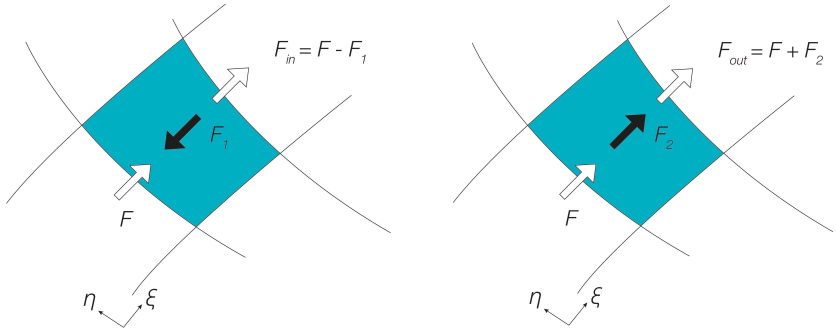

(a) *Sink flux model.* **(b)** *Source flux model.*

Figure 3.3: Leakage model.

If we consider a mesh cell in the tip gap, the total flux contribution in ξ and η directions of the computational plane becomes:

$$F - F^*_{sink} + F^*_{source}$$

$$G - G^*_{sink} + G^*_{source}$$

where F and G are the convective fluxes (Equation (1.1)), while F^* and G^* are the source or sink flux vectors, defined as:

$$F^* = \begin{bmatrix} \rho^* U^* \\ \rho^* U^* u^* \\ \rho^* U^* v^* \\ \rho^* U^* w^* \\ \rho^* U^* H^* \end{bmatrix}, \qquad G^* = \begin{bmatrix} \rho^* V^* \\ \rho^* V^* u^* \\ \rho^* V^* v^* \\ \rho^* V^* w^* \\ \rho^* V^* H^* \end{bmatrix}. \tag{3.2}$$

For the sink terms, the leakage mass flow rate is specified, while values of pressure and temperature are assumed equal to those of the main flow. For the source terms, the mass flow rate and the direction of the leakage flow are specified. For tip clearance flows this is assumed to be normal to the camber line of the tip section of the blade. For shroud or hub seals leakages the jet direction is specified by assigning a flow angle in the meridional plane and prescribing the tangential velocity obtained from an angular momentum balance that accounts for cavity windage effects. The momentum source intensity is calculated as:

$$q^* = \rho^* c^* = \frac{\dot{m}_l}{S},$$

where S is the total injection area orthogonal to the leakage flow direction defined as:

$$S = \sum \left[b \left(a_x \nu_x + a_y \nu_y \right) \right],$$

with a_x and a_y the projections of the cell area in the axial and radial direction, while ν_x and ν_y the components of the unit vector that defines the local jet direction. For real gases and vapours, the local value of density is determined from the implicit relations:

$$h^* = H^* - \frac{q^{*2}}{\rho^*}, \qquad \frac{1}{\rho^*} = \nu \left(\rho^*, h^* \right),$$

which are solved iteratively using a shooting method, while for ideal gases it is calculated analytically by solving a quadratic equation:

$$\rho^* = \frac{c_p p + \sqrt{c_p^2 p^2 + 2 H^* q^*}}{2 H^*}.$$

The velocity components are evaluated as:

$$u^* = \frac{q^*}{\rho^*} \nu_x, \qquad v^* = \frac{q^*}{\rho^*} \nu_y, \qquad w^* = \frac{q^*}{\rho^*} \nu_z.$$

Leakage losses are estimated from correlations, like the ones by Yaras e Sjolander [74] or Denton [21], and distributed linearly along the blade axial chord. In order to define a distribution in the spanwise direction, it is assumed that losses are concentrated where tip leakage effects are important. When source fluxes are imposed, the relative flow angle departs from that defined

by the flow tangency condition to the S2 streamsurface for a certain extent of the meridional flowpath. To identify these regions of the computational domain, a function of the spanwise coordinate is constructed as follows:

$$T(h) = \left| \frac{w}{\tilde{w} + \tilde{w}'} \right| - 1,$$

where $\tilde{w}$ and $\tilde{w}'$ are given by Equations (1.6) and (3.1), respectively. Far from the tip gap affected region, the tangential velocity component, w, is equal to $\tilde{w} + \tilde{w}'$ due to the action of the body forces, and $T = 0$. Where the tangential momentum is modified by the effects of the source terms of Equations (3.2), w is different from $\tilde{w} + \tilde{w}'$ and $T > 0$. In the regions of the meridional flowpath where such a condition is satisfied, local loss contributions are determined by area-averaging the total leakage loss.

As an example, contours of the T function and entropy distribution at the trailing edge of a gas turbine rotor blade, are reported in Figure 3.4.

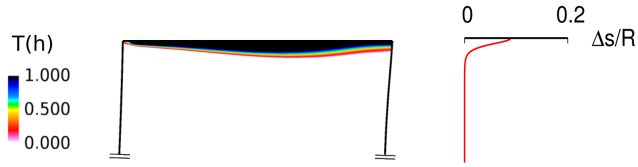

Figure 3.4: Tip clearance loss distribution and entropy at the trailing edge of a turbine rotor blade.

3.2.1 Unshrouded blades

The leakage mass flow rate over unshrouded blades is expressed by the formulation suggested by Denton [21] in the limit of incompressible leakage flow:

$$\dot{m}_l = c_d A \sqrt{2\rho\Delta p},$$

where c_d is a discharge coefficient. In the present work, the estimation proposed by Yaras and Sjolander was adopted [74]. As reported in Figure 3.5, the variation of c_d is expressed as a function of the tip gap height and the blade maximum thickness. A typical value is about 0.7 - 0.8.

The pressure difference between the pressure and suction side of the blade tip section, Δp, is related to the tangential component of the local blade

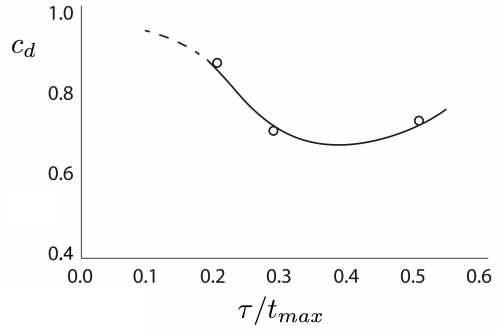

Figure 3.5: Variation of gap discharge coefficient with clearance for Yaras and Sjolander cascade.

body force at the tip blade, f_θ, known from the conservation of momentum equation. According to the equation (1.2), it is possible to write:

$$\Delta p = \frac{2\pi r}{N} \rho b f_\theta,$$

where r is the blade tip radius, N is the number of blades and b is local blockage factor. In order to ensure energy conservation, the total enthalpy value is assumed equal to that of the main flow.

Two tip clearance loss formulations have been considered. The firs one, by Yaras e Sjolander [74], is based on kinetic energy losses:

$$\zeta_{\mathrm{YS}} = \frac{2}{\dot{m} V^2} \left(\frac{2}{\rho}\right)^{0.5} C_d \tau \int_0^{c_x} (P_p - P_s)^{1.5}\, dx.$$

The second formulation is due to Denton [21] and it is based on a mixing analysis:

$$\zeta_{\mathrm{D}} = \frac{2}{\dot{m} V^2} \rho C_d \tau \int_0^{c_x} V_s^2 \left(1 - \frac{V_p}{V_s}\right) \sqrt{V_s^2 - V_p^2}\, dx.$$

If we approximate the relative flow velocity at the blade tip as the average between the V_s and the V_p, it is possible to write:

$$\begin{cases} V = \frac{1}{2}\left(V_s + V_p\right) \\ \Delta P = \frac{1}{2}\rho (V_s^2 - V_p^2), \end{cases}$$

and so, solving by substitution, we obtain:

$$\begin{cases} V_p = 2V - V_s \\ V_s = \frac{\Delta P}{2\rho V} + V. \end{cases}$$

Figure 3.6 shows an example of the results obtained, with the proposed clearance treatment, at the trailing edge of a turbine rotor. The strong impact of the leakage effect is well evidenced by relative flow angle distribution with and without tip clearance.

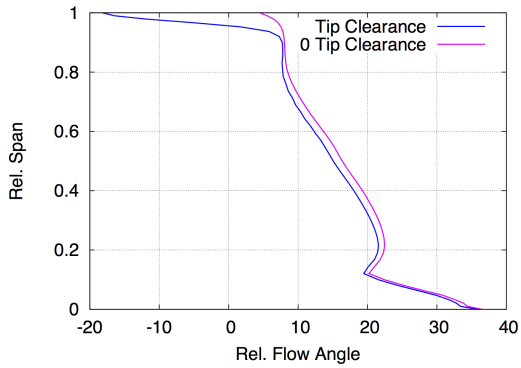

Figure 3.6: Relative flow angle at the trailing edge of a turbine rotor with and without a tip gap of 1% of the blade span.

3.2.2 Shrouded blades

In the case of shrouds and hub seals, the leakage mass flow rate is determined by the formulation proposed by Stodola [66]:

$$\dot{m}_l = \frac{A_l C_c}{\sqrt{N_{teeth}}} \sqrt{p_{in}\rho_{in}\left(1 - \left(\frac{p_{ex}}{p_{in}}\right)^2\right)},$$

where N_{teeth} is the number of teeth and C_c is an adequate contraction coefficient, which ranges typically from 0.6 to 0.8. The seal throat area is given by:

$$A_l = \frac{2\pi \bar{r} g}{N_b},$$

with g is the gap between the seal and the endwall and $\bar{r}$ is the average cavity radius. The seal throat area is given by:

$$\bar{r} = \frac{r_R + r_S}{2}.$$

In addition to the leakage flow rate, it is important to predict the swirl velocity and the total enthalpy at the exit of the shroud, because they have a strong influence on the mixing loss, caused by the interaction between the mainstream and the leakage flow [21]. In the present work, an angular momentum balance is applied to determine the swirl velocity variation through the shroud cavity. As shown in Figure 3.7, the shroud cavity is composed of a stationary and rotating part.

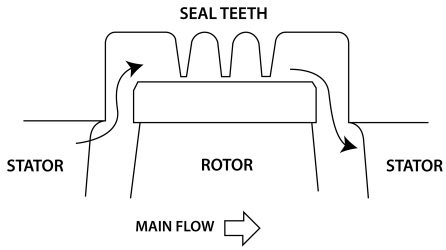

(a) *Turbine rotor.*

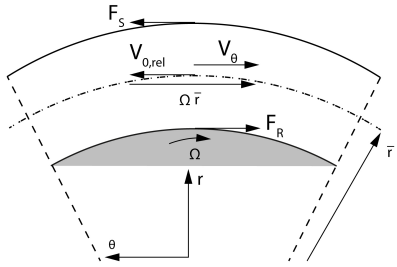

(b) *Annular cavity.*

Figure 3.7: Seal cavity geometry.

The moment acting on the control volume, M, must be equal to the angular momentum of the fluid passing through the control volume itself:

$$-\left(M_S + M_R\right) = \dot{m}_l \; \bar{r} \left(v_{\theta,ex} - v_{\theta,in}\right), \tag{3.3}$$

where:

$$M = \int_0^{l_s} \tau r \, dA \simeq \tau 2\pi \bar{r}^2 l_s.$$

The skin friction coefficient on both the shroud and the casing surfaces is converted in a wall shear stress, which can be defined as:

$$\tau = C_f \frac{1}{2} \rho \bar{v}_\theta^2 sgn\left(\bar{v}_\theta\right),$$

where $\bar{v}_\theta$ is the average core velocity, defined as:

$$\bar{v}_\theta = \frac{v_{\theta,in} + v_{\theta,ex}}{2}.$$

The turbulent nature of the flow is computed introducing the hydraulic diameter on the basis of smooth pipes. The present model switches between two different laws proposed by Blausius and Schultz-Grunow, depending on circumferential Reynolds number:

$$C_f = \begin{cases} 0.0791 \; Re_D^{1/4}, & \text{se } 4000 \leq Re_D < 10^5 \quad \text{(Blasius)} \\ 0.0456 \; Re_D^{1/5}, & \text{se } 10^5 \leq Re_D \leq 10^7 \quad \text{(Schultz-Grunow).} \end{cases}$$

It is important to point out that, when considering the rotating part of the cavity, the relative tangential velocity,

$$\bar{v}_{\theta,rel} = \left(\bar{v}_\theta - \Omega \bar{r}\right),$$

is used to compute τ and Re_D. From equation (3.3), it is possible to determine the swirl velocity at re-entry in the mainstream:

$$v_{\theta,ex} = v_{\theta,in} - \left(\frac{M_S + M_R}{\dot{m}_l \; \bar{r}}\right).$$

Once the torque produced about the rotor axis is calculated, for an adiabatic case, the total enthalpy rise is given by the energy equation:

$$\Delta h_0 = \frac{\dot{W}}{\dot{m}_l} = \frac{M_R \; \Omega}{\dot{m}_l}.$$

In this way, the leakage flow is then re-injected in the mainstream by imposing the mass flow rate, $\dot{m}_l$, the total enthalpy, $h_{0,ex}$, and the swirl velocity, $v_{\theta,ex}$.

As an example, contours of entropy downstream of the trailing edge of a shrouded turbine rotor blade, are reported in Figure 3.8.

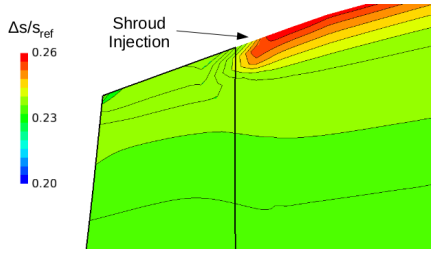

Figure 3.8: Entropy contours downstream of the trailing edge of a shrouded turbine rotor blade.

Chapter 4

Coolant Injections and Purge Flows

This chapter describes the strategy that has been developed in this research activity to include coolant ejections for gas turbine components refrigeration in the proposed throughflow framework. Coolant ejections in the meridional flowpath are modelled, on a local basis, via source terms vectors. To do this, an approach which is similar to the one discussed for leakage flows (Chapter 3.2) is adopted.

In order to properly model the complex cooling schemes that characterize modern gas turbines, two different models have been considered: endwall slots and blade jets. Endwall slots are employed to simulate purge cavity flows, while blade jets account for the presence of film cooling slots, trailing edge slots, and blade tip ejections. In the case of endwall slots, the axial position and length of the slot is specified and the source term vectors are applied in cells, adjacent to hub and tip endwalls, that belongs to the slot. For the case of blade jets, the source term vectors are applied in prescribed spanwise rows of grid cells. It must be noticed how, contrary to a 3D CFD approach, where there is a distinction between the pressure side and the suction side injections, here, in the throughflow approach, only the circumferentially-averaged effect of blade jets is considered.

Losses related to the mixing of coolant jets with the mainstream are taken into account by correlations and are distributed in the meridional flowpath.

As an inviscid flow model, like the one adopted in this work, does not provide any diffusion; a suitable mixing model is necessary to obtain a realistic

redistribution of the coolant injections effects in terms of total temperature and entropy. This will be described in a following Chapter of this thesis.

4.1 Coolant flows model

For a computational cell interested by flow injection (Figure 4.1), the total flux contributions the in ξ and η directions of the computational plane becomes:

$$\mathcal{F}_{out} = \mathcal{F}_{in} + \mathcal{F}^*$$

$$\mathcal{G}_{out} = \mathcal{G}_{in} + \mathcal{G}^*$$

where $\mathcal{F}_{in}$ and $\mathcal{G}_{in}$ are the convective fluxes, while F^* and G^* are the source flux vectors identifying the jet quantities, which are given by:

$$\mathcal{F}^* = \begin{bmatrix} \rho^* U^* \\ \rho^* U^* u^* \\ \rho^* U^* v^* \\ \rho^* U^* w^* \\ \rho^* U^* H^* \end{bmatrix}, \qquad \mathcal{G}^* = \begin{bmatrix} \rho^* V^* \\ \rho^* V^* u^* \\ \rho^* V^* v^* \\ \rho^* V^* w^* \\ \rho^* V^* H^* \end{bmatrix}.$$

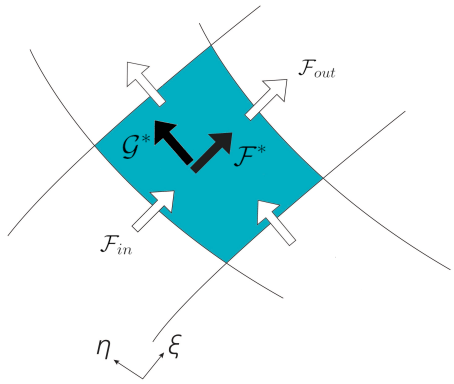

Figure 4.1: Flux balance in injected cell.

The total jet mass flow rate, $\dot{m}_c$, the total temperature, T^*, and the jet direction are specified, while the local jet pressure is assumed equal to that

of the main flow. The jet momentum is computed as:

$$q^* = \rho^* c^* = \frac{\dot{m}_c}{S},$$

where S is the total injection area:

$$S = \sum \left[b \left(a_x \nu_x + a_y \nu_y \right) \right],$$

with a_x and a_y the projections of the cell area in the axial and radial direction, respectively, while ν_x and ν_y the components of the unit vector that defines the local flow direction of the jet.

The jet swirl and meridional angles are actually assigned in the case of endwall slots, while for the case of blade jets the flow direction is assumed coincident with that of the local streamline. The local value of the jet density is computed as:

$$\rho^* = \frac{c_p p + \sqrt{c_p^2 p^2 + 2H^* q^*}}{2H^*}.$$

4.2 Coolant mixing loss model

Mixing losses due to coolant ejections at the trailing edge, purge flows, and film cooling have been considered in the present work.

The coolant-main-stream mixing loss is usually estimated using the method of Hartsel [30]. This is based on the Shapiro theory of one-dimensional flow with mass addition [59], and the result is usually expressed in terms of total pressure. However, for throughflow methods, it is much easier to work directly with entropy as a quantifier of loss. Denton [21] and Young and Wilcock [75, 76] proposed a practical correlation for determining the entropy generation rate in the mixing of coolant and mainstream flow. Here, the formulation of Denton is applied:

$$\Delta S = \gamma R M_m^2 \left(1 - \frac{V_c}{V_m} \cos\theta \right) \frac{\dot{m}_c}{\dot{m}_m},$$

where M_c is the Mach number at local mainstream conditions, $\dot{m}_c$ and $\dot{m}_m$ are, respectively, the mass flow rate of coolant and of the local mainstream, and θ is the angle of injection coolant from mainstream direction.

For purge flow injections, the corresponding entropy rise is distributed

along streamlines following the procedure described for leakage losses (Chapter 3.2) and assuming a linear decay in the streamwise direction. Instead, for film cooling injections, the mixing losses are treated as constants in the spanwise direction for all the injected cells, with a linear decay in the streamwise direction.

4.3 Coolant efficiency

In order to compute stages and turbine overall performance, a new formulation has been adopted [58]. The work done on the rotor can be evaluated either by integrating pressure and shear forces on all the rotating surfaces to compute the torque, or with an enthalpy balance on a control volume including the blade row. Here the specific work is computed from an enthalpy balance, and defined as:

$$W = \frac{\dot{m}_{in} h_{0,in} + \sum_{i=1}^{N_i} \left(\dot{m} h_0\right)_i - \sum_{i=1}^{N_e} \left(\dot{m} h_0\right)_i - \dot{m}_{ex} h_{0,ex}}{\dot{m}_{in}},$$

where N_i and N_e are the number of injections end extractions, while $\dot{m}_{in}$ end $\dot{m}_{ex}$ are the injected end extracted mass flow rate. The total-to-total efficiency is defined as:

$$\eta_{tt} = \frac{\dot{m}_{in} h_{0,in} + \sum_{i=1}^{N_i} \left(\dot{m} h_0\right)_i - \sum_{i=1}^{N_e} \left(\dot{m} h_0\right)_i - \dot{m}_{ex} h_{0,ex}}{\dot{m}_{in} h_{0,in} + \sum_{i=1}^{N_i} \left(\dot{m} h_0\right)_i - \sum_{i=1}^{N_e} \left(\dot{m} h_0\right)_i - \dot{m}_{ex} \bar{h}_{0,ex,s}},$$

where $\bar{h}_{0,ex,s}$ is a mass averaged isentropic total enthalpy defined as:

$$\bar{h}_{0,ex,s} = \frac{\dot{m}_{in} h_{0,ex,s} + \sum_{i=1}^{N_i} \left(\dot{m} h_{0,ex,s}\right)_i}{\dot{m}_{in} + \sum_{i=1}^{N_i} \dot{m}_i},$$

and $h_{0,ex,s}$ is the total enthalpy of each of the inlets expanded isentropically to the mainstream mass average total pressure at exit.

Chapter 5

Radial Mixing

Secondary and leakage flow are modeled in the throughflow methods as additional three-dimensional flow features whose effects are concentrated in selected regions of the meridional flowpath. This is not sufficient to ensure a realistic representation of the spanwise distributions of flow quantities. As discussed in several studies since three decades [3], the radial migration of the endwall flow plays a crucial role in determining the spanwise redistribution of flow distortions and losses in multistage turbomachinery.

A radial mixing model is therefore an important feature to be considered in a throughflow code. In the present research activity, the effect of the mixing is introduced via diffusive terms in the momentum and energy equations.

5.1 Viscous stresses

The viscous stress is originated from the friction between the fluid and the surface of an element. In the model proposed, only the components acting on the radially inward and outward facing surfaces of the fluid element is considered in the formulation:

$$\overline{\tau} = \begin{bmatrix} \tau_{xx} & \tau_{xr} & \tau_{x\theta} \\ \tau_{rx} & \tau_{rr} & \tau_{r\theta} \\ \tau_{\theta x} & \tau_{\theta r} & \tau_{\theta\theta} \end{bmatrix}.$$

If the fluid is assumed to be axisymmetric, the components of the viscous stress tensor are defined by the relations:

$$\tau_{xr} = \tau_{rx} = \mu_t \left(\frac{\partial v}{\partial x} - \frac{v}{r} \right)$$
$$\tau_{x\theta} = \tau_{\theta x} = \mu_t \left(\frac{\partial w}{\partial x} + \frac{\partial u}{\partial \theta} \right)$$
$$\tau_{r\theta} = \tau_{\theta r} = \mu_t \left(\frac{\partial v}{\partial \theta} \right)$$

in which μ_t represents the dynamic viscosity coefficient. It is important to observe that the normal stresses are related only to the static pressure:

$$\tau_{xx} = \tau_{rr} = \tau_{\theta\theta} = p.$$

The vector of the viscous fluxes, which contains the viscous stress as well as the heat diffusion, is introduced in the system of governing equation (1.1). The total contribution in η direction of the computational plane is:

$$F_v = \begin{bmatrix} 0 \\ \tau_{xr} \\ \tau_{xr} \\ \tau_{x\theta} + \tau_{r\theta} \\ \Theta_x + \Theta_r \end{bmatrix}.$$

where:

$$\Theta_x = v\tau_{xr} + k_t \frac{\partial T}{\partial x}$$
$$\Theta_r = u\tau_{xr} + k_t \frac{\partial T}{\partial r}$$

are terms describing the work of the viscous stresses and of the heat conduction in the fluid, respectively. The time step limitation due to diffusive terms is taken into account and treated like in [6].

5.2 Mixing coefficient

Historically, two classes of models have been proposed for determining the mixing coefficient: Adkins and Smith [3] assumed that a spanwise redistribu-

tion process was completely deterministic and associated to secondary flows; Gallimore and Cumpsty [27] took a different view of the mechanism causing radial mixing that it was dominated by a random, turbulent type, diffusion process. Finally, the work of Lewis [35, 36], which is the one proposed in this work, considers the spanwise transport as a result of both turbulent diffusion and convective mechanism due to secondary flow:

$$\epsilon = \epsilon_d + \epsilon_{sf}. \tag{5.1}$$

The spanwise transport of any circumferentially averaged fluid property, e.g., stagnation enthalpy, can be expressed in the streamwise direction as:

$$V_m \frac{\partial Q}{\partial m} = \epsilon \frac{\partial^2 Q}{\partial y^2}.$$

The value of the diffusion coefficient, ϵ, was determined with a similar approach to that of Gallimore and Cumpsty [27, 26], where the production of turbulence is related to the generation of entropy. Assuming a typical length scale L_d of turbulence eddies, the expression for ϵ_d is taken by:

$$\frac{\epsilon_d}{V_z L_s} = k \left(\frac{T_2 \Delta s}{V_z^2} \right)^{1/3} \left(\frac{L_d}{L_s} \right)^{4/3},$$

where k is a constant equal to 0.9 and L_s is the stage length. An estimate of the length scale can be determined from the profile loss coefficient, Y, the blade pitch, p, and the blade exit flow angle, α_2:

$$L_d = 5 Y_p p \cos \alpha_2.$$

For the spanwise convection coefficient, it is assumed that the redistribution process linked to secondary flow has a nature similar to turbulent mixing. The expression for ϵ_d is obtained:

$$\frac{\epsilon_{sf}}{V_z L_s} = k \left(\frac{\Delta^2 p^* f\left(\delta / p^*\right)}{h V_z \cos^2 \alpha_1} \right)^{1/2} \frac{p^*}{L_s},$$

where k is a constant equal to 0.02, h is the semi-span blade height, p^* is the throat of the cascade and $f\left(\delta / p^*\right)$ is a series expansion with the form shown in Figure 5.1. The expression of Δ is related to the secondary kinetic energy, which is determined by considering the three-dimensional flow vortex model

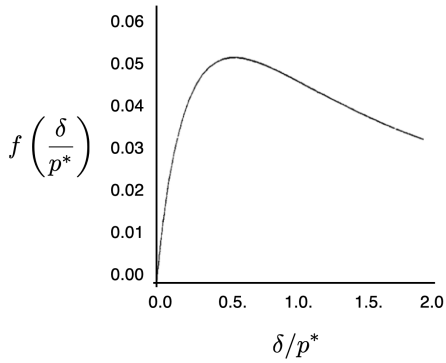

Figure 5.1: Function of inlet boundary layer thickness.

presented in Chapter 3. In particular, for hub section, the secondary vortex contribution, while for the tip section, the secondary and leakage vortex contributions.

The physical process, that are being represented by the mixing model, are introduced in the system of governing equation by an eddy viscosity μ_t and a thermal conductivity k_t. A Bousinnesq type assumption is adopted to express the Reynolds stress tensor, where the mixing coefficient, ϵ, is related to the eddy viscosity by the turbulent Schmidt number:

$$Sc_t = \frac{\mu_t}{\rho\epsilon}.$$

The thermal conductivity is then calculated using the Reynolds analogy, by the turbulent Prandtl number:

$$Pr_t = \frac{\mu_t C_p}{k_t}.$$

In the present work, the contribution of each blade row is calculated separately and cumulated from the first to the last one. A Gaussian function is employed, so that the decay of the contribution of a given blade row is spread over 1.5 axial chords, c_{ax}, downstream. It can be expressed as:

$$\Phi\left(x\right) = \epsilon_i \exp\left(\frac{(x - x_f)^2 \log\frac{\epsilon_f}{\epsilon_i}}{c_{ax}^2}\right)$$

The experimental evidence suggests that Pr_t and Sc_t should be of the order to the unity [13]. Numerical experiments conducted over a range of multistage turbines have shown how a value of $Pr_t = 2.0$ gives radial distributions of entropy that are in good agreement with 3D CFD results. Figure 5.2 compares results obtained with throughflow and TRAF codes in an annular duct with a jet at the inner endwall. Except for the region very close to the wall, where the viscous boundary-layer effects are visible in the 3D CFD solution, the radial distributions of total temperature (Fig. 5.2a) and total pressure (Fig. 5.2b), taken 10 slot lengths downstream the injection location, appear in very good agreement.

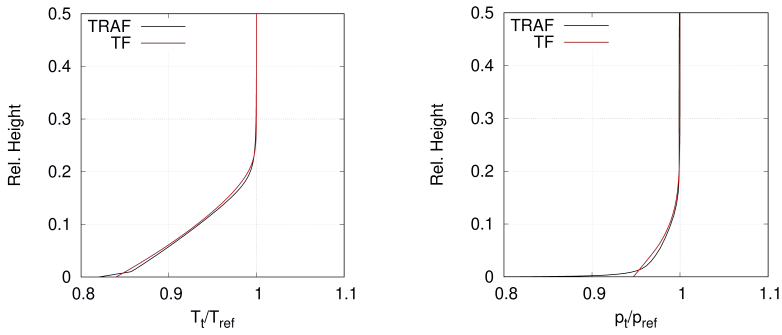

(a) *Total temperature.* **(b)** *Total pressure.*

Figure 5.2: Radial distributions for an annular duct with wall jet.

Chapter 6

Data matching and off-design analisys procedures

This chapter describes the strategy developed during the research activity for the off-design analysis of multistage steam and gas turbines using the proposed throughflow method. The strategy starts from the calibration of the throughflow framework in order to match the results of a 3D CFD analysis at design point. To this end, steady multistage viscous calculations are considered and the design point data match is achieved by extracting flow features from the circumferentially averaged three-dimensional solution and prescribing them as inputs to the throughflow code. Such flow features are:

- the S2 flow surface;
- the aerodynamic blockage distribution;
- the loss distribution.

The *thin-layer* approximation is adopted for the reference 3D CFD calculations at nominal conditions. It consists in neglecting viscous fluxes in the curvilinear coordinate corresponding to the spanwise direction, while retaining them in the blade-to-blade plane. Such an approach guarantees the consistency of the computed flow surface with the throughflow model. Also, it eliminate the strong distortions that arises in the endwall boundary-layer region when a full Navier-Stokes solution is adopted. This matching procedure has been completely automated and does not require any user input. Once the data match has been achieved, the throughflow framework is frozen and used for off-design simulations.

In order to consider the change in the cooling air properties due to the various turbine operating conditions, an approximate method has also been implemented in the throughflow framework.

6.1 Stream Surface

For off-design predictions, the flow surface is extracted from a circumferentially averaged 3D CFD solution at design point. In particular, the flow surface, $\tilde{\Gamma}(x, r)$, is obtained from the tangency condition to the circumferentially-averaged relative velocity field:

$$\tilde{u}\frac{\partial\tilde{\Gamma}}{\partial x} + \tilde{v}\frac{\partial\tilde{\Gamma}}{\partial r} = \frac{\tilde{w}}{r} - \Omega.$$

For the numerical solutions, it is convenient to add a time dependent term so that an evolution equation for Γ is obtained:

$$\frac{\partial\tilde{\Gamma}}{\partial t} + \tilde{u}\frac{\partial\tilde{\Gamma}}{\partial x} + \tilde{v}\frac{\partial\tilde{\Gamma}}{\partial r} = \frac{\tilde{w}}{r} - \Omega. \tag{6.1}$$

This (linear) equation can be conveniently integrated by using a second-order implicit scheme; more details can be found in Appendix B.

An example of the calculated streamsurface for a four-stage turbine is reported in Figure 6.1, with superimposed Mach number contours.

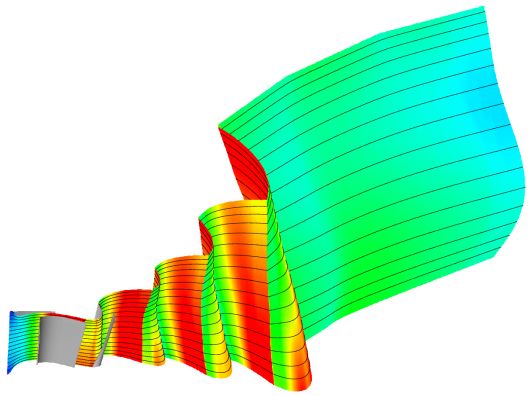

Figure 6.1: S2 streamsurface for a four-stage turbine with superimposed Mach number contours.

The streamsurface obtained at nominal condition is kept fixed for the off-design analysis and adjusted only to accommodate incidence effects. This implies that the outlet relative flow angles for the blade rows are kept constant for all the considered operating conditions, and the flow deviation is thus kept equal to the one predicted by the 3D CFD calculation at design point. A consequence of the *Thin-Layer* assumption to produce the reference 3D solution is the lack of secondary flow effects in the resulting stream surface. Such effects are introduced in the throughflow procedure as additional flow features as described in Chapter 3.

6.2 Aerodynamic Blockage

As for the streamsurface, in analysis problems, the tangential blockage distribution can be deduced from the three-dimensional CFD solution. The steady continuity equation for an axysimmetric flow with tangential blockage is written as:

$$\frac{\partial \rho u b}{\partial x} + \frac{\partial \rho v b}{\partial r} = 0. \tag{6.2}$$

If we consider a target flowfield to be matched by the throughflow calculation (e.g. an axysimmetric flowfield obtained by circumferentially averaging a 3D CFD solution) due to the averaging process, the axisymmetric quantities ρ, u and v are not expected to satisfy equation (6.2) if the geometric blockage factor is used. It is possible to re-write equation (6.2) in order to determine the blockage distribution $b = b(x, r)$:

$$\frac{\tilde{u}}{b}\frac{\partial b}{\partial x} + \frac{\tilde{v}}{b}\frac{\partial b}{\partial r} = -\frac{\nabla\left(\tilde{\rho}\cdot\tilde{c}\right)}{\tilde{\rho}}.$$

A more convenient, time-dependent form in curvilinear coordinates is:

$$\frac{\partial \chi}{\partial t} + \tilde{U}\frac{\partial \chi}{\partial \xi} + \tilde{V}\frac{\partial \chi}{\partial \eta} = -\frac{\Delta}{\tilde{\rho}}, \tag{6.3}$$

where $\chi = \ln b$ and $\Delta = \nabla\left(\tilde{\rho}\cdot\tilde{c}\right)$. It is worthwhile to notice how this equation is formally identical to equation (6.1) so that they can be solved with the same procedure, as reported in Appendix B. This is a favourable circumstance that simplifies the post-processing chain needed to extract input data for the throughflow code from the 3D CFD solution.

Finally, the tangential aerodynamic blockage distribution is obtained as:

$$b\,(x, r) = e^{\chi}.$$

Such a distribution takes into account the displacement effects of boundary layers and sensibly improves the matching between throughflow predictions and the reference 3D CFD solution.

The comparison between spanwise distributions of aerodynamic and geometric blockage for a turbine blade at 50% axial chord is reported in Figure 6.2.

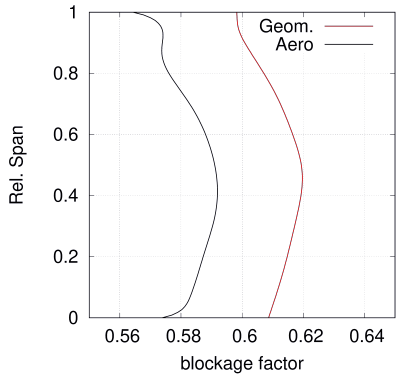

Figure 6.2: Aerodynamic and geometric blockage for a turbine blade.

6.3 Loss distribution

The entropy change due to viscous losses occurring inside blade rows is derived from correlations, but, in order to match a CFD solution, the entropy field calculated from the tangentially-averaged 3D flowfield is normalized and used to distribute the entropy increase along streamlines. The entropy increase computed from correlations for each blade row is also scaled to match the 3D CFD results. The entropy distribution and the scaling factor for each blade row are determined at nominal conditions and then kept fixed when analysing the off-design operation of the turbine. Figure 6.3 reports the comparison between the prescribed entropy distribution and the one computed from the throughflow results for an uncooled turbine stage at midspan.

The described procedure addresses essentially the matching of the profile loss distributions. As for the other loss sources, they are calculated and distributed by using the methodologies described in Chapter 3.

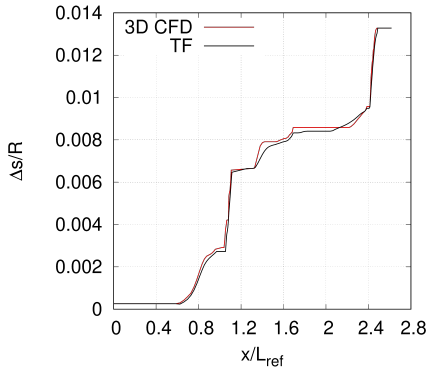

Figure 6.3: Prescribed (from 3D CFD analysis) and calculated (from throughflow results) entropy distributions.

6.4 Cooling scheme

The cooling air mass flow rate and properties in off-design condition should in principle be obtained, for each injection slot, from proper analyses of the secondary air system of the particular gas turbine power plant. This is a complex and time-consuming process that is hardly suited for preliminary off-design studies during design phases, especially when the range of considered operating conditions is wide. While cooling air properties can be roughly estimated at each operating conditions by simple cycle analyses, the determination of coolant mass flow rates requires dedicated studies of the fluid system that brings the air to the ejection slots. In order to overcome this difficulty, an approximate method to avoid the estimation of coolant mass flow rates has been implemented in the throughflow method. The cooling air mass flow rate is simply expressed as a fraction of the inlet mass flow rate to the turbine. The value of such a fraction is determined at design condition and kept fixed in off-design analyses.

Chapter 7

Validation

As a validation of the proposed methodology, the throughflow code was used to study three experimental test cases. Each test allows us to the assessment of the various physical models included in the framework.

The first one is the T106 high-lift, low-pressure turbine blade, used to assess the secondary flow modelling approach. The second one is a subsonic high-pressure steam turbine stage, the KTH 4b, which allows us to highlight the average effect of three-dimensional flow features, like leakage effects and purge flows. The last one is a high-pressure transonic gas turbine, the CT3 stage, which allows us to analyse the radial mixing model and the predictive capability of the solver at off-design conditions.

In the majority of the cases, the geometry of the blades is available as airfoil coordinates corresponding to cylindrical or conical sections of the blade itself. This is convenient for extracting the meridional blockage distribution, but for constructing the S2 flow surface, the mean blade surface is needed. Moreover, loss and deviation correlations are expressed in terms of blade section parameters (like the maximum thickness, throat opening, unguided turning, etc.). In order to determine such parameters from the airfoil coordinates, a geometrical approach to the reverse engineering of turbine blade profiles has been developed during the present research activity. It is described in Appendix C.

7.1 T106 Turbine Cascade

The linear cascade under investigation is based on the T106 blade section which was tested experimentally by Duden and Fottner [24] in a high speed wind tunnel in two configurations: one with parallel endwalls and one with divergently tapered endwalls. Due to the evidence of stronger secondary flow, the configuration discussed here is the tapered one, with an outlet-inlet area ratio of $A_{TE}/A_{LE} = 1.203$ and a symmetrical taper angle of $\lambda = 15°$.

Table 7.1 and Figure 7.1 show the geometric and aerodynamic specifications of the design data of the linear cascade. The exit isentropic Mach number is $Ma_{2,is} = 0.59$, while the Reynolds number is $Re_{2,is} = 5 \cdot 10^5$.

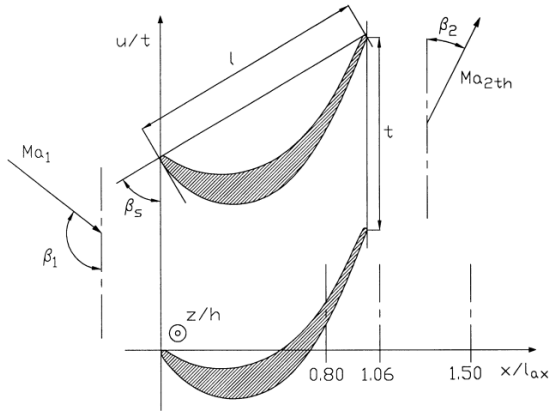

Figure 7.1: Cascade geometry of the T106 blade [24].

Table 7.1: Geometrical parameters of blade in the T106 Test Turbine.

	Blade
Number of blades	7
Axial chord [mm]	85.92
Stagger angle [deg]	59.28
Aspect ratio	2.273

7.1.1 Discussion of results

For the meridional analysis of this linear cascade the governing equations were recasted in a suitable form: the axisymmetric terms were dropped out while blockage and body force source terms were retained. At the inlet, the experimental values of the total quantities and the flow angle are imposed: $T_{t,1} = 312.9$ K, $P_{t,1} = 0.4754$ *bar* and $\beta_1 = 127.7°$. At the outlet, the static pressure, also obtained from experiments, is set as $P_{t,2} = 0.3793$ *bar* and assumed uniform along the span, without the radial equilibrium theory.

The blade mean surface and the blockage distribution were obtained from the three-dimensional geometry of the cascade. The meridional channel was discretized with 120 grid cells in the axial direction, with 64 cells in the blade passage. Due to the symmetrical geometry of the endwalls and inlet conditions, only half of the blade height was considered and it was discretized with 64 spanwise cells.

Inlet boundary layer thicknesses and vorticity were deduced from the spanwise velocity distribution measured upstream of the cascade. They were used for the correlations by Benner, and Kacker-Okapuu for the secondary flow penetration depth and loss coefficient [11, 34] and in the Hawthorne formula [31] for the streamwise vorticity at the trailing edge.

The capability of the secondary flow model to produce realistic spanwise distributions can be appreciated in Figure 7.2, where computed secondary deviation and total pressure loss coefficient are compared to experiments. The experimental deviation distribution (Figure 7.2a) is quite well reproduced by the throughflow analysis. A secondary flow model with only one vortex cannot account for non symmetric effects and this, for the analysed configuration, results in an underestimation of the flow underturning near the 15% of the blade span. The prediction by the Benner correlation for the spanwise penetration depth appears to be quite accurate. In terms of total pressure loss coefficient, Figure 7.2b, the prediction based on the correlation by Kacker-Okapuu is in good agreement with measurements. Instead, the Benner's correlation results in a serious underestimation of the loss peak which is recorded near the 15% of the span. Remarkable is the good reproduction of the shape of the loss distribution, except for the first 5% span where the experimental results are affected by the endwall boundary layer, which is not accounted for in the throughflow analysis.

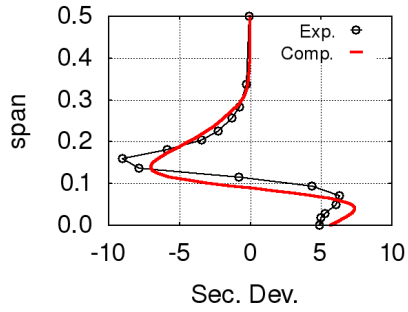

(a) *Secondary deviation.*

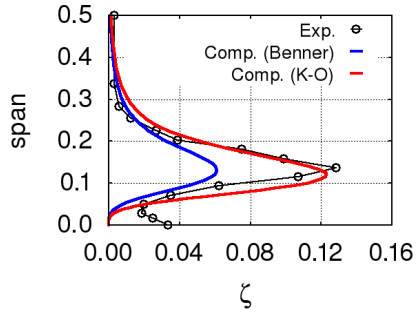

(b) *Loss coefficient.*

Figure 7.2: Predicted and measured spanwise distributions for the T106 cascade with tapered endwalls.

7.2 KTH 4b Turbine Stage

The 4b test turbine is an open-cycle test facility which was investigated by Dahlqvist and Fridh at KTH Royal Institute of Technology [18]. The rig operates at cold inlet conditions (30°C - 90°C), with air supplied by a 1 MWe screw compressor. The flexibility of the rig allows for testing of up to three turbine stages, with a nominal air flow of 4.7 kg/s at 4 bar_a. The maximum speed of the rig is rated to 11,500 rpm.

The stage is subsonic with low degree of reaction, typical of a high-pressure steam turbine stage. The blades are mounted radially on the stator and rotor disc. A cross section of the stage is shown in Figure 7.3. Between the stator platform and the rotor disc, a cavity that ejects purge flow into the main stream is located about midway between the stator trailing edge and the rotor leading edge at the hub. The rotor is shrouded and the main geometrical shroud characteristics are resumed in Table 7.2 [42]. The geometrical parameters of the vane and blade at midspan are summarized in Table 7.3.

Table 7.2: Rotor shrouding geometrical parameters of the KTH Test Turbine.

Number of labyrinth combs	4
Radial clearance in the seal [mm]	0.2
Average labyrinth radius [mm]	208
Labyrinth pitch [mm]	8.0
Comb height [mm]	5.0
Inclination angle of the forward comb wall [deg]	90
Inclination angle of the rear comb wall [deg]	90

Table 7.3: Geometrical parameters of stator and rotor of the KTH Test Turbine.

	Vane	Rotor
Number of blades	42	58
Axial chord [mm]	24.15	24.85
Stagger angle [deg]	46.0	22.1
Aspect ratio [mm]	0.764	1.284

Experimental results are available for planes 1, 2 and 3. The stage design pressure ratio of 1.23 static-to-static was investigated. A series of operating

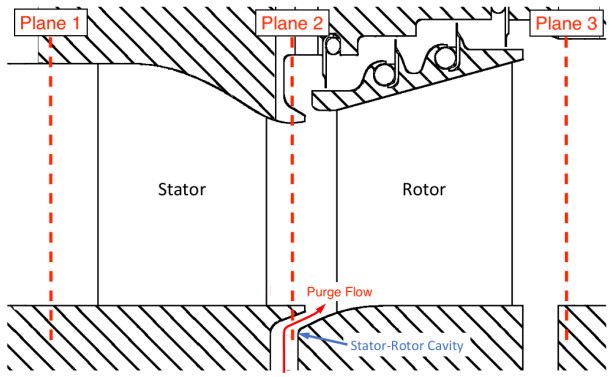

Figure 7.3: Meridional view of the KTH 4b stage with purge cavity.

speeds were analysed, characterized the non-dimensional isentropic velocity ratio:

$$\nu = \frac{\Omega r_{mean}}{\sqrt{2\Delta h_{is}}},$$

spanning from 0.30 to 0.75, at a fixed Reynolds number equal to $0.545 \cdot 10^6$. The design speed of the stage is 4452 rpm, corresponding to an isentropic velocity ratio equal to 0.48, which is close to an investigated value ($\nu = 0.43$). The investigated operating points are summarized in Table 7.4, including rotational speed and pressure-based degree of reaction Λ_p.

Table 7.4: Investigated operating points for the KTH Test Turbine.

$\nu_{tot-stat}$	$N(rpm)$	Λ_p
0.30	2810	0.023
0.43	4010	0.125
0.55	5130	0.192
0.65	6070	0.224
0.75	7010	0.262

For the speed ν 0.43, 0.55 and 0.65 the impact of the purge flow was explored. At each of these three points, two levels of purge were applied consecutively in addition to the unpurged reference case. The relation between

the mainstream, $\dot{m}_m$, and the coolant, $\dot{m}_c$, mass flow rate is expressed as:

$$\frac{\dot{m}_c}{\dot{m}_m} = \frac{q}{1-q}.$$

The investigated point are summarized in Table 7.5.

Table 7.5: Key parameters of purge flow for the KTH Test Turbine.

$\nu_{tot-stat}$	$q[\%]$	$m_p[kg/s]$
0.43	1.0	0.0176
0.43	2.0	0.0356
0.55	1.1	0.0188
0.55	2.0	0.0344
0.65	1.0	0.0168
0.65	2.1	0.0356

7.2.1 Computational domain

The geometrical parameters were extracted from the blade-to-blade stator and rotor profiles shown in Figure 7.4. To this end, it has been developed a geometric approach to reverse engineering of profiles for axial turbines, which is described in Appendix C.

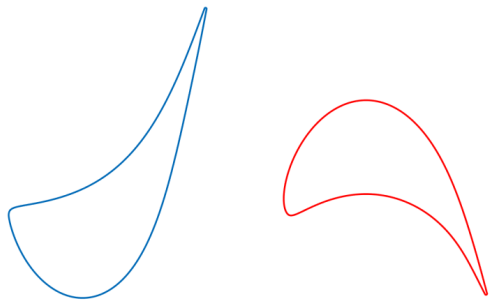

Figure 7.4: KTH test turbine stator and rotor geometries.

For the current investigation, coordinates of the outer and inner walls are extracted from [42]. The coordinate system origin was set at the turbine rotation axis and aligned with the stator vane leading edge.

The meridional mesh and the blockage factor distribution are generated with an in-house code. In the streamwise direction, the computational domain was discretized into 64 cells for each blade row, and about 48 cells for the inter-blade flow-paths. A number of 72 cells were used in the spanwise direction. The total grid size, which has been established on the base of a previous grid dependence analysis, amounts to approximately 18,000 elements. The blockage factor extracted from the airfoil geometries is shown in Figure 7.5.

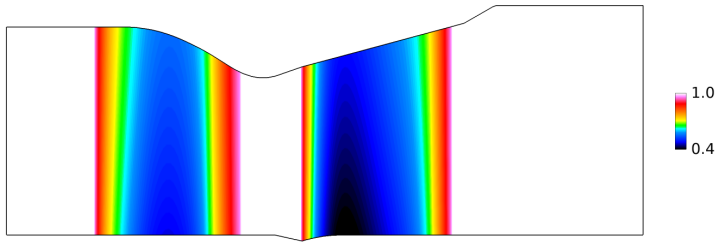

Figure 7.5: Blockage distribution of the KTH stage.

7.2.2 Discussion of results

The inlet temperature and pressure profiles were assumed to have constant values over the spanwise direction, as $T_{01} = 302.63$ K and $P_{01} = 1.2303$ *bar*. The correlations adopted for the calculations reported here are shown in Table 7.6. Three-dimensional flow features are handled as described in Chapter 3, without any specific calibration of the models constants.

Table 7.6: Correlations used in the KTH Test Turbine.

Profile & Secondary losses	Kacker-Okapuu
Deviation	Kacker-Okapuu
Incidence loss	Benner

The small expansion ratio results in quite low absolute velocity at the stage inlet and outlet, especially at reduced rotational speed and flow rate. The peak Mach number is about 0.4 at the stator exit. The adoption of the AUSM$^+$-up scheme results in good convergence rates when the cut-off Mach number is set to 0.08. Slow convergence was instead observed with the central scheme at low rotational speeds.

The first flow configuration that will be discussed in details is the one corresponding to an isentropic velocity ratio equal to $\nu = 0.43$, which corresponds to the nominal operating point of the stage. The results that will be first reported are obtained in the unpurged case. The comparison between computed and measured spanwise distributions are reported in Figure 7.6 in terms of flow angles and Mach number in planes 2 and 3. The strong flow distortions, that are in line with the low aspect ratio of the blades, makes this turbine stage a very interesting test case to assess the secondary flow features models implemented in the throughflow method. To this end, the results of three different computations are reported: one with secondary flow and shroud models (red lines), one with secondary flow model, but without the shroud (green line), and one without any 3D model (blue line). The much faithful reproduction of the experimental shape of radial distributions, which is obtained when all the 3D flow features are taken into account, is clearly evidenced for all the considered flow properties.

A non negligible discrepancy between throughflow results and measurements can be observed at the stator exit (Figures 7.6a, 7.6b), for both the flow angle and Mach number distributions, in the first 20% of the span. In this region measurements show a relevant velocity defect and strong deviation which results in a sensibly reduced flow turning. The throughflow analysis does not capture such a flow structure in that region. It must be noticed how plane 2 is located very close to the slot of the purge cavity. The presence of the slot could easily result in boundary layer thickening at the hub endwall or even flow separation and such a flow behaviour cannot be reproduced by the throughflow calculations.

At the rotor exit (Figures 7.6c, 7.6d) the agreement between predictions with 3D flow feature modelling and experimental data is good both in terms of absolute Mach number and relative flow angle. The main discrepancies are found in the first 20% of the blade span near the hub where the secondary flow penetration depth in the spanwise direction appears to be underestimated in the numerical results. It can be appreciated how the proposed shroud model noticeably improve the throughflow predictions in the tip region of the rotor blade. The effects of the shroud treatment result in a very good reproduction of the Mach number peak in this region (Figure 7.6d). Although the predicted trend is correct, the effect on the relative flow angle distribution is not so pronounced (Figure 7.6c) and the agreement with measurements is worst. The strong decrease in flow turning experienced by the experimental

distribution in the last 10% of the span could be due to the interaction of the leakage flow with the casing boundary layer, that results in a sensible dissipation of the swirl component of the velocity.

In terms of radial distributions of flow variables, a comparable level of agreement between predictions and experimental data is achieved in the whole range of tested rotational speed values. As an example, the spanwise distributions of flow angles and absolute Mach numbers are reported for the lowest ($\nu = 0.30$, Figure 7.7) and the highest ($\nu = 0.75$, Figure 7.8) isentropic velocity ratios. The change in operating speed is accompanied by a spanwise flow redistribution as observed especially in the rotor outlet plane (Figures 7.7c, 7.7d, 7.8c, 7.8d). Such a spanwise redistribution is well captured by the throughflow procedure. The most relevant discrepancies are detected in the rotor outlet relative flow angle at the lowest rotational speed ($\nu = 0.30$), where the experimental distribution shows very large variations along the span.

In terms of stage parameters the comparison between measured and predicted values is synthesized in Figures 7.9a and 7.9b, that respectively report mass flow rate and stage isentropic efficiency as a function of the isentropic velocity ratio. The experimental efficiency values were reported as scaled with the peak one. Such a peak corresponds to an isentropic velocity ratio of $\nu = 0.55$ in both experiments and calculations (Figure 7.9b). Discrepancies appear near the lower and upper limits of the investigated range of operating speed. The largest one corresponds to the highest value of the rotational speed. In this condition, the increased stage reaction and pressure difference between rotor inlet and outlet result in the prediction of high leakage losses from the shroud.

The stage mass flow rate appears to be slightly underestimated at low isentropic velocity ratios (Figure 7.9a). This is not surprising as also the most relevant discrepancies in the spanwise distributions are observed for such flow conditions.

Experimental data for the KTH stage were made available also for purged cases. In particular, measured relative flow angle and absolute Mach number radial distributions were reported at the rotor outlet (plane 3). This was regarded as a good chance to check for the capability of the proposed coolant injection model to provide a realistic impact on throughflow predictions. An example of comparison between computed and measured spanwise distributions for the unpurged and purged case with $q = 2.0\%$ is reported in

Figure 7.10 for an isentropic velocity ratio of $\nu = 0.43$. The effect of the purge flow on the radial distributions of relative flow angle (Figure 7.10a) and absolute Mach number (Figure 7.10b) at rotor outlet appears to be reasonably reproduced by the calculations. The throughflow results show the same trend of the experiments with comparable differences between the unpurged and purged cases. In particular, the local flow acceleration in the first 20% of the span in the purged case, is well evidenced by the Mach number distribution, even if it is overestimated and located at a higher span fraction in the numerical results.

A picture of the computed flowfield in the purged case can be appreciated in Figure 7.11 which reports absolute Mach number contours over-imposed on entropy contours. The effects of the wall slot injection in the rotor Mach number field is well evidenced together with the major entropy rise contributions coming from the coolant and shroud leakage flow mixing with the mainstream.

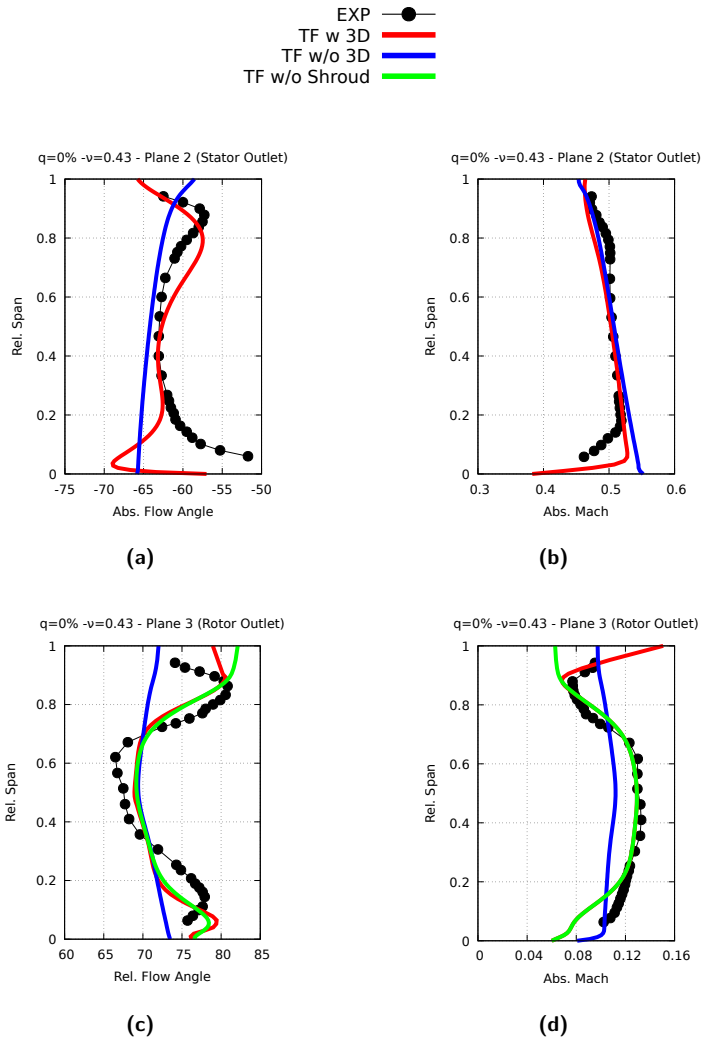

Figure 7.6: Spanwise distributions for the KTH stage for $\nu = 0.43$, $q = 0\%$

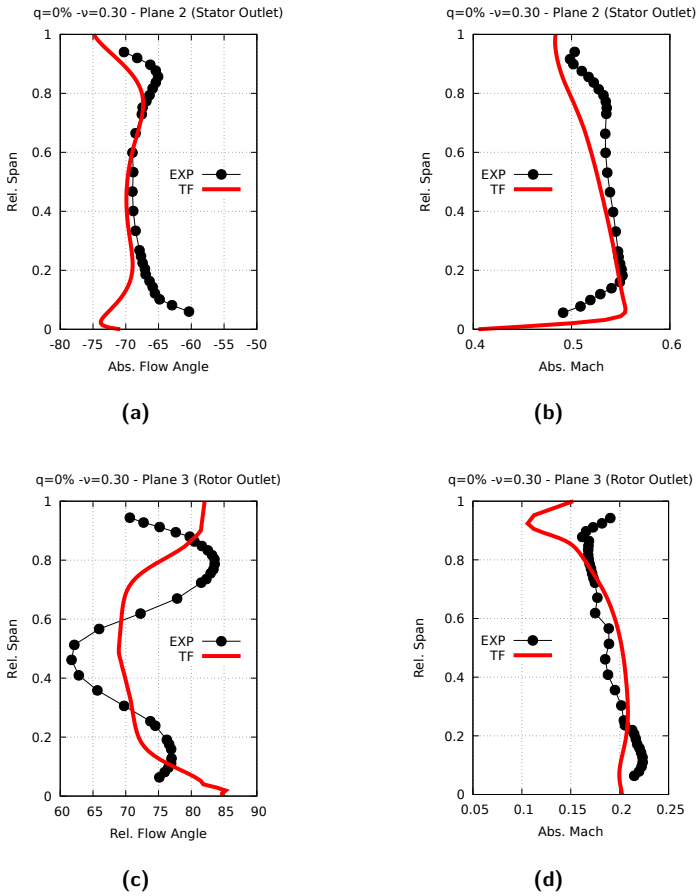

Figure 7.7: Spanwise distributions for the KTH stage for $\nu = 0.30$, $q = 0\%$

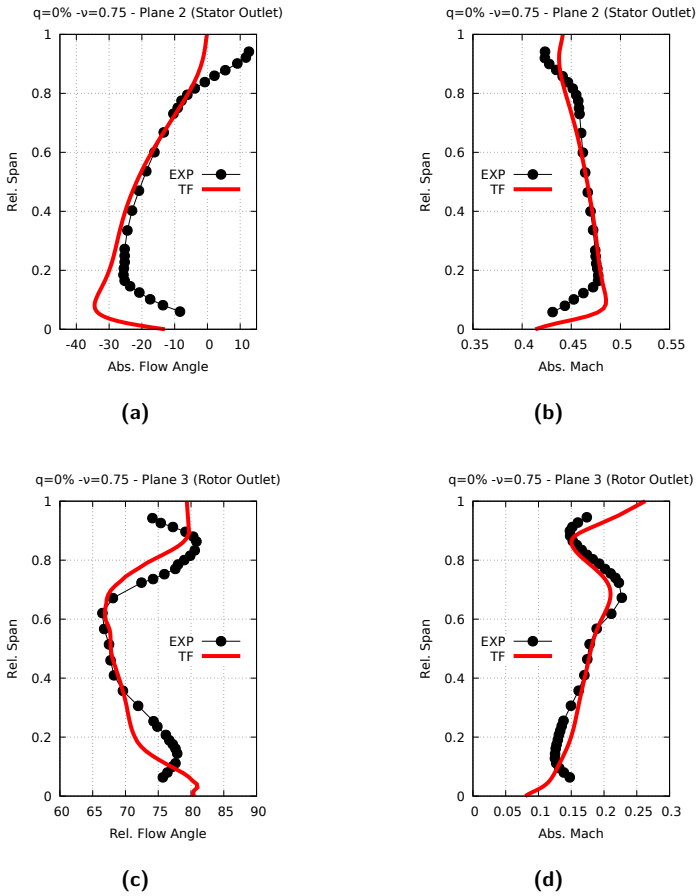

Figure 7.8: Spanwise distributions for the KTH stage for $\nu = 0.75$, $q = 0\%$

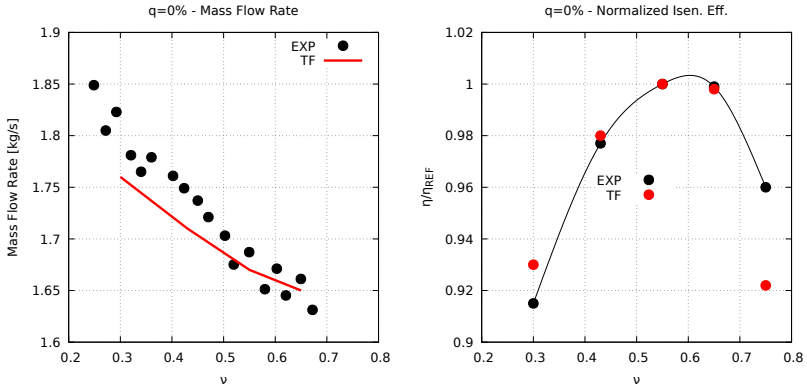

Figure 7.9: Mass flow rate (a) and isentropic efficiency (b) for the KTH stage as a function of the isentropic velocity ratio ν for $q = 0\%$

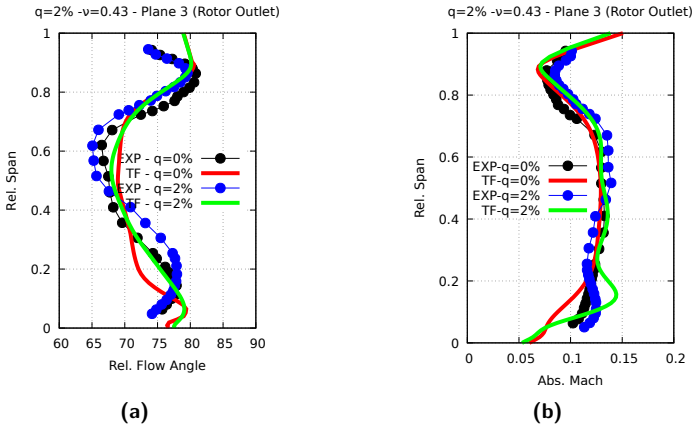

Figure 7.10: Spanwise distributions at rotor outlet for $\nu = 0.43$, $q = 2\%$

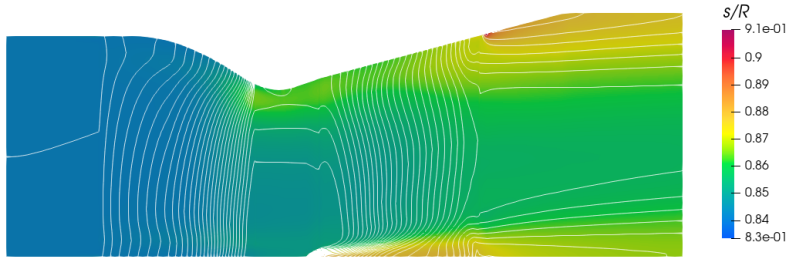

Figure 7.11: Compute Absolute Mach number contours overimposed on entropy contours for the KTH stage.

7.3 CT3 Turbine Stage

The experiments of the transonic CT3 turbine stage were performed at the *von Kármán Institute* in the framework of the TATEF 2 (Turbine Aero-Thermal External Flows 2) European project. This facility, built in the 1990s by Sieverding and Arts [60], is able to simulate the aerodynamic performance of high-pressure turbines, reproducing the operating conditions encountered in modern aeroengine.

The turbine stage is composed of cylindrical vanes and unshrouded leaned blades [20]. The main geometrical characteristics are listed in Table 7.7. A meridional view of the stage is reported in Figure 7.12. Experimental results are available for planes 1 and 3.

Table 7.7: Geometrical parameters at mid-span of stator and rotor in the CT3 Test Turbine.

	Vane	Rotor
Number of blades	43	64
Axial chord [mm]	41.16	39.78
Stagger angle [deg]	54.0	32.0
Aspect ratio [mm]	0.812	0.738

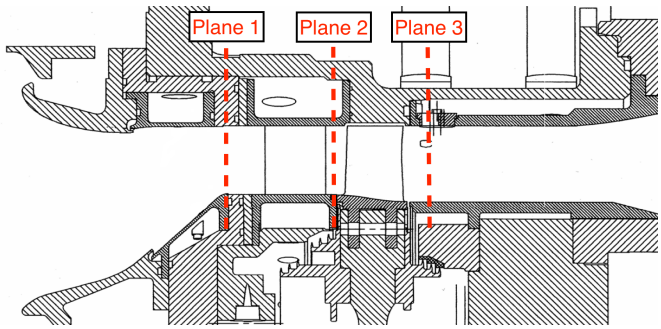

Figure 7.12: Meridional view of the CT3 stage.

Three operating conditions (*Nominal*, *Low* and *High*) were investigated during the measurement campaign at a fixed Reynolds number. Their isentropic Mach number at stator and rotor exit, and stage total pressure ratio are presented in Table 7.8. The nozzle guide vane exit Mach number is

supersonic for all the conditions. Tests were performed around the nominal speed of 6500 rpm.

Table 7.8: Operating conditions at midspan for the CT3 stage.

	$M_{2,is}$	$M_{3,is}$	p_{03}/p_{01}
Low	1.071	0.65	2.19
Nom	1.242	0.97	3.19
High	1.249	1.18	3.85

7.3.1 Computational domain

In the streamwise direction, the computational domain was discretized into 62 cells for each blade row, and about 46 cells for the inter-blade flow-paths. A number of 68 cells were used in the spanwise direction. The total grid size amounts to approximately 18,000 elements. A cell clustering was applied near leading edge and trailing edge in order to better represent the rapid variation of the blockage factor in those region, as reported in Figure 7.13.

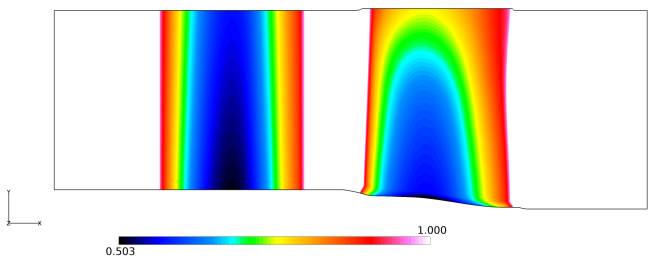

Figure 7.13: Blockage distribution of the CT3 stage.

7.3.2 Discussion of results

The spanwise distributions of total temperature, total pressure and flow angle at Plane 1 were used as inlet boundary conditions for all tests ($P_{01} = 1.65$ *bar*, $T_{01} = 434$ K, $M_1 = 0.14$). The boundary-layer displacement thickness, δ^*, which is also derived from the measured distributions, is set equal to

5% of the span at the hub, while equal to 2% of the span at the tip. At the exit of the rotor blade, the static pressure is assigned at the hub: the spanwise distribution is then determined by the radial equilibrium equation. The correlations used are reported in Table 7.9.

Table 7.9: Correlations used in the CT3 Test Turbine.

Profile & Secondary losses	Kacker & Okapuu
Deviation	Ainley & Mathieson
Incidence losses	Benner & Sjolander
Tip clearence losses	Denton
Radial Mixing	Lewis

In terms of radial distributions of flow quantities, throughflow results at the design condition are compared with experimental data and 3D, steady, viscous, CFD calculations obtained with the TRAF code [29] (Figure 7.14). None of the simulations reproduces accurately the experimental spanwise distributions of all the flow quantities, but the level of agreement of the throughflow results with measured data is comparable with that of 3D CFD results, or even better for some quantities (i.e. absolute flow angle, Figure 7.14a, and total temperature, Figure 7.14c). Indeed, the radial mixing model does a good job in improving the throughflow predictions near the endwalls but sensible discrepancies remain in the total pressure (Figure 7.14b) and absolute Mach number (Figure 7.14d) profiles: the strong distortions seen in experimental distributions and TRAF results in these regions are not captured.

The same considerations can be repeated also for off-design conditions. The throughflow results for the *Low* and *High* conditions are compared to experiments and 3D CFD results in Figures 7.15 and 7.16, respectively. The overall good reproduction of the radial distributions of flow quantities observed for the nominal condition is conserved in the prediction of off-design operations of the turbine stage. Indeed, for the considered transonic, low aspect ratio configuration, the radial distributions of flow quantities undergo relevant changes when varying the stage expansion ratio.

So, the scenario described by Figures 7.14, 7.15, 7.16 shows a remarkably accurate and reliable response of the proposed methodology to the changes in the tangentially averaged flow structure associated to different operating conditions for the stage.

The computed mass flow rate value is equal to $9.31 kg/s$ for all the three investigated operating conditions due to chocked flow in the vanes, and it is about 2% higher than the experimental value of $9.15 kg/s$. In terms of performance the comparison between computed and measured values is summarized in Figure 7.17. The calculated expansion ratio (Figure 7.17a) and power (Figure 7.17b) values are overestimated of about $2 - 3\%$ with respect to the experimental results and 3D CFD results. This is not surprising due the comparable overestimation in mass flow rate.

It is possible to observe how the performance estimates from 3D CFD are closer to the experimental data than the throughflow ones. The appreciable discrepancies in the spanwise total pressure distributions of Figure 7.14b are suspected to be responsible for the slight mismatch in the performance figures calculated by the throughflow approach.

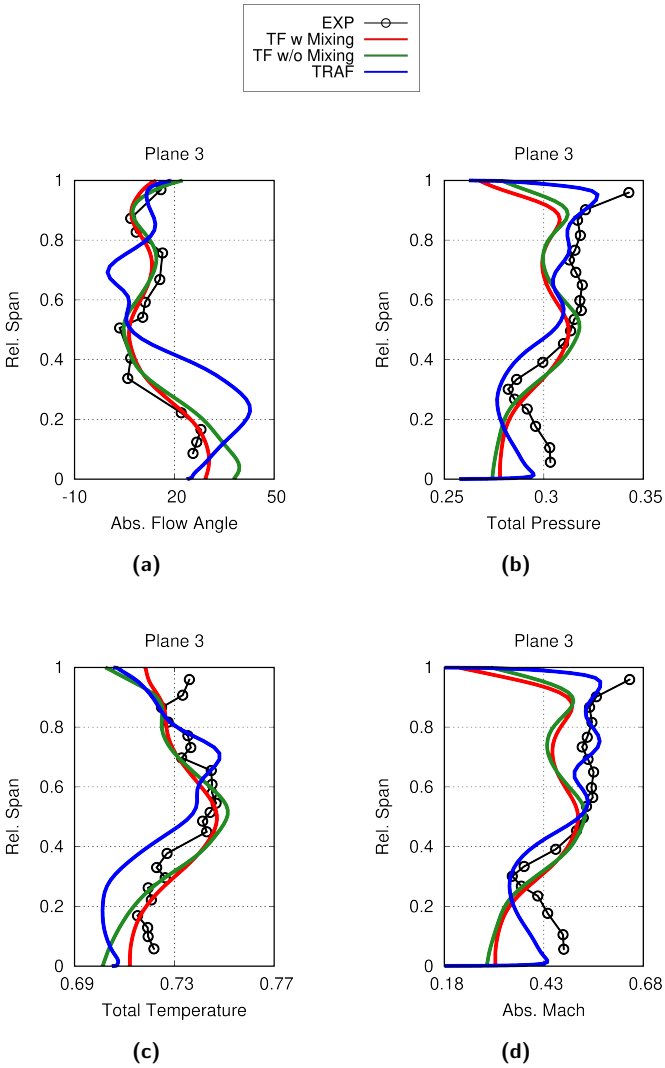

Figure 7.14: Predicted and measured spanwise distributions of flow quantities in Plan 3 for the CT3 turbine stage at nominal conditions with and without radial mixing effects.

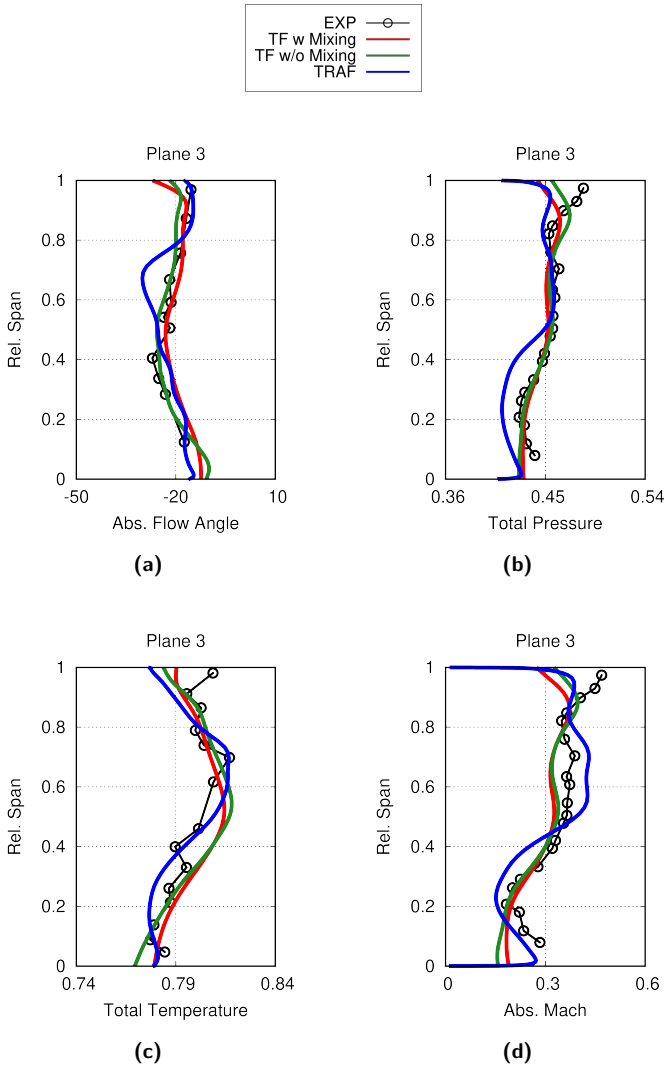

Figure 7.15: Predicted and measured spanwise distributions of flow quantities in Plan 3 for the CT3 turbine stage at low conditions with and without radial mixing effects.

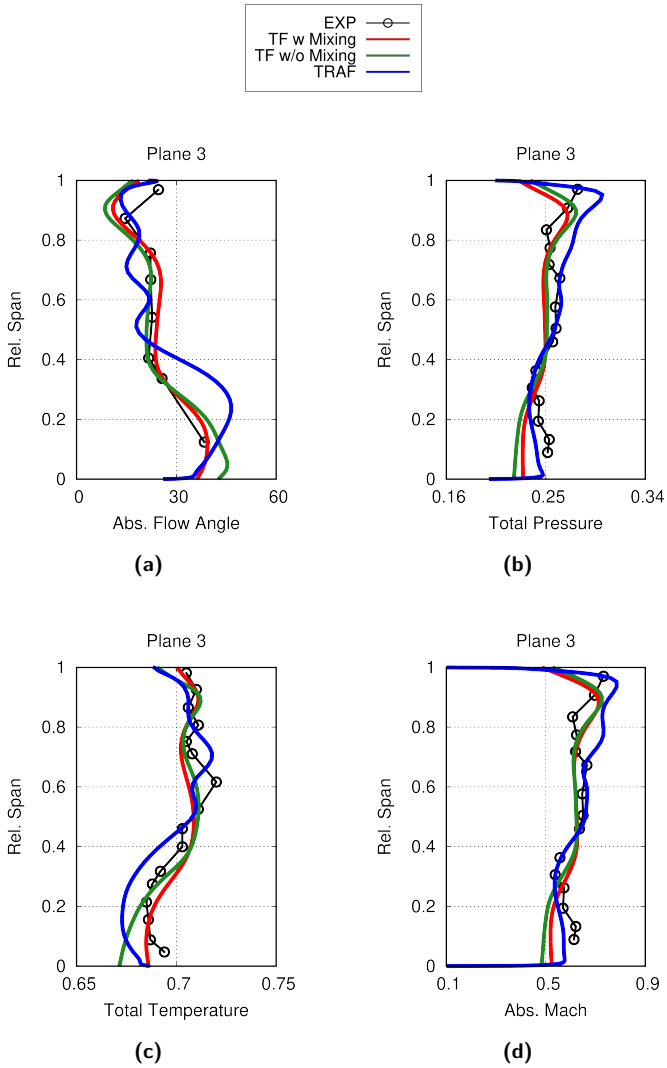

Figure 7.16: Predicted and measured spanwise distributions of flow quantities in Plan 3 for the CT3 turbine stage at high conditions with and without radial mixing effects.

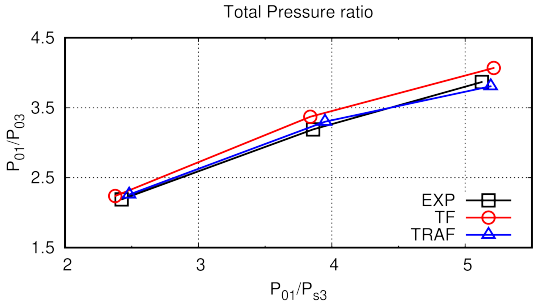

(a)

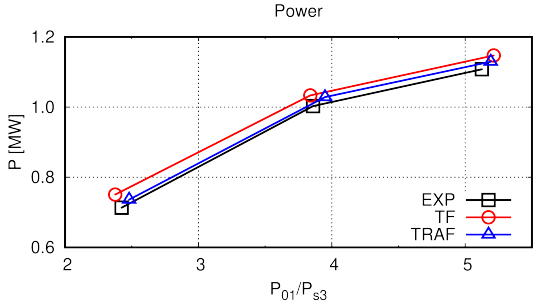

(b)

Figure 7.17: Measured and computed performance for the CT3 stage: (a) Total Pressure ratio; (b) Power.

Chapter 8

Application

The capability of the procedure is assessed by analysing some industrial axial turbine configurations designed and manufactured by Ansaldo Energia. The first one is a four-stage, medium size F-class, air-cooled gas turbine, for which design and off-design conditions are studied. The last two test cases are the low-pressure modules of two large steam turbines. Throughflow predictions in terms of main performance figures and radial distributions of flow quantities are compare with experimental data and 3D CFD steady viscous analyses (TRAF code [6]).

For the throughflow calculations carried out in the present work, the computational time was of the order of few minutes on an Intel® $i7-4770$ CPU @3.40 GHz.

8.1 Four Stage High-Pressure Gas Turbine: the 94.3A4

This section describes the application of the throughflow code to the analysis of an industrial, medium size F-class, air-cooled gas turbine designed and manufactured by Ansaldo Energia. The turbine features a state-of-the-art design with 4-stages and unshrouded rotor blades. In the present work, computations were performed at design and off-design conditions.

Throughflow analyses have been carried out by discretizing the turbine meridional flowpath with about 55,000 mesh cells. Approximately 60 cells were used for each blade row, with 48-56 cells in interblade spacing. A number

of 56 cells were used in the spanwise direction. The correlations used are reported in Table 8.1.

Table 8.1: Correlations used in the 94.3A4 Gas Turbine.

Profile & Secondary losses	Kacker-Okapuu
Incidence loss	Benner & Sjolander
Deviation	Kacker-Okapuu
Radial Mixing	Lewis

The first part of the present study is dedicated to a detailed investigation of the performance and operating characteristics of the gas turbine at base-load conditions. The second part is intended to asses the proposed procedure for off-design predictions, when the discharge pressure and the rotational speeds varies.

8.1.1 Base Load condition

The TRAF calculation at nominal condition has been matched by using the procedure described in Chapter 6. A detailed comparison between the throughflow and the 3D CFD analysis is reported below.

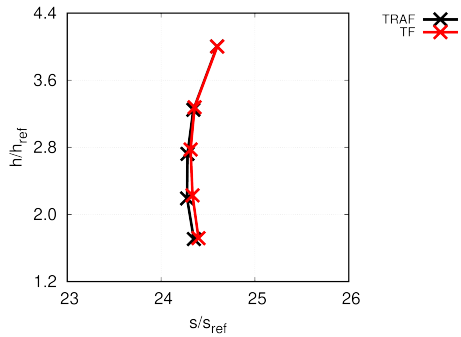

Figure 8.1: Calculated expansion lines for the 4-stage turbine in the $h-s$ diagram.

The h-s diagram of the whole turbine is shown in Figure 8.1. Starting from the same inlet conditions, the flow expansion proceeds, stage by stage, is very similar in the two analyses. In the first two stages, the process is strongly influenced by relevant injection of cooling air. The total entropy

change is slightly underestimated by the throughflow analysis with respect to 3D CFD results. This is expected to result in a slight overestimation of the turbine efficiency. In fact this circumstance is confirmed by the comparison in terms of overall operating parameters. The relative differences between throughflow and 3D CFD predictions, expressed as percentages of the TRAF results:

$$E_{\%} = \frac{x_{cfd} - x_{tf}}{x_{cfd}} 100$$

are summarized in Table 8.2. The throughflow method predicts all the relevant performance figure of the turbine with a difference below 1% with respect to state-of-the-art 3D CFD analysis.

Table 8.2: Relative differences between computed operating characteristics for the 94.3A4 Gas Turbine at design conditions.

Parameter	Difference (%)
Mass flow rate	+0.020
Power	−0.015
Total-to-total efficiency	+0.013

A comparison between throughflow and 3D CFD solutions in terms of absolute Mach number contours in the meridional plane is shown in Figure 8.2. The predicted flow patterns appear very similar, with practically the same Mach number levels in all the stages.

Figure 8.3 shows radial distributions of flow quantities at the exit of rotating blade rows: absolute flow angle, total pressure, total temperature and absolute Mach number. Although not perfect, the agreement between throughflow and TRAF predictions is actually very good. The most relevant differences occur for the first stage (Figures 8.3a, 8.3e, 8.3i, 8.3m), which is characterized by a low aspect ratio and by the injection of a high coolant mass flow rate. For most of the stages, in the first 20% of the span the throughflow results show a relevant defect in the spanwise distributions of Mach number and total pressure (Figures 8.3f, 8.3g and 8.3m, 8.3n, 8.3o, 8.3p) which is not detected by the TRAF calculation. Such a defect is related to the accumulation effect of the strong purge flows from the stator-rotor cavities. The discrepancies between the two calculations in the aforementioned region of the flowpath suggest that the diffusion level of coolant flow properties in the main flow tend to be somewhat underestimated by the radial mixing

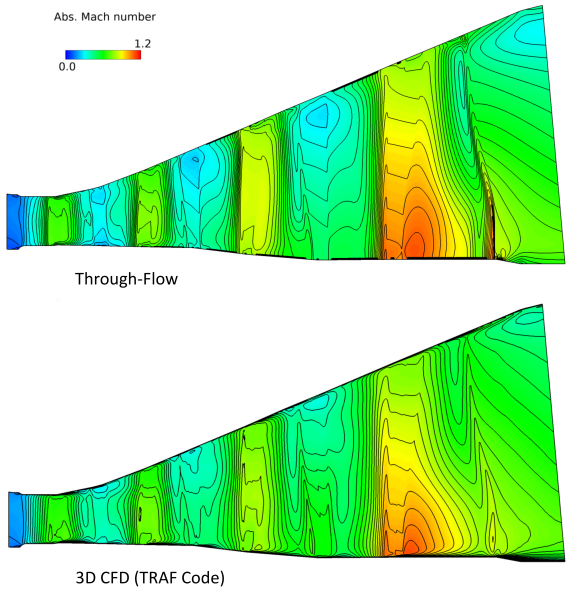

Figure 8.2: Computed Absolute Mach number contours for the AE94.3A4 gas turbine: Design condition.

model implemented in the throughflow procedure. However, the tip leakage effects appears to be satisfactorily reproduced in the distributions of all the considered flow quantities.

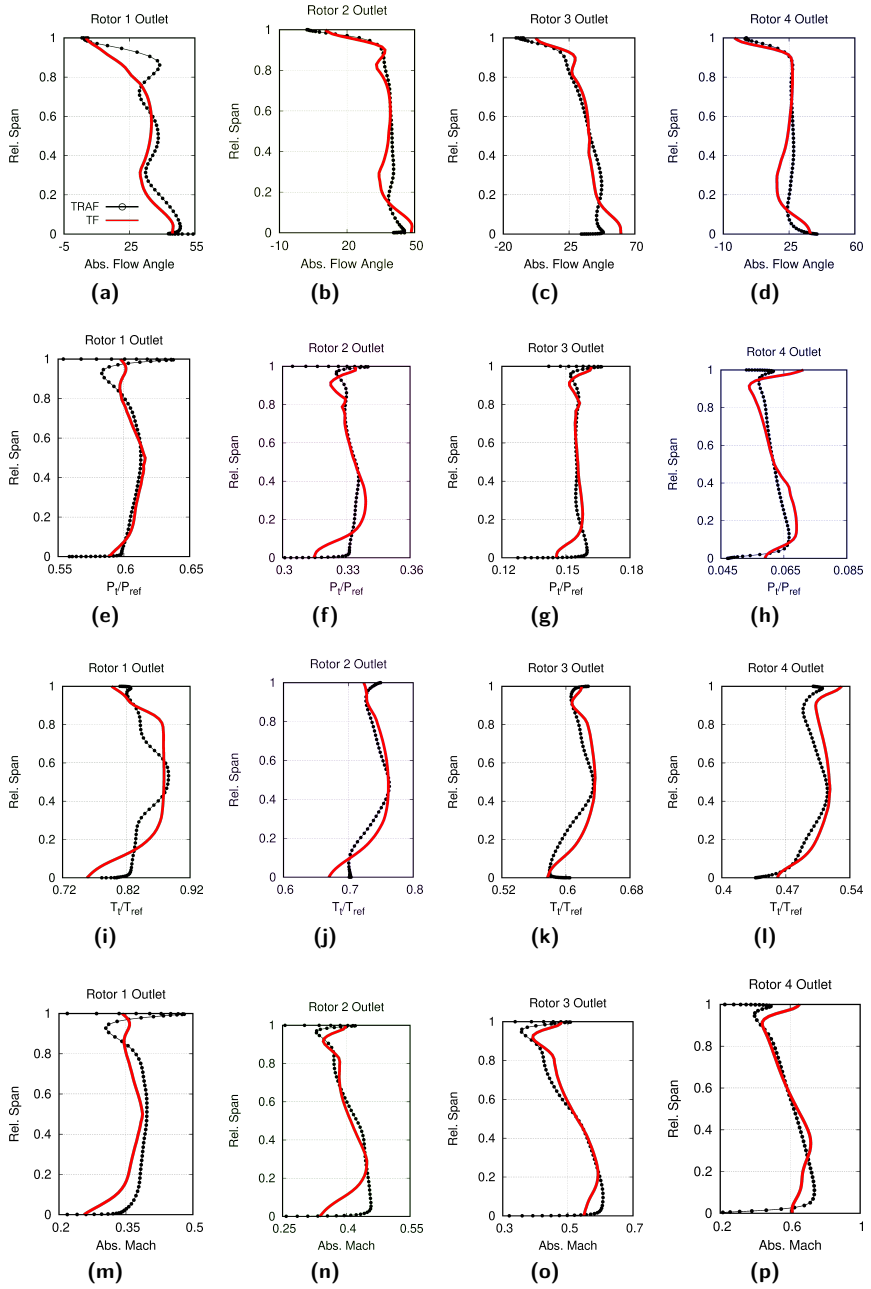

Figure 8.3: Throughflow and 3D CFD (TRAF) spanwise distributions of flow quantities at the exit of rotor blade rows for the AE94.3A4 axial turbine at nominal condition.

8.1.2 Off-design analyisis

Twelve operating conditions are analysed at a fixed Reynolds number and turbine inlet boundary conditions (total temperature, total pressure and absolute flow angle). The discharge pressure of the gas turbine was varied in a wide range: up to 30% lower and 100% higher than that in the design case. The detailed assessment of the throughflow code is discussed referring to turbine performances, compared to the ones computed with the TRAF code.

Figures 8.4, 8.5 shows the evolution of the total pressure ratio, the power, the efficiency, and the mass flow rate, as a function of the ratio between the inlet total pressure and the static pressure:

$$\pi_s = \frac{p_{0,inlet}}{p_{s,outlet}}.$$

All values are non-dimensionalized with respect to the design conditions. The agreement between throughflow and the 3D CFD results can be considered good. The major discrepancies at reduced expansion ratios, at all the considered operating speeds, where the throughflow calculations predicts lower efficiency values. The drop in the calculated efficiency (Figure 8.5b) occurs at operating points that are extremely far from typical operations of the turbine and in such conditions the accuracy of correlations for predicting losses becomes certainly questionable. Anyway, the highlighted discrepancies can be considered in line with the predictive capability that one can expect from a meridional analysis.

As it can be deduced from the behaviour of the mass flow rate, Figure 8.5a, the turbine stays chocked in the whole range of analysed expansion ratios. This is due to the strong coolant injection upstream of the first stage nozzle throat, and this feature is also well reproduced by the throughflow calculations.

The detailed assessment of the throughflow model for the 100% higher and 30% lower pressure than that in the design case conditions is now discussed. Figures 8.6, 8.7 and 8.8 report, respectively, the flow field in the meridional plane and the spanwise distribution of the main flow quantities, in comparison with the ones obtained with the fully 3D CFD code.

The computed flowfields appear to be very similar also in strong off-design conditions. As evident from the Mach number contours of Figure 8.7, at the lowest expansion ratio, the last stage rotor operates beyond limit loading conditions. As a result of this, a supersonic flow region that extends from the

hub endwall up to about 70% of the span is formed immediately downstream the fourth stage. Such a circumstance determines the formation of a three-dimensional shock system which can be clearly observed in Figure 8.7. The throughflow analysis also predicts the formation of a supersonic flow region at the last stage exit, even if it reports a smaller spanwise extension for such a feature and a slightly different shock system. The shock waves in the throughflow analysis appear to be the strongest ones as a higher Mach number is observed upstream of them with respect to the 3D CFD calculation. Such discrepancy is not surprising as the shock trace in the meridional flowfield from the TRAF solution is the result of the circumferential averaging of the complex fish-tail shock configuration that arises at the rotor trailing edge. The shock waves predicted in the throughflow solution are obviously axisymmetric ones and such a shock configuration is a very rare occurrence in turbomachinery flows. Despite such a difference in the computed shock structures, shock capturing capabilities represent a very desirable feature in meridional analyses, as they offer an approximate but realistic way to introduce supersonic flow losses in throughflow analyses, without the need of a dedicated correlation.

The radial profiles reported in Figure 8.8 summarize the comparison between throughflow and TRAF results at off-design operations, in terms of absolute flow angle, total pressure, total temperature and absolute Mach number. The agreement is again satisfactory and comparable to the one achieved at the design point.

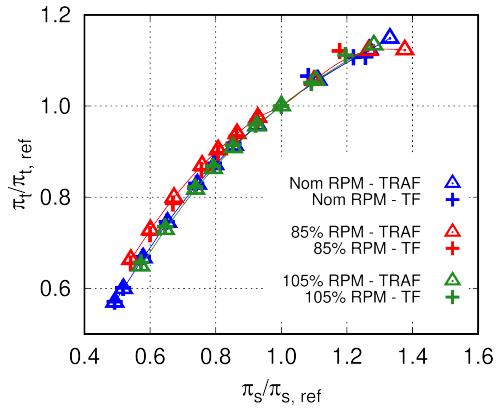

(a)

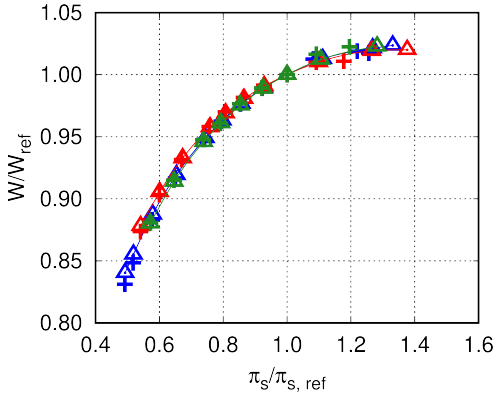

(b)

Figure 8.4: Computed performance for the axial turbine at off-design conditions: total pressure ratio (a) and power (b) in function of the pressure ratio.

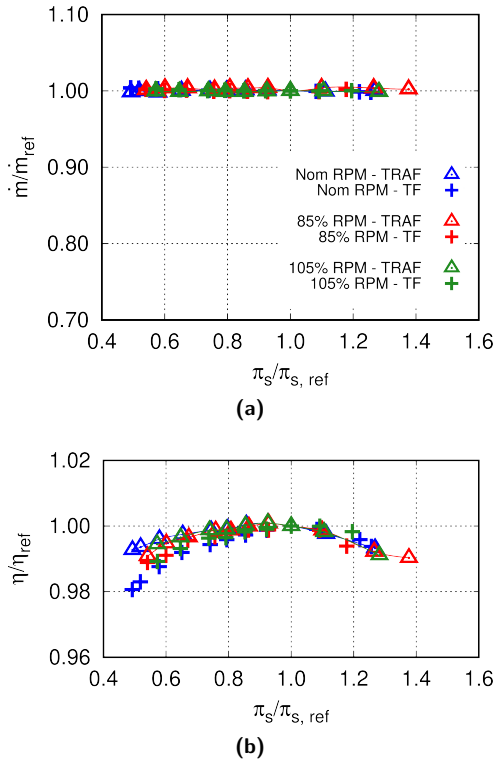

Figure 8.5: Computed performance for the axial turbine at off-design conditions: mass-flow (a) and efficiency (b) in function of the pressure ratio.

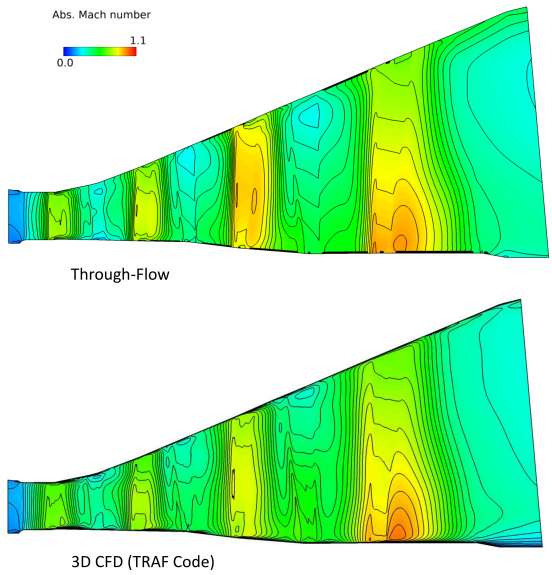

Figure 8.6: Computed Absolute Mach number contours for the AE94.3A4 gas turbine: High condition.

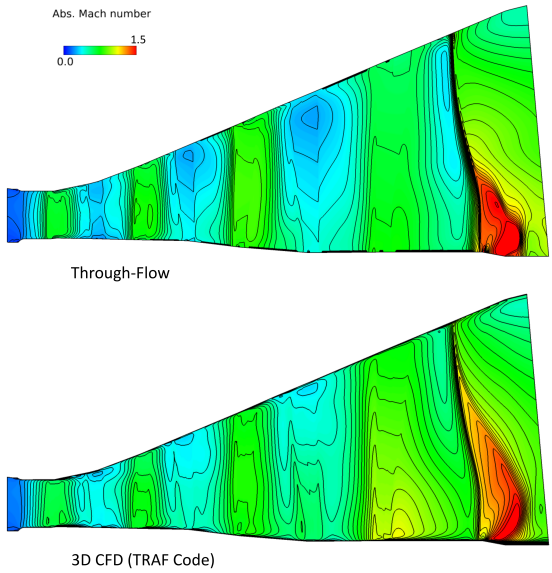

Figure 8.7: Computed Absolute Mach number contours for the AE94.3A4 gas turbine: Low condition.

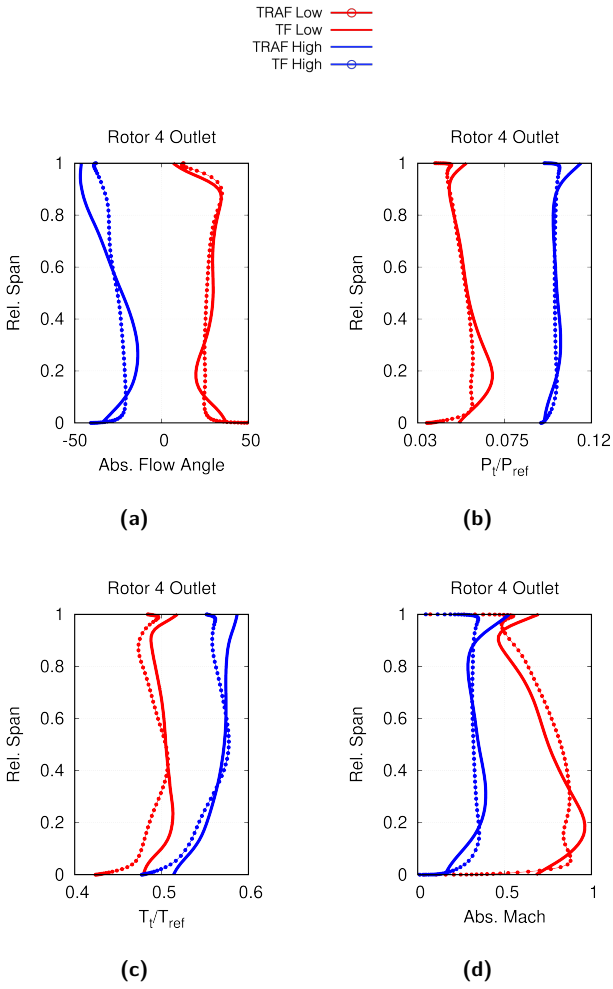

Figure 8.8: Throughflow and 3D CFD (TRAF) spanwise distributions of flow quantities at the exit of the last rotor blade row at low and high conditions.

8.2 Three Stage Low-Pressure Steam Turbine: the ND48

The second analysed configuration corresponds to the three-stage low pressure module of the ND48 steam turbine. It features a modern design for the $100 \div 250$ MW output power range with the last rotor blade which heights up 48 in. Such a component recently underwent a wide design and optimization campaign during a joint development project between Ansaldo Energia and Škoda Energy [69]. A picture of this blade is reported in Figure 8.9. The snubber that was installed for structural reasons is visible at about mid-span. All the rotor blades are shrouded.

Figure 8.9: Last rotor blade of the ND48 Low-Pressure Module [69].

The meridional grid employed for throughflow calculations has 853 cells in the streamwise direction and 89 in the spanwise one, with 64 mesh cells for each bladed portion of the flowpath. The correlations are reported in Table 8.3. It is important to precise that for the deviation angle it was used the Ainley-Mathieson correlation [4], integrated with the Traupel formulation for supersonic flows. The cross section of the snubber was approximated with an ellipse and a unity drag coefficient was considered on the base of a snubber Reynolds number of the order of 10^4.

8.2.1 Discussion of results

A comparison between the absolute Mach number contours in the meridional plane obtained from throughflow and 3D CFD solutions is presented in Figure 8.10. In order to be consistent with the throughflow model, the three-dimensional CFD TRAF solution was tangentially area-averaged to ob-

Table 8.3: Correlations used in the ND48 Steam Turbine.

Profile & Secondary losses	Craig & Cox
Deviation	Ainley & Mathieson, Traupel
Leakage loss	Denton
Radial Mixing	Lewis

tain the flow visualization of Figure 8.10. The predicted flow patterns appear very similar, with practically the same Mach number levels in all the three stages. A visible difference concerns the reproduced effect of the snubber, which results in a wider and more pronounced wake in the TRAF solution. The body force field that models such effects brings about the generation of turbulent stresses in the 3D CFD solution, while it only generates flow distortions and entropy in the throughflow analysis.

The expansion line of the 3-stage module is reported in the *h-s* diagram in Figure 8.11. Starting from the same inlet conditions, the turbine expansion process is very similar in the two analyses. The enthalpy drop for last stage is slightly underestimated by the throughflow analysis with respect to 3D CFD results.

This observation is consistent with the comparison between the computed performance summarized in Table 8.4. Here the difference between predicted operating parameters, expressed as percentage of the TRAF results, are reported. The difference in the predicted mass flow rate values is negligible, but the throughflow analysis underestimates the output power. Total-to-total adiabatic efficiencies is instead overestimated in the throughflow results. The discrepancies are however not dramatic and in line with the use of classical loss correlations for such a modern and challenging turbine architecture.

Table 8.4: Relative differences between computed operating characteristics for the ND48 Low-Pressure module.

Parameter	Difference (%)
Mass flow rate	-0.2
Power	-1.2
Total-to-total efficiency	+0.4

A more detailed assessment of the throughflow predictions is carried out

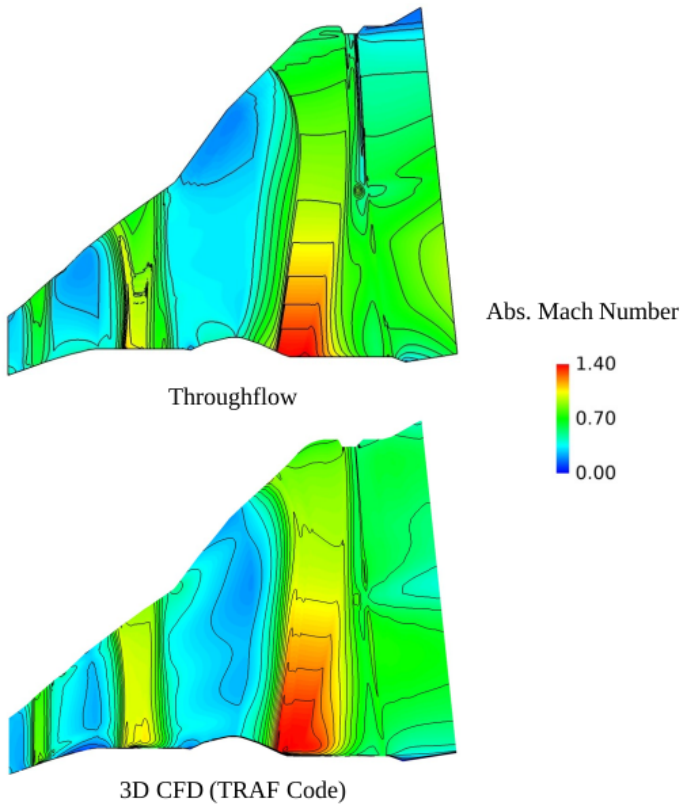

Figure 8.10: Computed Absolute Mach number contours for the ND48 Low-Pressure module.

in Figure 8.12, which reports radial distributions of flow quantities, such as total temperature and total pressure, and the absolute and Mach number at the last two rotors trailing edges. The last two stages exhibit the higher Mach number levels and, for the sake of conciseness, the discussion is limited to the results for them. The throughflow results are in satisfactory agreement with 3D CFD predictions and consistent with the observed differences in operating conditions. The most pronounced discrepancies concern total pressure distributions in the first 50% of the blade span at the exit of both the considered stages (Figures 8.12d and 8.12h). The absolute Mach number

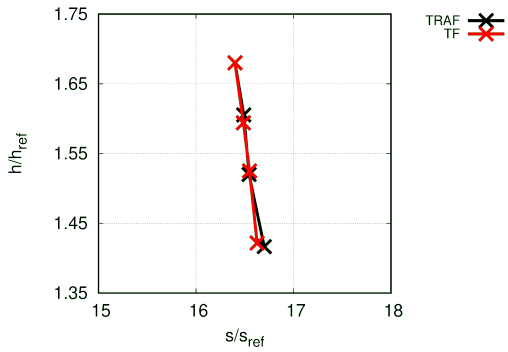

Figure 8.11: Expansion line for the ND48 Low-Pressure module.

distribution at the outlet of the fourth stage (Figure 8.12f) highlights the already noticed difference in the predicted effect of the part-span snubber. In fact, it results in a marginal velocity defect in the throughflow Mach number distribution at the third rotor exit, in contrast to the stronger one detected in the 3D CFD profile. However, the spanwise flow distortions captured by the throughflow analysis show a realistic behaviour thanks to the proposed 3D flow features modelling. In particular, the predicted impact of the shroud-cavity flow reinjection appears very similar in throughflow and CFD predictions. This circumstance is made particularly evident by the total temperature peak near the casing at the second stage outlet (Figure 8.12c), but it is also appreciable in absolute flow angle distributions (Figures 8.12a and 8.12e).

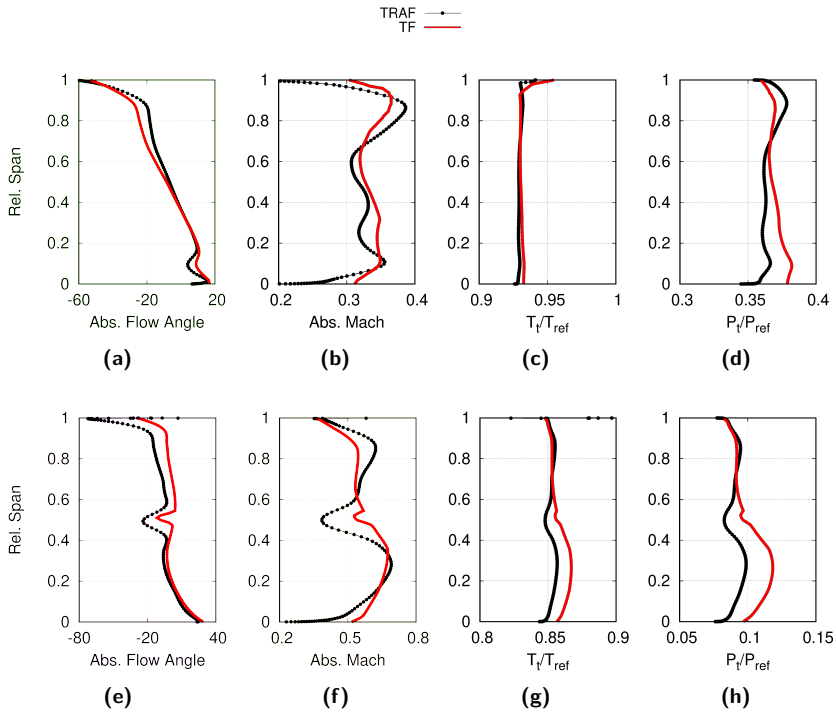

Figure 8.12: Spanwise distributions of flow quantities for the ND48 Low-Pressure module at Stage 3 Outlet.

8.3 Four Stage Low-Pressure Steam Turbine: the ENEL 320

The last test case comprises the last four stages of the double flow, low pressure cylinder of the Ansaldo 320 MW steam turbine installed in the ENEL Power Station of Vado Ligure (Italy). The main design parameters of the turbine are listed in Table 8.5 (Accornero et al. [2], Accornero and Maretto [1]). The last stage features are characterized by a pressure ratio of over 6:1, and a hub to tip radius of about 2. The high blade speed results in very high relative Mach numbers (about 2) at last stage stator root and rotor tip. Damping wires are present on the third and fourth rotor blades. Only the last rotor blade is unshrouded.

Throughflow analyses have been carried out with a number of elements similar to the previous cases. In particular, with about 68,500 mesh cells, of which 845 cells in the streamwise direction and 81 in the spanwise one.

Table 8.5: ENEL 320 turbine design characteristics.

Power	320 MW
Rotating speed	3000 RPM
LP inlet temperature	365 °C
LP inlet pressure	9.5 bar
Condenser pressure	0.05 bar

8.3.1 Discussion of results

Bladed and non-bladed regions of this 4-stage module were discretized with the same number of cells used for the ND48 turbine. The comparison between computed flowfields in the meridional plane is again carried out in terms of absolute Mach number contours (Figure 8.13). The Mach number is predicted to be subsonic in the first stage while it goes above the unity starting from the second stage and reaches very high values (up to 2) at the exit of the last stage and close to the casing. In the throughflow results, the extension and the peak Mach number of the supersonic region close to the tip endwall at the last stage outlet are very similar to the ones predicted by the TRAF code. The supersonic flow in that region results in a shock-wave

approximately normal to the wall, which is captured by both the throughflow and 3D CFD solution, although with different intensities. The lower velocity detected in the 3D CFD solution downstream of the shock qualifies it as the strongest one between the two. As previously observed, the shock-systems on the circumferentially averaged meridional flowfield cannot be accurately reproduced by the throughflow approach, however the highlighted differences can considered of negligible practical importance.

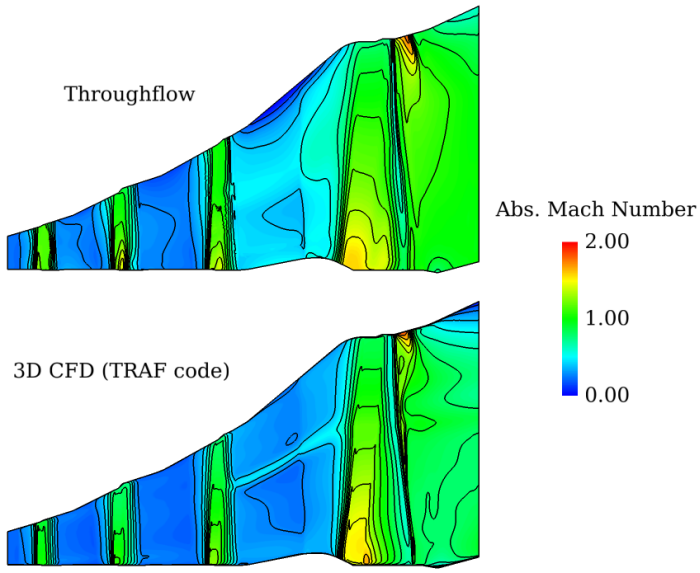

Figure 8.13: Absolute Mach Number Contours for the Enel 320MW Low-Pressure module.

To give an idea of the accuracy achieved with present throughflow analysis, predicted spanwise distributions at the turbine exit are compared with 3D CFD results and available experimental data in Figure 8.14. Measurements concern the absolute and relative flow angles and the relative Mach number (Figures 8.14a, 8.14b, 8.14d). It can be appreciated how the agreement between throughflow results and measured distributions is comparable to that obtained from the TRAF solution. Again, it must be noticed how the proposed tip clearance treatment allows a realistic reproduction of the flow

behaviour in the meridional analysis close to the casing. Also in this case, the effect of the damping wires appear attenuated in the throughflow results with respect to 3D CFD predictions, but this does not seem to upset the comparison with experimental data.

In terms of integral operating parameters, the relative differences between throughflow and 3D CFD predictions, expressed as percentages of the TRAF results, are summarized in Table 8.6. The slight overestimation of the mass flow rate by the throughflow calculation results in a comparable overestimation of the output power relative to the same operating characteristic from the 3D CFD analysis. The total-to-total efficiency is only marginally lower. Such a comparison appears in line with the results obtained for the ND48 turbine and confirms the feasibility of the proposed throughflow procedure for design and analysis applications in the field of steam turbines.

Table 8.6: Relative differences between computed operating characteristics for the ENEL 320 Low-Pressure module.

Parameter	Difference (%)
Mass flow rate	+0.3
Power	+0.8
Total-to-total efficiency	+0.2

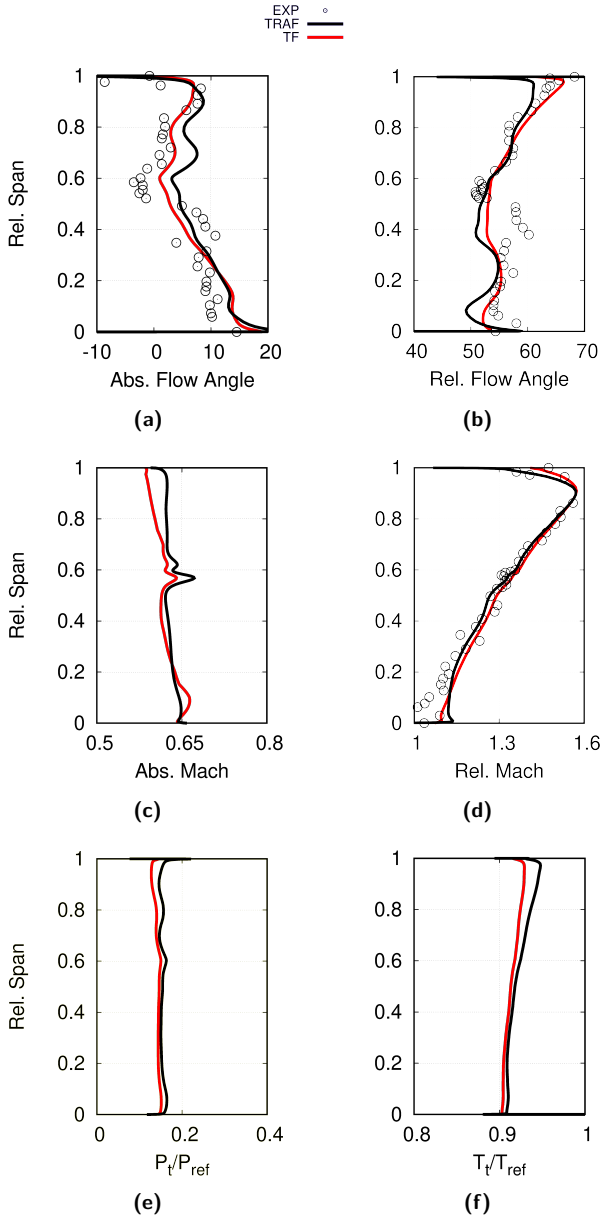

Figure 8.14: Spanwise distributions of flow quantities at last stage exit for the Enel 320 Low-Pressure module.

Chapter 9

Conclusions

The research activity described in this work was dedicated to the extension and improvement of a CFD-based throughflow code for the purpose of developing of a meridional analysis tool that fulfils the requirements of modern industrial design systems for turbomachinery. The code solves the axisymmetric Euler equations for ideal and real gases, with tangential blockage and body forces, and inherits its numerical scheme from the TRAF code, i.e. the 3D, steady/unsteady Navier-Stokes solver which, since almost 30 years, has being developed by the Prof. Arnone's group at the University of Florence. The numerical flux treatment has been enhanced by the introduction of a novel scheme which is an adaption of the AUSM$^+$-up scheme for treating real gas flows and handle body force terms in a comprehensive and consistent framework. The scheme has proven to be fast, robust and reliable in a variety of flow configurations that range from almost incompressible to definitely supersonic, and from ideal gas to superheated and saturated steam. The adoption of an implicit treatment of source terms contributes to maintain good stability properties from the numerical framework in the cases in which those terms are dominant.

Several models aimed at introducing three-dimensional flow features (like secondary flows, and leakage flows for shrouded and unshrouded blades) in the meridional analyses have been developed and implemented. The proposed methodology tried to address the issue with simple phenomenological models that naturally fit into the CFD based structure of the throughflow solver. Correlations are introduced to estimate losses, but they also offer an effective way to distribute those losses in the meridional flowpath in a physically sound

manner. A radial mixing model has also been developed and implemented in order to allow the radial migration of the endwall flow and predict realistic radial profiles of flow properties in multistage turbines. The treatment of secondary flows as transverse velocity fields generated by Lamb-Oseen-type vortices plus a realistic spanwise entropy distribution has proven to result in good secondary deviation and loss predictions on a linear cascade based on the T106 profile. The proposed leakage models, based on source/sink convective flux terms, used in conjunction with fairly standard correlations for profile losses and deviations has led to improved predictions in the both the KTH 4b subsonic stage and the CT3 transonic stage. For such configurations, thanks to the 3D models, the calculated radial distributions of flow properties and stage performance were found to be in fairly acceptable agreement with CFD results and experiments, not only at design conditions, but also when studying off design trends.

A coolant injection model, still based on source term vectors, has been also developed. It allowed us to apply the source terms in prescribed regions of the flowfield, thus enabling the simulation of the complex cooling schemes typical of modern multistage gas turbines. For the case of cavity purge flows, a comparison with CFD predictions of a wall jet in crossflow showed how the injection treatment, in conjunction with the radial mixing model, is able to provide total pressure and temperature profiles that closely resembles the one obtained with a viscous 3D CFD calculation. Moreover, the validation of the proposed methodology against the measurements carried out on the KTH 4b stage showed how such an approach is able to reproduce the impact that purging has on spanwise distributions of flow quantities.

The application of the proposed method to three industrial multistage turbine configuration designed and manufactured by Ansaldo Energia, confirmed the good quality of the throughflow results, which have been scrutinized against 3D CFD analyses carried out with the TRAF code and the available experimental data. Three-dimensional flow features, coolant injections, and radial mixing models resulted to be mandatory for a realistic reproduction of spanwise distributions. Also integral performance figures were predicted in good agreement with 3D CFD results. The comparison with the available experimental data supports the idea of the reliability given by the throughflow results.

The feasibility of the discussed off-design analysis procedure, based on an automated matching procedure with 3D CFD calculations at design,

has been demonstrated by the application to a modern, four-stage, heavy-duty gas turbine. We showed how a very good agreement with steady, three-dimensional CFD predictions, is obtained in terms of both spanwise distributions and performance figures of the turbine. Such a goal can be achieved with the proposed approach, at a very reduced cost in terms of computational time and resources: in comparison with the TRAF code, the CPU-time ratio for the calculation of each operating point is about 20, even in the case of a massively parallel execution of the CFD solver.

The capability of the procedure to deal with supersonic flows has been made clear by the results of the analysis of the heavy-duty gas turbine and the ENEL 320 low pressure steam turbine as well. The shock-wave patterns reproduced by the meridional analysis are in agreement with the ones shown by the circumferentially averaged 3D CFD solution. This clearly shows the superiority of CFD-based approaches equipped with state-of-the-art flux schemes, with respect to classical methods that do not possess such shock capturing capabilities.

We believe that the generality and reliability characteristics shown by the proposed throughflow method demonstrate its feasibility for an intensive use in the field of multistage steam and gas turbines design.

Appendix A

Semi-implicit operator matrices

The implicit operator makes up a large, sparse, and non-symmetric block matrix with dimensions equal to the total number of cells. The solution of the linear equation system (2.6) requires the inversion of the implicit operator. In terms of primitive variables the state vector and the source vectors are given by:

$$V = \begin{bmatrix} \rho \\ u \\ v \\ w \\ p \end{bmatrix}, \quad S = \begin{bmatrix} \rho v \\ \rho uv \\ \rho v^2 - \rho w^2 \\ 2\rho vw \\ \rho vE + pv \end{bmatrix}, \quad S_f = \begin{bmatrix} 0 \\ F_{bx} \\ F_{by} \\ F_{b\theta} \\ F_{b\theta}\Omega r \end{bmatrix}$$

and the final left hand side matrix is expressed as:

$$\left[I - \frac{\delta t}{\mathcal{V}} P \right]$$

with P defined as:

$$\begin{bmatrix} 1+v & 0 & \rho & 0 & 0 \\ uv - b_{21} & 1+\rho v - b_{22} & \rho u - b_{23} & 0 & 0 \\ v^2 - w^2 - b_{31} & -b_{32} & 1 + 2\rho v - b_{33} & -2\rho w & 0 \\ 2vw - b_{41} & -b_{42} & 2\rho w - b_{43} & 1 + 2\rho v & 0 \\ \frac{v}{2}c^2 - b_{51} & \rho uv - b_{52} & \left(\frac{\gamma}{\gamma-1}p + \frac{3}{2}\rho v^2\right) - b_{53} & \rho vw & 1 + \frac{\gamma}{\gamma-1}v \end{bmatrix}$$

The coefficients scheme b_{ij} are given by:

$$
\begin{aligned}
b_{21} &= F_{bx} & b_{22} &= a_1 a_3 \tan\alpha & b_{23} &= a_2 a_3 \\
b_{31} &= F_{by} & b_{32} &= a_1 a_4 \tan\alpha & b_{33} &= a_2 a_4 \\
b_{41} &= F_{b\theta} & b_{42} &= \frac{a_1}{r n_\theta} \sin\alpha & b_{43} &= a_2 \frac{n_{\theta l}}{r n_\theta} \\
b_{51} &= F_{b\theta} c_t & b_{52} &= \frac{a_1 c_t}{r n_\theta} \sin\alpha & b_{53} &= a_2 c_t \frac{n_{\theta l}}{r n_\theta}
\end{aligned}
$$

where c_t is the tangencial velocity component and:

$$
\begin{aligned}
F_{bx} &= b\frac{n_{xl}}{r n_\theta} & n_{xl} &= -\sin\alpha\cos\beta \\
F_{by} &= b\frac{n_{yl}}{r n_\theta} & n_{yl} &= -\sin\alpha\sin\beta \\
F_{b\theta} &= b\frac{n_{\theta l}}{r n_\theta} & n_{\theta l} &= \cos\alpha
\end{aligned}
$$

with b the blockage factor and:

$$
\begin{aligned}
\frac{\partial q}{\partial x} &= \frac{\partial\left(\Omega r^2 + \sqrt{u^2+v^2}\; r\tan\alpha\right)}{\partial x} \\
\frac{\partial q}{\partial r} &= \frac{\partial\left(\Omega r^2 + \sqrt{u^2+v^2}\; r\tan\alpha\right)}{\partial r}
\end{aligned}
$$

The coefficients a_i are:

$$
\begin{aligned}
a_1 &= \frac{uv}{c} \\
a_3 &= \frac{n_{xl}}{r n_\theta} - \frac{n_{\theta l}}{r n_\theta}\tan\lambda\sin\beta^* \\
a_2 &= 2c_t + \frac{u^2+2v^2}{c}\tan\alpha \\
a_4 &= \frac{n_{yl}}{r n_\theta} + \frac{n_{\theta l}}{r n_\theta}\tan\lambda\cos\beta^*
\end{aligned}
$$

The blade-to-blade angle, α, the meridional angle, β, and the lean angle, λ, are computed from the S2 flow surface.

Appendix B

Solution of the flow surface and blockage evolution equations

The common formulation for the flow surface and blockage evolution equations can be written as:

$$\frac{\partial Q}{\partial t} + u\frac{\partial Q}{\partial x} + v\frac{\partial Q}{\partial r} = S, \tag{B.1}$$

or in a curvilinear (ξ, η) coordinate system, as:

$$\frac{\partial Q}{\partial t} + \frac{u}{J}\frac{\partial Q}{\partial \xi}\xi_x + \frac{u}{J}\frac{\partial Q}{\partial \eta}\eta_x + \frac{v}{J}\frac{\partial Q}{\partial \xi}\xi_r + \frac{v}{J}\frac{\partial Q}{\partial \eta}\eta_r = S \tag{B.2}$$

The contravariant velocities in the ξ, η coordinate directions are given by:

$$U = u\xi_x + v\xi_r$$
$$V = u\eta_x + v\eta_r$$

The equation (B.2) can be now written as:

$$\frac{\partial Q}{\partial t} + \frac{U}{J}\frac{\partial Q}{\partial \xi} + \frac{V}{J}\frac{\partial Q}{\partial \eta} = S, \tag{B.3}$$

By adopting an implicit second-order central finite-difference discretization of equation (B.3):

$$\frac{\partial Q}{\partial t} = \frac{Q_{i,j}^{(n+1)} - Q_{i,j}^{(n)}}{\delta t}$$
$$\frac{\partial Q}{\partial \xi} = \frac{Q_{i+1,j}^{(n+1)} - Q_{i-1,j}^{(n+1)}}{2}$$
$$\frac{\partial Q}{\partial \eta} = \frac{Q_{i,j+1}^{(n+1)} - Q_{i,j-1}^{(n+1)}}{2}$$

we obtain:

$$\frac{Q_{i,j}^{(n+1)} - Q_{i,j}^{(n)}}{\delta t} + \frac{U}{2J}\left(Q_{i+1,j}^{(n+1)} - Q_{i-1,j}^{(n+1)}\right) + \frac{V}{2J}\left(Q_{i,j+1}^{(n+1)} - Q_{i,j-1}^{(n+1)}\right) = S$$

By introducing central difference operators as:

$$Q_{i+1,j}^{(n+1)} - Q_{i-1,j}^{(n+1)} = \delta_\xi Q_{i,j}^{(n+1)}$$

$$Q_{i,j+1}^{(n+1)} - Q_{i,j-1}^{(n+1)} = \delta_\eta Q_{i,j}^{(n+1)}.$$

With this, we have:

$$\frac{Q_{i,j}^{(n+1)}}{\delta t} + \frac{U}{2J}\delta_\xi Q_{i,j}^{(n+1)} + \frac{V}{2J}\delta_\eta Q_{i,j}^{(n+1)} = S + \frac{Q_{i,j}^{(n)}}{\delta t}.$$

If we gather together $Q_{i,j}^{(n+1)}$,

$$\left(\frac{1}{\delta t} + \frac{U}{2J}\delta_\xi + \frac{V}{2J}\delta_\eta\right) Q_{i,j}^{(n+1)} = S + \frac{Q_{i,j}^{(n)}}{\delta t},$$

and multiply for δt,

$$\left(1 + \frac{U}{2J}\delta t\delta_\xi + \frac{V}{2J}\delta t\delta_\eta\right) Q_{i,j}^{(n+1)} = S\delta t + Q_{i,j}^{(n)},$$

knowing that $Q_{i,j}^{(n+1)} = Q_{i,j}^{(n)} + \delta Q$, we can write:

$$\left(1 + \frac{U}{2J}\delta t\delta_\xi + \frac{V}{2J}\delta t\delta_\eta\right) \delta Q = S\delta t - \left(\frac{U}{2J}\delta t\delta_\xi + \frac{V}{2J}\delta t\delta_\eta\right) Q_{i,j}^{(n)}. \qquad \text{(B.4)}$$

Now, defining the right-hand side as the residual:

$$R^{(n)} = S\delta t - \left(\frac{U}{2J}\delta_\xi + \frac{V}{2J}\delta_\eta\right) Q_{i,j}^{(n)}$$

it is possible to re-write equation (B.4) as:

$$\left(1 + \frac{U}{2J}\delta t\delta_\xi + \frac{V}{2J}\delta t\delta_\eta\right)\delta Q = R^{(n)}.$$

Approximating the left-hand side implicit operator with a factorization,

$$\left(1 + \frac{U}{2J}\delta t\delta_\xi + \frac{V}{2J}\delta t\delta_\eta\right)\delta Q \approx \left(1 + \frac{U}{2J}\delta t\delta_\xi\right)\left(1 + \frac{V}{2J}\delta t\delta_\eta\right),$$

we finally obtain:

$$\left(1 + \frac{U}{2J}\delta t\delta_\xi\right)\left(1 + \frac{V}{2J}\delta t\delta_\eta\right)\delta Q = R^{(n)}. \tag{B.5}$$

This allows the decomposition of the implicit operator in two tridiagonal systems:

$$\begin{cases} \left(1 + \dfrac{U}{2J}\delta t\delta_\xi\right)\delta Q^* = R^{(n)} \\ \left(1 + \dfrac{V}{2J}\delta t\delta_\eta\right)\delta Q = \delta Q^* \end{cases}$$

Appendix C

A geometric approach to reverse engineering of profiles

The geometric parameters of a blade can be extracted through a geometrical approach to reverse engineering of profiles.

A profile can be schematized as the succession of polynomial functions and circumferences. The type of curves that make up a profile can be summarized in five mathematical functions, as shown in Figure C.1. The logical choices for three of these functions are the leading edge circle, the trailing edge circle and the circular arc describing the uncovered suction surface beyond the throat. The suction surface from the leading edge tangency point to the throat, and the entire pressure surface are both defined by polynomials.

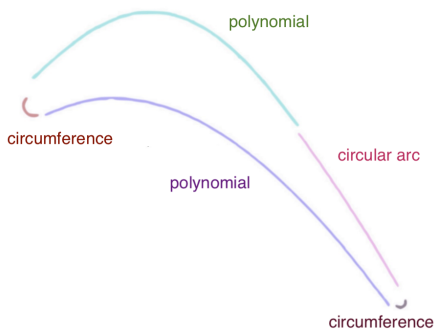

Figure C.1: Airfoil mathematical functions.

At least seven point have been identified on the blade profile: three points for each circumference and one point for the third order polynomial. For a better approximation, fourteen points were used, as shown in Figure C.2.

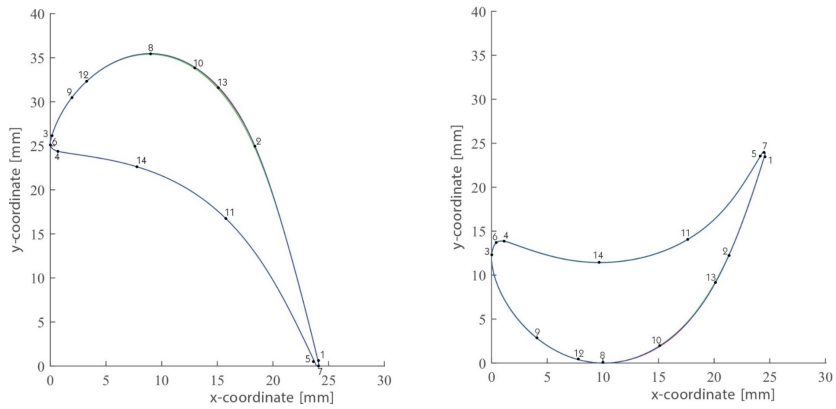

(a) *Vane.* **(b)** *Blade.*

Figure C.2: The airfoil's key points.

Once the profile has been reconstructed, the eleven independent blade parameters can be obtained [56]: radius, axial chord, tangential chord, unguided turning, inlet blade angle, inlet wedge angle, leading edge radius, exit blade angle, trailing edge radius, number of blades and throat. The section parameters computed from the model are compared with the real ones, as shown in Table C.1. It is important to note that the blades are characterized by a constant geometry.

Table C.1: Geometrical parameters obtained for the KTH Test Turbine.

	Vane	KTH Vane	Rotor	KTH Rotor
Axial chord [mm]	24.15	24.13	24.85	24.59
Unguided turning [deg]	9.4	16.9	21.7	21.6
Inlet blade angle [deg]	29.4	33.5	-55.4	58.3
Inlet wedge angle [deg]	2.7	2.4	24.0	22.6
Exit blade angle [deg]	-79.5	-74.6	69.3	70.4
Leading edge radius [mm]	2.64	2.16	2.82	2.85
Trailing edge radius [mm]	0.25	0.25	0.27	0.27
Throat [mm]	8.28	8.07	8.08	8.13
Chord [mm]	34.89	34.7	26.09	26.6
Area [mm^2]	247.9	252.4	203.4	217.9

Publications

This research activity has led to publications in international journals and conferences. These are summarized below.

1. **Ricci M.**, Pacciani R., Marconcini M., Macelloni P., Cecchi S., Bettini C. *Computational Fluid Dynamics-Based Throughflow Analysis of Transonic Flows in Steam Turbines* , *ASME Journal of Turbomachinery*, November 2019, vol. 141, iss. 11, 111005 (7 pages) [DOI: https://doi.org/10.1115/1.4044871]

2. **Ricci M.**, Pacciani R., Marconcini M., Macelloni P., Cecchi S., Bettini C. *CFD-Based Throughflow Analysis of Transonic Flows in Steam Turbines* , *ASME Turbo Expo 2019: Turbomachinery Technical Conference and Exposition*, Phoenix, Arizona, paper GT2019-90851 (10 pages) [DOI: https://doi.org/10.1115/GT2019-90851]

3. **Ricci M.**, Pacciani R., Marconcini M., Arnone A. *Secondary flow and radial mixing modelling for CFD-based Through-Flow method: an axial turbine application*, *Energy Procedia*, August 2018, vol. 148, pp. 218-225 [DOI: https://doi.org/10.1016/j.egypro.2018.08.071]

Bibliography

[1] Accornero, A. and Maretto, L. *Aerodynamics and Streamwetness Fraction of a Multi-Stage Turbine - Comparison of Prediction with Experimental Data*. Lecture Series 1983-06. Aerothermodynamics of Low Pressure Steam Turbines and Condensers. von Kármán Institute, 1983.

[2] Accornero, A. and Doria, G. and Maretto, L. and Zunino, E. *Flow in a 320 MW Low-Pressure Section: Theoretical and Experimental Evaluation*. Lecture Series 1980-06. Steam Turbines for Large Power Output. von Kármán Institute, 1980.

[3] Adkins, G. G. and Smith, L. H. "Spanwise Mixing in Axial-Flow Turbomachines". In: *J. of Engineering for Power* 104.1 (1982), pp. 97–110.

[4] Ainley, D. G and Mathieson, G. C. R. "A Method of Performance Estimation for Axial-flow Turbines". In: *Aeronautical Research Council London (UK)* ARC R/M 2974 (1951).

[5] Angot, P., Bruneau, C. H., and Fabrie, P. "A penalization method to take into account obstacles in incompressible viscous flows". In: *Numerische Mathematik* 81.4 (1999), pp. 497–520. ISSN: 0945-3245. DOI: 10.1007/s002110050401.

[6] Arnone, A. "Viscous analysis of three-dimensional rotor flow using a multigrid method". In: *Journal of Turbomachinery* 116.3 (1994), pp. 435–445.

[7] Banjac, M., Petrovic, M. V., and Wiedermann, A. "A New Loss and Deviation Model for Axial Compressor Inlet Guide Vanes". In: *Journal of Turbomachinery* 136.7 (Jan. 2014). 071011. ISSN: 0889-504X. DOI: 10.1115/1.4025956.

[8] Banjac, M., Petrovic, M. V., and Wiedermann, A. "Secondary Flows, Endwall Effects, and Stall Detection in Axial Compressor Design". In: *Journal of Turbomachinery* 137.5 (May 2015). 051004. ISSN: 0889-504X. DOI: 10.1115/1.4028648.

[9] Baralon, S., Hall, U., and Eriksson, L. E. "Viscous throughflow modelling of transonic compressors using a time-marching finite volume solver". In: *ISABE - International Symposium on Air Breathing Engines, 13 th, Chattanooga, TN*. 1997, pp. 502–510.

[10] Baturin, O. et al. "Generation of the Equations for the Profile Losses Calculation in Blade Row of Axial Turbines in Design Analysis". In: Turbo Expo: Power for Land, Sea, and Air Volume 2C: Turbomachinery (June 2016). V02CT39A013. DOI: 10.1115/GT2016-56320.

[11] Benner, M. W., Sjolander, S. A., and Moustapha, S. H. "An empirical prediction method for secondary losses in turbines - Part I: A new loss breakdown scheme and penetration depth correlation". In: *Journal of turbomachinery* 128.2 (2006), pp. 273–280.

[12] Benner, M. W., Sjolander, S. A., and Moustapha, S. H. "An empirical prediction method for secondary losses in turbines - Part II: A new secondary loss correlation". In: *Journal of Turbomachinery* 128.2 (2006), pp. 281–291.

[13] Bird, R. B. "Transport phenomena". In: *Applied Mechanics Reviews* 55.1 (2002), R1–R4.

[14] Boncinelli, P. et al. "Real Gas Effects in Turbomachinery Flows: A Computational Fluid Dynamics Model for Fast Computations ". In: *Journal of Turbomachinery* 126.2 (June 2004), pp. 268–276. ISSN: 0889-504X. DOI: 10.1115/1.1738121.

[15] Brandt, A. "Multi-level adaptive computations in fluid dynamics". In: *4th Computational Fluid Dynamics Conference*. 1979. DOI: 10.2514/6.1979-1455.

[16] Came, P. M. and Marsh, H. "Secondary Flow in Cascades: Two Simple Derivations for the Components of Vorticity". In: *Journal of Mechanical Engineering Science* 16.6 (1974), pp. 391–401. DOI: 10.1243/JMES_JOUR_1974_016_073_02.

[17] Craig, H. R. M. and Cox, H. J. A. "Performance Estimation of Axial Flow Turbines". In: *Proceedings of the Institution of Mechanical Engineers* 185.1 (1970), pp. 407–424.

[18] Dahlqvist, J. and Fridh, J. "Experimental investigation of turbine stage flow field and performance at varying cavity purge rates and operating speeds". In: *Journal of Turbomachinery* 140.3 (2018), p. 031001.

[19] De Ruyck, J. and Hirsch, C. "Investigations of an Axial Compressor End-Wall Boundary Layer Prediction Method". In: *Journal of Engineering for Power* 103.1 (Jan. 1981), pp. 20–33. ISSN: 0022-0825. DOI: 10.1115/1.3230699.

[20] Dénos, R. and Paniagua, G. "Effect of vane-rotor interaction on the unsteady flowfield downstream of a transonic high pressure turbine". In: *Proceedings of the Institution of Mechanical Engineers, Part A: Journal of Power and Energy* 219.6 (2005), pp. 431–442.

[21] Denton, J. D. "The 1993 IGTI Scholar Lecture: Loss Mechanisms in Turbomachines". In: *Journal of Turbomachinery* 115.4 (Oct. 1993), pp. 621–656. ISSN: 0889-504X. DOI: 10.1115/1.2929299.

[22] Denton, J. D. "The Use of a Distributed Body Force to Simulate Viscous Effects in 3D Flow Calculations". In: Turbo Expo: Power for Land, Sea, and Air Volume 1: Turbomachinery (June 1986). V001T01A058. DOI: 10.1115/86-GT-144.

[23] Denton, J. D. "Throughflow calculations for transonic axial flow turbines". In: *Journal of Engineering for Power* 100.2 (1978), pp. 212–218.

[24] Duden, A. and Fottner, L. "Influence of taper, Reynolds number and Mach number on the secondary flow field of a highly loaded turbine cascade". In: *Proceedings of the Institution of Mechanical Engineers, Part A: Journal of Power and Energy* 211.4 (1997), pp. 309–320.

[25] Dunham, J. and Came, P. M. "Improvements to the Ainley-Mathieson Method of Turbine Performance Prediction". In: *Journal of Engineering for Power* 92.3 (July 1970), pp. 252–256. ISSN: 0022-0825. DOI: 10.1115/1.3445349.

[26] Gallimore, S. J. "Spanwise Mixing in Multistage Axial Flow Compressors: Part II—Throughflow Calculations Including Mixing". In: *Journal of Turbomachinery* 108.1 (July 1986), pp. 10–16. ISSN: 0889-504X. DOI: 10.1115/1.3262009.

[27] Gallimore, S. J. and Cumpsty, N. A. "Spanwise Mixing in Multistage Axial Flow Compressors: Part I—Experimental Investigation". In: *J. Turbomach.* 108.1 (1986), pp. 2–9.

[28] Gehring, S. and Riess, W. "Analysis of the Mixing Process in a 1.5 Stage Turbine With Coolant Ejection". In: Turbo Expo: Power for Land, Sea, and Air Volume 1: Aircraft Engine; Marine; Turbomachinery; Microturbines and Small Turbomachinery (May 2000). V001T03A114. DOI: 10.1115/2000-GT-0669.

[29] Giovannini, M. et al. "Evaluation of unsteady computational fluid dynamics models applied to the analysis of a transonic high-pressure turbine stage". In: *Proceedings of the Institution of Mechanical Engineers, Part A: Journal of Power and Energy* (2014), p. 0957650914536170.

[30] Hartsel, J. "Prediction of Effects of Mass-Transfer Cooling on the Blade-Row Efficiency of Turbine Airfoils". In: *10th Aerospace Sciences Meeting*. 1972, p. 11. DOI: 10.2514/6.1972-11.

[31] Hawthorne, W. R. and Armstrong, W. D. "Rotational Flow Through Cascades Part II. The Circulation About The Cascade". In: *The Quarterly Journal of Mechanics and Applied Mathematics* 8.3 (Jan. 1955), pp. 280–292. ISSN: 0033-5614. DOI: 10.1093/qjmam/8.3.280.

[32] Hirsch, C. and Warzee, G. "A Finite-Element Method for Through Flow Calculations in Turbomachines". In: *Journal of Fluids Engineering* 98.3 (Sept. 1976), pp. 403–414. ISSN: 0098-2202. DOI: 10.1115/1.3448341.

[33] Jameson, A., Schmidt, W., and Turkel, E. "Numerical solutions of the Euler equations by finite volume methods using Runge-Kutta time-stepping schemes". In: *AIAA paper* 1259 (1981), p. 1981.

[34] Kacker, S. C. and Okapuu, U. "A Mean Line Prediction Method for Axial Flow Turbine Efficiency". In: *J. of Engineering for Power* 104.1 (1982), pp. 111–119.

[35] Lewis, K. L. "Spanwise Transport in Axial-Flow Turbines: Part 1—The Multistage Environment". In: *Journal of turbomachinery* 116.2 (1994), pp. 179–186.

[36] Lewis, K. L. "Spanwise Transport in Axial-Flow Turbines: Part 2—Throughflow Calculations Including Spanwise Transport". In: *Journal of turbomachinery* 116.2 (1994), pp. 187–193.

[37] Liou, M. S. "A Sequel to AUSM, Part II: AUSM$^+$-up for All Speeds". In: *Journal of Computational Physics* 214 (2006), pp. 137–170.

[38] Liou, M. S. "Ten years in the making-AUSM-family". In: *15th AIAA Computational Fluid Dynamics Conference*. 2001. Chap. 2521. DOI: 10.2514/6.2001-2521.

[39] Liou, M. S. and Edwards, J. "Numerical speed of sound and its application to schemes for all speeds". In: *14th Computational Fluid Dynamics Conference*. 1999, p. 3268.

[40] Marsh, H. *A digital computer program for the through-flow fluid mechanics in an arbitrary turbomachine using a matrix method*. Ministry of Aviation, 1966.

[41] Martinelli, L. and Jameson, A. *Validation of a multigrid method for the Reynolds averaged equations*. American Institute of Aeronautics and Astronautics, 1988.

[42] Mikaillian, N. "Test Turbine Measurements and Comparison with Meanline and Throughflow Calculations". MA thesis. Stockolm: KTH, 2012.

[43] Mildner, F. and Gallus, H. E. "An Analysis Method for Multistage Transonic Turbines With Coolant Mass Flow Addition". In: *Journal of Turbomachinery* 120.4 (Oct. 1998), pp. 744–752. ISSN: 0889-504X. DOI: 10.1115/1.2841785.

[44] Mittal, R. and Iaccarino, G. "Immersed Boundary Methods". In: *Annual Review of Fluid Mechanics* 37.1 (2005), pp. 239–261. DOI: 10.1146/annurev.fluid.37.061903.175743.

[45] Moustapha, S. H., Kacker, S. C., and Tremblay, B. "An improved incidence losses prediction method for turbine airfoils". In: *Journal of Turbomachinery* 112.2 (1990), pp. 267–276.

[46] Novak, R. A. "Streamline curvature computing procedures for fluid-flow problems". In: *Journal of Engineering for Power* 89.4 (1967), pp. 478–490.

[47] Pacciani, R., Marconcini, M., and Arnone, A. "A CFD-Based Throughflow Method with Three-Dimensional Flow Features Modelling". In: *J. Turbomach., Propulsion and Power* 2.3 (2017), p. 11.

[48] Pacciani, R., Marconcini, M., and Arnone, A. "Comparison of the AUSM+-up and other advection schemes for turbomachinery applications". In: *Shock Waves* (2019). ISSN: 1432-2153. DOI: 10.1007/s00193-018-0883-4.

[49] Pacciani, R. et al. "A CFD-Based Throughflow Method With An Adaptive Formulation For The S2 Streamsurface". In: *Proceedings of the Institution of Mechanical Engineers, Part A: Journal of Power and Energy* 230.1 (2016), pp. 16–28.

[50] Pasquale, D., Persico, G., and Rebay, S. "Optimization of Turbomachinery Flow Surfaces Applying a CFD-Based Throughflow Method". In: *Journal of Turbomachinery* 136.3 (Sept. 2013). 031013. ISSN: 0889-504X. DOI: 10.1115/1.4024694.

[51] Persico, G. and Rebay, S. "A penalty formulation for the throughflow modeling of turbomachinery". In: *Computers & Fluids* 60 (2012), pp. 86–98. ISSN: 0045-7930. DOI: 10.1016/j.compfluid.2012.03.001.

[52] Petrovic, M. V. and Riess, W. "Off-design Flow Analysis of Low-Pressure Steam Turbines". In: *Proceedings of the Institution of Mechanical Engineers, Part A: Journal of Power and Energy* 211.3 (1997), pp. 215–224. DOI: 10.1243/0957650971537123.

[53] Petrovic, M. V. and Wiedermann, A. "Through-Flow Analysis of Air-Cooled Gas Turbines". In: *Journal of Turbomachinery* 135.6 (Sept. 2013). 061019. ISSN: 0889-504X. DOI: 10.1115/1.4023463.

[54] Petrovic, M. V., Wiedermann, A., and Banjac, M. B. "Development and Validation of a New Universal Through Flow Method for Axial Compressors". In: Turbo Expo: Power for Land, Sea, and Air Volume 7: Turbomachinery, Parts A and B (June 2009), pp. 579–588. DOI: 10.1115/GT2009-59938.

[55] Petrovic, M. V. et al. "Part Load Behavior of the LP Part of an Industrial Gas Turbine". In: Turbo Expo: Power for Land, Sea, and Air Volume 2A: Turbomachinery (June 2017). V02AT40A033. DOI: 10.1115/GT2017-64778.

[56] Pritchard, L. J. "An Eleven Parameter Axial Turbine Airfoil Geometry Model". In: Turbo Expo: Power for Land, Sea, and Air Volume 1: Aircraft Engine; Marine; Turbomachinery; Microturbines and Small Turbomachinery (Mar. 1985). DOI: 10.1115/85-GT-219.

[57] Rains, D. A. "Tip Clearance Flows in Axial flow Compressors and Pumps". PhD thesis. California Institute of Technology, 1954.

[58] Rubechini, F. et al. "The Impact of Gas Modeling in the Numerical Analysis of a Multistage Gas Turbine". In: *Journal of Turbomachinery* 130.2 (Mar. 2008). 021022. ISSN: 0889-504X. DOI: 10.1115/1.2752187.

[59] Shapiro, A. *The Dynamics and Thermodynamics of Compressible Fluid Flow: Volume I*. John Wiley & Sons, 1953, pp. 219–231.

[60] Sieverding, C. H. and Arts, T. "The VKI Compression Tube Annular Cascade Facility CT3". In: Turbo Expo: Power for Land, Sea, and Air Volume 5: Manufacturing Materials and Metallurgy; Ceramics; Structures and Dynamics; Controls, Diagnostics and Instrumentation; Education (June 1992). V005T16A001. DOI: 10.1115/92-GT-336.

[61] Simon, J. F. "Contribution to Throughflow Modelling for Axial Flow Turbomachines". PhD thesis. University of Liège, 2007.

[62] Simon, J. F. and Léonard, O. "A Throughflow Analysis tool based on the Navier–Stokes equations". In: *P. ETC6*. 2005, pp. 7–11.

[63] Simon, J. F. and Léonard, O. "Modeling of 3D losses and deviations in a Through-Flow Analysis tool". In: *Journal of Thermal Science* 16.3 (2007), pp. 208–214.

[64] Simon, J.-F., Thomas, J. P., and Léonard, O. "On the Role of the Deterministic and Circumferential Stresses in Throughflow Calculations". In: *Journal of Turbomachinery* 131.3 (Apr. 2009). 031019. ISSN: 0889-504X. DOI: 10.1115/1.2992514.

[65] Smith, L. H. "The radial-equilibrium equation of turbomachinery". In: *Journal of Engineering for Power* 88.1 (1966), pp. 1–12.

[66] Stodola, A. *Dampf-und Gasturbinen. Mit einem Anhang über die Aussichten der Wärmekraftmaschinen: Nachtrag zur 5*. Springer-Verlag, 2013.

[67] Sturmayr, A. and Hirsch, C. "Throughflow model for design and analysis integrated in a three-dimensional Navier-Stokes solver". In: *Proceedings of the Institution of Mechanical Engineers, Part A: Journal of Power and Energy* 213.4 (1999), pp. 263–273. DOI: 10.1243/0957650991537608.

[68] Swanson, R. C. and Turkel, E. "Artificial dissipation and central difference schemes for the Euler and Navier-Stokes equations". In: *National Aeronautics and Space Administration Report* 1 (1987).

[69] Torre, A. and Cecchi, S. *Latest Development and Perspectives in the Optimized Design of Low Pressure Steam Turbine at Ansaldo Energia.* Invited lecture ETC7, Athens, Greece. 2007.

[70] Traupel, W. *Thermische turbomaschinen.* Vol. 1. Springer-Verlag Berlin, 1966.

[71] Wiedermann, A. and Petrovic, M. V. "Through-Flow Modeling of Single- and Two-Shaft Gas Turbines at Wide Operating Range". In: Turbo Expo: Power for Land, Sea, and Air Volume 2C: Turbomachinery (June 2018). V02CT42A006. DOI: 10.1115/GT2018-75394.

[72] Wu, C. H. *A General Theory of Three-Dimensional Flow in Subsonic and Supersonic Turbomachines of Axial-, Radial, and Mixed-Flow Types.* Tech. rep. NACA, Report No. TN-2604, 1952.

[73] Yao, Z. and Hirsch, C. "Throughflow model using 3D Euler or Navier-Stokes solver". In: *VDI Berichte* 1185 (1995), pp. 51–61.

[74] Yaras, I. and Sjolander, S. "Prediction of Tip-Leakage Losses in Axial Turbines". In: *ASME Journal of Turbomachinery* 114.1 (1992), pp. 204–210.

[75] Young, J. B. and Wilcock, R. C. "Modeling the Air-Cooled Gas Turbine: Part 1—General Thermodynamics ". In: *Journal of Turbomachinery* 124.2 (Apr. 2002), pp. 207–213. ISSN: 0889-504X. DOI: 10.1115/1.1415037.

[76] Young, J. B. and Wilcock, R. C. "Modeling the Air-Cooled Gas Turbine: Part 2—Coolant Flows and Losses ". In: *Journal of Turbomachinery* 124.2 (Apr. 2002), pp. 214–221. ISSN: 0889-504X. DOI: 10.1115/1.1415038.